Design and Operation Mechanisms of Battery and Hydrogen Based Transport Systems Integrated with Power Grids

Nader Ashraf Abd El-Fattah El-Taweel

A DISSERTATION SUBMITTED TO
THE FACULTY OF GRADUATE STUDIES
IN PARTIAL FULFILLMENT OF THE REQUIREMENTS
FOR THE DEGREE OF
DOCTOR OF PHILOSOPHY

GRADUATE PROGRAM IN ELECTRICAL
ENGINEERING AND COMPUTER SCIENCE
YORK UNIVERSITY
TORONTO, ONTARIO
June 2020

Abstract

As a result of the low Greenhouse Gases (GHG) emissions in the electricity generation profiles, electrification of transit networks represents a promising approach to reduce transportation-related GHG emissions. Two fundamental concepts have been adopted to electrify transport systems: utilization of (i) battery storage for Battery Electric Vehicles (BEV), and (ii) hydrogen for Fuel-Cell Electric Vehicles (FCEV). Each of the two concepts has its own design and operation challenges in order to be widely and efficiently deployed. Accordingly, this thesis focuses on developing new models to address the imminent challenges of design and operation practices that are associated with the adoption of both concepts.

First, novel analytical methodologies are developed to be applied to the size estimation of BEV and FCEV fueling stations, as a critical step to set the stage for the transportation electrification. The ratings of various components are expressed in terms of the system operation percentage using the proposed formulation, and the desired ratings are selected at which the net profit reaches the maximum point.

Second, both Public Bus Transit (PBT) and power utility operators retain various challenges in facilitating the seamless integration of Battery Electric Bus (BEB) fleet systems. The most salient challenges are: (i) the lack/unavailability of real-world and high-resolution speed data of BEB to accurately calculate the Electric Bus Energy Consumption (EBEC), and (ii) the lack of appropriate simulation tools to model and optimize BEB fleet systems. Therefore, a novel model to generate a set of synthetic speed profiles is proposed using the

basic information of the bus trip: duration, distance, and bus stops. A new mathematical formulation is also proposed to model and optimize the design of BEB fleet systems. The model considers the operational requirements of PBT systems, utility grid model and the EBEC characteristics.

Third, the proliferation of hydrogen fueling stations throughout the transportation network and justifying their economic viability are key factors to the success of the FCEVs. Accordingly, a new model for optimal scheduling of distributed hydrogen storage stations is proposed to serve the transport sector and the electricity market Demand Response (DR) program, besides optimizing the hydrogen sale price. Further, the Liquid Organic Hydrogen Carrier (LOHC) technology now offers a promising solution for the reliable and safe storage of hydrogen. Hence, this thesis also demonstrates how such plants should be optimally sized and operated for joint applications for concurrent services to both the transportation sector and utility grid ancillary services.

The findings of this thesis highlight the feasibility of current BEBs technology to replace diesel-based transit buses, shall appropriate technical design and measures be considered to alleviate the negative interactions between power utilities and transit networks. In addition, ancillary services provision to the grid is concluded to be a win-win situation to the utility grid and the hydrogen facility that can reduce the hydrogen sale price.

Acknowledgements

Along my PhD studies journey, there are many people who have helped and empowered me to complete my research.

First, I would like to express my genuine gratitude to my supervisor Prof. Hany Farag for his continuous and unconditional guidance and support. I have been extremely fortunate to have a supervisor who always share his success, and care about enlightening the one's knowledge, skills, and grand vision. I had a lot to learn from him both on the professional and personal levels.

I would like also to sincerely thank my committee members Prof. John Lam and Prof. Afshin Rezaei for their continuous support and valuable time and advice.

I would like to also acknowledge the enthusiastic encouragement and valuable advice provided by Prof. Moataz Mohamed. His dedication toward zero–emission transit systems inspires me to pursue my PhD studies in electrified transport systems.

I would like to recognize Dr. Hadi Khani for his valuable suggestions and constructive critiques to this research work. I truly appreciate the time we spent discussing several aspects of research, and your willingness to share with me your research experience, especially in power systems optimization. Also, assistance and advice provided by Dr. Aboelsood Zidan is greatly appreciated.

I am grateful for all my colleagues in Smart Grid Research Lab. Mohamed Zaki, Shivam Saxena, Abdullah Sawas, and Abdullah Al-obaidi, thank you guys so much for your encouragement and fruitful discussions, all of you have been always sincere and trustworthy.

Although no words can express my appreciation to you, I would like to pay a special and profound gratitude to my mother and my brother. Your love, encouragement, and prayers enable me to accomplish this research.

My heartiest thanks to my graduate studies companion, Ahmed Alsayed for always being there whenever is needed; Mohamed Abdelhamid Zizo for all our scientific and philosophical discussions and for always being there for a coffee break; Khaled Youssef for being a great support; Moomen Soliman adding cheer and joy to the group; and Ahmed

Fergala for your continuous wise advises. All of you guys have been true friends who always make me feels like home.

Lastly, I gratefully acknowledge all funding received throughout my PhD thesis studies in their awarding order: Ontario Government for offering me the Ontario Graduate Scholarship, Natural Sciences and Engineering Research Council (NSERC) of Canada for being awarded the NSERC postgraduate scholarship-Doctoral Program, Metrolinx agency for awarding me the 2018 Rob MacIsaac Fellowship, and Mitacs for offering me the Mitacs Accelerate Research Internship.

Dedication

إلي أمي الحبيبة

إلي أخي وليد

إلي روح أبي

To my Beloved Mother

To my Brother Waleed

To my Late Father

Table of Contents

List of Tables

List of Figures

Abbreviations

ADVISOR Advanced Vehicle Simulator

BEB Battery Electric Bus

BEV Battery Electric Vehicles

BONMIN Basic Open-source Nonlinear Mixed INteger

CAPEX Capital Expenditure

CBDR Capacity–Based Demand Response

CDF Cumulative Density Function

CI Confidence Interval

CIP Confidence Interval Percentage

DG Distributed Generation

DR Demand Response

EB Electric Bus

EBEC Electric Bus Energy Consumption

EV Electric Vehicles

EVFS Electric Vehicle Fuel Station

FCEV Fuel-Cell Electric Vehicles

FFS Free Flow Speed

GHG Greenhouse Gases

HVAC Heat, Ventilation and Air Conditioning

ICE Internal Combustion Engine

IRR Internal Rate of Return

LOHC Liquid Organic Hydrogen Carrier

LoS Level of Service

MAPE Mean Absolute Percentage Error

MINLP Mixed Integer Non-Linear Programming

NPV Net Present Value

OPEX Operation Expenditure

OPTI OPTimization Interface

PBT Public Bus Transit

PDF Probability Density Function

PDS Power Distribution System

PtH Power–to–Hydrogen

PV Photo–Voltaic

SAPE Standard Deviation of Absolute Percentage Error

SMR Steam Methane Reformer

SOC State of Charge

VAR Reactive Power

List of Thesis Publication

1. **Nader El-Taweel**, Aboelsood Zidan, and Hany Farag, "Novel Electric Bus Energy Consumption Model based on Probabilistic Synthetic Speed Profile Integrated with HVAC", *IEEE Transactions on Intelligent Transportation Systems*, In Press 2020. [Available Online]: https://ieeexplore.ieee.org/document/8998578

2. **Nader El-Taweel**, Hany Farag, and Moataz Mohamed, "Integrated Utility–Transit Model for Optimal Configuration of Battery Electric Bus Systems", *IEEE Systems Journal*, Vol. 14, no. 1, Mar. 2020. [Available Online]: https://ieeexplore.ieee.org/document/8894472

3. **Nader El-Taweel**, Hadi Khani, and Hany Farag, "Optimal Sizing and Scheduling of LOHC–Based Generation and Storage Plants for Concurrent Services to Transportation Sector and Ancillary Services Market," *IEEE Transactions on Sustainable Energy*, vol. 11, no. 3, pp. 1381 - 1393, Jul. 2020. [Available Online]: https://ieeexplore.ieee.org/document/8753621

4. **Nader El-Taweel**, Hadi Khani, and Hany Farag, "Analytical Size Estimation methodologies for Electrified Transportation Fueling Infrastructures Using Public-Domain Market Data", *IEEE Transactions on Transportation Electrification*, vol. 5, no. 3, pp. 840 - 851, Sep. 2019. [Available Online]: https://ieeexplore.ieee.org/document/8758467

5. **Nader El-Taweel**, Hadi Khani, and Hany Farag, "Hydrogen Storage Optimal Scheduling for Fuel Supply and Capacity-Based Demand Response Program under Dynamic Hydrogen Pricing," *IEEE Transactions on smart Grid*, vol. 10, no. 4, pp. 4531 - 4542, Jul. 2019. [Available Online]: https://ieeexplore.ieee.org/document/8425772
   * Featured in **Brainstorm Newsletter**, a special edition of York University's newsletter that showcases research and innovation at York University. [Available Online]: https://bit.ly/2mVd5jm

6. **Nader El-Taweel**, Hany Farag, Heather-Ann Niefer, "Planning and Operation of Electrified GO Bus Transit System," submitted to Metrolinx, Apr. 2018. [Available Online]: https://bit.ly/2lwgXXP

7. **Nader El-Taweel**, and Hany Farag, "Incorporation of Battery Electric Buses in the Operation of Intercity Bus Services," *In 2019 IEEE Transportation Electrification Conference and Expo (ITEC)*, June 2019. [Available Online]: https://ieeexplore.ieee.org/document/8790598

8. **Nader El-Taweel**, M. Mohamed, and Hany Farag, "Optimal Design of Charging Stations for Electrified Transit Networks," In 2017 IEEE Transportation Electrification Conference and Expo (ITEC), pp. 786 - 791, 2017. [Available Online]: https://ieeexplore.ieee.org/document/8598367

Chapter 1

Introduction

1.1 Background

The development of low–carbon technologies to mitigate GHG emissions has been considered a promising solution to address the global climate change concerns. Power utility sectors have been moving toward accommodating high penetration levels of renewable generation resources [1]. As a result of the low GHG emissions in the electricity generation profile, transportation sectors have been moving towards electric powertrain technologies for personal mobility and public transit [2, 3, 4]. This is to reduce the transportation sector major share in global emissions (i.e. 24% of the global CO2 production) [5]. Transportation electrification is envisioned as one of the most prominent solution to deal with the environmental pollution resulted from the increasing number of fossil–fueled vehicles [5].

Two fundamental concepts have been adopted to realize the transportation electrification: utilization of (i) battery storage for BEV and (ii) fuel cell for hydrogen–powered vehicles. BEVs use an on–board battery energy storage system to drive an electric motor. FCEV, on the other hand, rely on usage of hydrogen as the fuel to generate electricity from fuel cell units; the generated electricity is used to propel the vehicle's electric motor or is stored in an energy storage device (i.e., battery) [6].

Apart from the emission benefits, additional advantage of the electric powertrain is that their electric drive motors have higher energy conversion efficiencies than the Internal Combustion Engine (ICE). The energy conversion efficiency for the electric drive motors is about 76% (i.e., from on-board battery to drive the wheels), which is about five times higher compared to the average of the ICEs efficiency of 16% (i.e., from on-board fuel storage to drive the wheels) [7]. The differences between BEVs and FCEVs involve the grid to on-board storage efficiencies. BEVs have about 66% for DC fast chargers integrated with battery storage system and 78% for slow charging mode using AC chargers integrated with battery energy storage [8]. Therefore, the overall grid to wheels efficiency of BEVs is about 50% and 60% for fast and slow charging, respectively. While, FCEVs have about 57% energy conversion from grid to on-board storage [8]. Hence, by considering a 70% energy conversion for the on-board fuel cell that converts hydrogen to electricity to be stored in a buffer battery storage [9], the overall grid to wheels efficiency is about 30%. Although, the FCEVs grid to wheels efficiency is about half of BEVs, FCEVs are known for their higher mileage range, faster refueling rate, and the absence of energy storage degradation issues [6]. For this reason, FCEV is considered a competitive option for transit electrification, especially when it comes to higher mileage range and fast refueling requirements.

The electrification mix between BEVs and FCEVs has the potential to efficiently electrify the transportation sector. However, each of the aforementioned transportation electrification concepts has its own challenges to be efficiently deployed.

Firstly, with respect to the BEVs adoption, several studies in the literature focuses on mitigating the challenges to deploy personal BEVs. A stream of research investigates the integration of energy storage system with the BEVs parking lot. This is to (i) reduce the demand charge per annum, (ii) relieve the pressure on the grid, and (iii) minimize the Operation Expenditure (OPEX) thereby maximizing the net profit [10, 11]. In addition, the studies for optimal sizing and allocation of the BEVs charging stations are diverse in the literature [12, 13, 14, 15, 16, 17, 18, 19, 20, 21, 22, 23]. The main objectives of the optimal

sizing and allocation of the BEVs charging stations are (i) estimating the vehicles power demand and charging schedule to satisfy the BEVs State of Charge (SOC), (ii) minimizing the Capital Expenditure (CAPEX) of the charging station components (i.e., number of chargers, waiting spaces in the charging stations, storage system, backup distributed generation units etc.) and the purchased electricity from the utility, (iii) satisfying the distribution system constraints, and (iv) investigating the opportunity of the BEVs charging stations to provide ancillary services to the power grid to enhance their profitability.

Alongside the research efforts devoted to promote for the personal BEVs, electrification of PBT has been considered as one of the most salient approaches to reduce transit–related GHG emissions [24]. Public bus fleets operate on fixed routes to carry passengers from one place to another according to a predetermined daily operating time schedule and fixed routes, which makes them a potential target for full electrification [25], [26]. Further, electrified PBT have the potential to maximize the utilization benefits from renewable power generation [27]. In this regard, BEB technologies that utilize on–board batteries and chargers are considered eminent solutions to move toward zero-emission PBT systems [28]. This is due to the BEB high technology maturity level compared to other electrification technologies such as fuel cell electric bus [28]. However, due to their emergent nature, BEB technologies have created new transportation-energy matrix, which is incomprehensible to transit and utility sectors. The transportation sector faces challenges in terms of implementing a full electrification system, due to the conflict between transportation operational requirements and electric network obligations. Previous analysis of the interactions between the operation of BEBs [27, 28, 29, 30], sheds light on several challenges, such as, but not limited to: (i) impact of charger capacity upon the operational demand profile and the charging queuing time of buses; (ii) additional BEB requirements to maintain the operational schedule; and (iii) transit impact of BEBs on the utility grid e.g., voltage, feeder's capacity, and power balance. It could be argued, therefore, that due to the variation in PBT operation and utility grid profile, a trade-off is required in order to optimize transit

operation, utility grid demand profile, and BEB configuration: these being battery size, charger power, and number of required chargers.

Secondly, compared to BEVs, FCEVs are known for their higher mileage range, faster refueling rate similar to diesel-based vehicles, and the absence of energy storage degradation issues [31]. However, hydrogen gas, the FCEV feedstock, needs to be produced and made available to the transportation sector [32]. Hydrogen can be cleanly produced using an electrolyzer, known as the Power–to–Hydrogen (PtH) technology, whereby electricity is utilized to diffuse water into hydrogen and oxygen [32]. The generated hydrogen from PtH can be stored in the form of liquid or gas in a reservoir for later use. Hydrogen can then be converted back into electricity and supplied to the power grid using a fuel cell, or it can be directly sold to the transportation sector (i.e., to supply FCEVs) [33]. It should be noted that hydrogen can be generated either centrally in large scale and then be transported to hydrogen fueling stations, or produced on site (i.e., at hydrogen fueling stations). Despite the fact that mass production at central hydrogen generation plants is more economical, the transportation cost of the hydrogen to the consumption areas could escalate the overall cost. For this reason, it has been argued that the production of hydrogen should take place within the fueling station facility in order to alleviate the transportation cost and increase the reliability of hydrogen availability [34], [35]. Although the implementation of hydrogen fueling stations has attracted the attention of industry sectors [36], such stations have not been completely materialized yet. This is mainly due to the following reasons: (i) the development of the FCEVs is currently at the demonstration/commissioning stage [37]; (ii) there is a gap between the present rate of return and the expected profit from the investment in such stations, and (iii) the absence of the techno–economics models, which investigates the optimal planning and operation of the distributed/centralized PtH generation plants across the power system network [35]. Hence, deployment of hydrogen fueling stations over the transportation network is required for the success of the FCEVs. However, the economic viability of such stations needs to be justified in order for them to

be proliferated. In addition, the integration of such stations into the power systems should be carefully investigated, in order to avoid any negative impacts on the power system.

1.2 Thesis Objective

This thesis aims to facilitate the seamless adoption of electrified transportation systems and their integration into the power grid by counteracting the timely research gaps that challenge the realization of electrified personal and PBT networks. Battery–based personal and PBT proliferation obstacles lay upon their limited driving range, negative charging impact on the power grid, and their economic viability. Hence, novel planning and operation models are required to maintain the power grid prerequisites constraints, while optimizing their infrastructure economic metrics. In contrast, the challenge to realize hydrogen–based transit networks are prescribed to be the lack of hydrogen availability i.e, production facility and infrastructure. Thereby, techno–economic planning and operational models for the hydrogen production and storage facilities integrated with power grids are required to advance the existence of hydrogen-based transit networks. Based on the above discussion, this thesis aims to achieve the following identified objectives:

1. Development of an analytical sizing approach for the sizing of both battery–based and hydrogen–based Electric Vehicles (EV)s fueling stations.

2. Development of a probabilistic model to generate synthetic electric buses speed profiles using the basic information of the bus trip (i.e., trip time, distance, and stop locations) traffic conditions, weather conditions, and the operation of Heat, Ventilation and Air Conditioning (HVAC) systems. Using such model, PBT planners can accurately assess the energy consumption characteristics of electric buses at different operating conditions to plan for the electrification of the PBT system, when there is a lack or unavailability of real–world and high resolution data.

3. Development of an integrated model for power utility grid and PBT network, which aims at optimizing the BEB system configuration for a PBT fleet: these being battery capacity; chargers' rated size; and number of chargers.

4. Development of an optimal scheduling algorithm for the integration of distributed hydrogen fueling stations into the distribution power network.

5. Development of an optimal planning and scheduling model for the integration of a centralized hydrogen production and storage facility into the transmission network.

1.3 Thesis Layout

Following this introduction, the remainder of this thesis is outlined as follows:

- **Chapter 2**: Provides critical literature survey on the integration of electrified transit networks into power systems.

- **Chapter 3**: Presents novel analytical sizing models for the sizing of both battery–based and hydrogen–based Electric Vehicle Fuel Station (EVFS).

- **Chapter 4**: Presents a novel and generic probabilistic model to calculate the EBEC without the need for a high–resolution speed profile data. Roadway Level of Service (LoS) is incorporated in the proposed model to simulate different traffic conditions. Further, the operation of the HVAC is also incorporated in the model using the thermal mass balance principle.

- **Chapter 5**: Presents a new mathematical formulation to model BEB fleet systems. The model considers the operational requirements of PBT systems and the energy consumption characteristics of BEBs. The proposed transit model is then integrated with the power distribution system model to develop an integrated utility-transit

problem formulation for the optimal design of BEB systems. The formulated optimization problem aims at determining the optimal configuration parameters of BEB fleet systems that include: the bus battery capacity, chargers rated power, and the total number of installed chargers in the charging station.

- **Chapter 6**: Presents a novel model for optimal scheduling of privately owned hydrogen storage stations to both serve the transport sector and the electricity market operator. The model mainly aims to (i) exploit the lower electricity market prices to reduce the power purchase cost and (ii) contribute to the capacity-based demand response program to further enhance the economic feasibility of the investment.

- **Chapter 7**: Demonstrates how LOHC–based hydrogen generation and storage plants should be sized and operated for joint applications, in order to enhance the system rate of return. In particular, a new model is proposed for optimal sizing and scheduling of the LOHC–based generation and storage plants for concurrent services to both the transportation sector and ancillary services market.

- **Chapter 8**: Presents the conclusion of this dissertation, identify the contributions and draw directions for possible future work.

Chapter 2

Literature Survey

2.1 Introduction

The population growth in many countries will bring about an increase in public and freight transportation levels of demand in the near future [30, 38]. As such, it is expected that transportation sector GHG emissions will rise to higher emission rates [30, 39]. This will in turn necessitate the need of deploying innovative approaches that are capable of effectively serving the growing transportation demand while addressing their environmental concerns [30, 38, 39, 40, 41]. The proliferation of electrified transportation systems is envisioned as a promising solution that could significantly contribute to the reduction of environmental pollution [42]. In this regard, this chapter presents a brief background and literature survey on the challenges that face the seamless adoption of electrified transport networks.

2.2 Adoption of personal BEVs

Several studies in the literature investigate the economic viability of integrating energy storage systems with the personal BEV charging station. In [10], a study is carried out to assess the economic viability of coupling energy storage with a fast charger unit. The study

indicates that storage is effective in reducing the demand charge per annum, in addition to relieving the pressure on the grid. The authors in [11] develop a model that would manage the operation of a fast charging station coupled with Photo–Voltaic (PV) units in order to minimize the OPEX, thereby maximizing the net profit.

The studies for optimal sizing of the battery–EVFS or hybrid vehicle components are diverse in the literature. In [12], the authors propose a methodology to optimally size storage systems used for a BEV charging station by utilizing a probabilistic approach to estimate the vehicles demand. The study aims to minimize the CAPEX of the storage and the purchased electricity from the utility. In [13], the authors propose a searched–based optimization approach that would solve a nonlinear integer problem in order to optimally size a fully–green charging system consisting of storage and a set of PV panels. The model aims at minimizing the charging station CAPEX, while satisfying the BEVs demand. The study in [23] is focused on a mixed integer linear programming model for determining the optimal sizing and operational strategy of battery storage integrated with fast BEVs charging stations. The study in [43], presents a sizing solution for fast BEVs charging stations is presented based on an explicit temporal SOC characterization of the BEVs charging demand. The optimal number of chargers and waiting spaces in the charging stations are determined by the model taking into consideration the cost–benefit performance of the system. The authors in [44] develop a method to design the number of charging points and size an energy storage system for fast BEVs charging stations. This is to alleviate the need to upgrade the electricity grid infrastructures at the charging station location. The work in [44] considers the acceptable waiting period of BEVs in order to come up with designing the number of charging points.

In addition, several studies present optimal sizing and allocation of the battery-EVFS or hybrid vehicle components in the literature. A bi–layer Pareto optimization approach is proposed in [14], in order to size and allocate a BEV–based parking lot. The model seeks to maximize the parking lot profit, while satisfying the distribution system constraints.

In [15], the authors propose an embedded Monte Carlo simulation–based method with the genetic algorithm to optimally size and allocate a plug–in hybrid EV charging station connected to a distribution system. The work in [15] considers profit gained by the charging station through participation of the BEVs charging stations to the demand response program. In [16], the authors evaluate the impact of demand response program on the profitability of BEVs charging stations considering the effect of the stations on distribution system power losses. The model utilizes a particle swarm optimization algorithm to size and allocate the BEVs charging station that would minimize the stations initial cost and systems losses. A two–stage optimization model is given in [17] that would allocate and size stand–alone BEVs charging stations on highways. The optimization model handles the uncertainties of the traffic and solar irradiance using a probabilistic distribution model. In [19], the authors present an optimization process for sizing and allocation of BEVs charging stations aiming to minimize the integrated cost of charging stations and consumers. Case studies are conducted to demonstrate how the method can reduce the initial and operation costs of BEVs charging stations. The authors in [20] present a model for sizing and allocation of various renewable–based Distributed Generation (DG) units, BEVs charging stations, and storage devices within a power distribution system. They have formulated their model as a second–order conic programming problem taking into consideration the time-varying nature of DG generation and demand consumption. The study in [21] is mainly focused on optimal sizing and allocation of BEVs fast–charging stations contemplating the interactions between the transportation and power networks. The model also considers the security operation constraints of the distribution network to ensure that the limitations of the grid are met by the model. The authors in [22] present a technique for optimal sizing and allocation of fast BEVs charging stations considering the transportation and power grid losses.

In addition to the above–cited studies on the optimal sizing and allocation of renewable–based battery–EVFS, some studies have focused on the planning of such stations, e.g., in

[45, 46, 47], while some have proposed methods for optimal locating of these stations, e.g., in [48].

While several optimization–based sizing models are presented in the literature, analytical models for sizing of the electrified transportation infrastructure that do not require sophisticated optimization toolboxes are missing from prior studies. An analytical sizing model involves mathematical equations as functions of the optimal sizing and system's reliability constraints [49]. The main challenge to solve such analytical models would be to estimate coefficients and unknown parameters of the analytical equations [50]. For instance, the work in [49] proposes an analytical model to optimize the size of a standalone PV system that satisfies the loads reliability, while minimizing the system's cost. A multi–objective analytical sizing model is proposed in [50] to size a PV system that would supply a water pumping unit. The model in [50] aims to minimize the system's life cycle cost and the deficiencies related to the power supply. In [51], an analytical model is utilized to design the sizing of a hybrid wind, PV, fuel cell, and a hydrogen energy storage system. An analytical sizing approach for customer–side battery storage system is proposed in [52], in order to reduce the customer's electricity bills while considering the system's benefits and costs.

2.3 Battery-Based Electric Buses

In tandem with the research efforts to promote for the adoption of personal EVs, the electrification of PBT networks has been considered as one of the most salient approaches to reduce transit–related GHG emissions [24]. Bus fleets operate on fixed routes and schedules, which facilitate the planning and operation of electric buses [27, 28]. In order to compensate for the limited BEB driving range, three operation concepts have been proposed: battery swapping, wireless charging, and on–board battery charging [27, 53].

Battery swapping technique involves the use of a mechanical arm to replace the drained battery packs of the BEB in few minutes [26]. Yet, the battery swapping concept has several drawbacks with regard to the need of huge investment in infrastructure, standardization of battery packs for interoperability and changeability, as well as battery degradation and ownership [26, 27].

The wireless charging concept implies transferring energy from a power transmitter that consists of an inverter and inductive track [53]. Where, the BEB charges on–road during its motion over the inductive track. Nonetheless, wireless charging for BEBs requires extra investment in the road infrastructure and design [25]. This is due to the need for sizing and allocating the wireless charger structure according to the BEBs' battery capacity and charging requirements [25].

Based on the aforementioned reasons, the concept of on–board battery charging systems is currently under wide investigation and development as a critical mean for the large–scale adoption of electrified PBT fleets. In this regard, two types of BEB charging–based systems have been proposed: overnight and opportunity. The main difference between the two types is the trade–off in the BEB battery capacity i.e., driving range, and the required rated power of chargers i.e., charging time [27, 28]. BEB systems that rely solely on overnight–charging require chargers that have relatively smaller power ratings. In which, overnight BEB chargers are installed at the bus depot/garage to provide a long time charging for a large battery capacity, compared to opportunity–based BEB. Previous studies, however, showed that overnight–charging BEB systems might require an increase in the BEB fleet size, relative to the current diesel–based fleet, to maintain the predefined operation scheduling of transit networks [28]. Opportunity–charging BEB systems, in contrast, utilize on–route high–powered chargers to provide frequent and short time charging for BEBs equipped with relatively smaller battery capacity. On–route charging systems utilize automated overhead pantographic arms to charge the BEBs in the transit hub(s) (i.e., bus terminal(s)) or along the transit routes [54, 55]. Several world–wide demonstration projects showed that

on–route charging technologies are capable of sufficiently charging BEBs within 4–6 minutes [54, 55].

2.3.1 Battery Electric Bus Modeling

Recently, modelling EBEC is being the subject of many publications. BEBs consume energy to provide motive power and to support its HVAC system, besides their auxiliary systems [56]. A real-world EBEC depends on many factors such as bus type, speed profile (speed of a vehicle versus time), passenger loading and alighting, driver, HVAC operation and auxiliary power demands [56, 57]. Furthermore, EBEC can be affected by some external factors such as traffic congestion and time of traffic [57, 58]. With accurate EBEC analysis and estimation under real–world traffic conditions, the advantages of BEBs can be accurately quantified [58]. EBEC model describes the quantitative relationship between the energy consumption rate for BEBs and their impact factors through analytic and/or data–driven models [59]. Future driving conditions can be predicted based on historical driving data and online estimation methods for a given city route [60, 61]. As such, without complete information about future driving cycles, the genuine EBEC can not be guaranteed, thereby efficient planning for the BEBs infrastructure can not be attained [62]. From another side, measuring high time-resolution speed profile data is difficult, if not impractical for large bus fleets [62, 63].

A number of state–of–the–art approaches used a single average or median value to determine the energy requirements of BEBs. Authors reported energy consumption rate (kWh/km) in wide ranges. The reported kWh/km consumption rates are 1.24–2.48 for BEBs [64], 1.7– 4.1 for length of 12 m BEB [65], 1.2–2.9 for length of 10 m BEB [65], 1.1–2.2 with an average of 1.6 for single-decker buses [63], 1.6–3.2 with averages of 2.3 and 2.5 for double-decker and articulated buses respectively [63], 2.4–4.5 for double–decker BEBs in intercity bus services [66], 0.8–1.2 for BEBs [56], 1.5 for BEBs [67], 1.8–3 for series plug-

in hybrid buses with high-power energy Li-ion battery [68], 3.2–5 for series hybrid buses with high-power energy Li-ion battery [68], 3–5.8 for parallel hybrid buses with high-power energy Li-ion battery [68], and 3.5–7.8 for parallel hybrid buses with supercapacitor [68].

Estimating EBEC based on a single average value is inaccurate because it doesn't reflect the high variability of real–world situations [63, 67]. In addition, ignoring uncertainty of EBEC and travel time may cause unnecessarily over-sizing of the BEBs' system design; and thus, leads to a sub–optimal or infeasible plan for BEB systems [63]. For these reasons, it is paramount to develop a stochastic model for investigating how the uncertainty in speed profiles data would affect the EBEC model and in consequence the optimal BEBs' system design.

Several studies in the literature investigate the factors that impact the EBEC. Ref. [69] used grey relational analysis method to analyze various external factors that affect EBEC such as travel date (i.e., working day or weekend), weather conditions (temperature, haze or rain), length of travel path, vehicle HVAC, and vehicle running limit. These influencing factors are converted into numerical values through fuzzy rules. Then, wavelet neural network was used to train EBEC factors together with EBEC data to establish the EBEC prediction model. The proposed EBEC model requires actual survey data which reflects the multiple external influencing factors to be used for training the wavelet neural network and to establish a similar day selection model. However, most transit companies do not have these real operational data about BEBs. Authors in [25] proposed BEB system with wireless power transfer technology, however, randomness in speed and uncertainty in energy demand are not included. They assumed that: (i) BEBs follow predefined velocity profiles; (ii) the energy demand between stations is known; (iii) BEB stops at every station; and (iv) 3 kW of extra electrical load per hour is uniformly needed in the energy demand evaluation for the air conditioner and radio. Refs. [61, 64, 66] used the vehicle longitudinal dynamics equation to model BEB with real-world driving data for routes under study. These standardized historical bus drive cycles do not reflect uncertainties of real-time

traffic. For instance, they do not account for different traffic conditions and the HVAC operation and consumption. Ref. [65] proposed an operating mode binning method to assess on-road EBEC and well-to-wheel air pollutants emissions of BEBs based on second–by–second real-world data. BEBs were tested during rush and non-rush hours and under three fixed usage conditions: 1) empty load with 5-10% of bus capacity and AC off, 2) half load with 40-45% of bus capacity and AC off, and 3) half load and AC on. Also, all usage conditions were subjected to stop for approximately 1 minute at each bus station. Based on real–world trolleybus measurements, the author in [57] quantitatively assessed the parameters that impact EBEC to be used as a basis for training drivers and an element of eco–driving assistance systems. Trolleybus is bound to a certain track based on presence of an overhead electric wire. This difference compared to autonomous BEBs has impact on its supply system and electrical equipment. Also, influence of traffic conditions and congestion may be different.

Multiple decision analysis methods, correlation analysis, and linear regression were applied to select the EBEC parameters. Ref. [63] presented a longitudinal dynamics model to calculate EBEC using low-resolution data that can be collected from day-to-day operations. They assumed that: 1) the required auxiliary power for air conditioning and various auxiliary services is constant over the driving duration and the dwell time; 2) there is at least one intermediate halt per trip and one more for each 5 km/h-step that the average speed of the trip takes under 25 km/h; and 3) the acceleration is constant during each part in the speed profile (acceleration, coasting, and deceleration). Ref. [56] proposed a simplified model to simulate EBEC in different operating conditions using measured data from existing bus lines. The required auxiliary power was assumed to be 6 kW in mild weather conditions, 14 kW in cold or hot conditions, and 22 kW in extreme cold conditions. The passengers load was assumed to be 50 passengers (3750 kg) in all simulations. In Ref. [59], EBEC under real-world traffic congestion was decomposed based on both positive kinetic energy and negative kinetic energy (regenerative braking). Then, a data-driven

model was built to estimate EBEC on each route. In [62], a multi-objective stochastic model predictive control was proposed for EBECs. The vehicle longitudinal dynamics model was applied to simulate BEBs' demand torque. Furthermore, the Markov-chain based stochastic driver model was built to describe the demand torque in different speed ranges. Tested driving cycles were too short, and cycles repeated several times. Thus, those driving conditions are simpler than real-world driving cycles. Moreover, optimal results depend on the weight value for multi-objective problem.

Ref. [70] evaluated EBEC using vehicle longitudinal dynamics model. Authors calculated EBEC based on the average bus speed and distance between stops. A 60% and 100% of full bi–articulated high capacity bus occupancy (250 passengers) were considered during regular and rush hours, respectively. Furthermore, the probability of stops at traffic lights represented with a binomial distribution function. Bus stops are distributed each 500 to 600 m. The average slopes between stops are considered through a route elevation profile computed from altitude data using intermediate points. In [71], the vehicle longitudinal dynamics model was applied to calculate the required torque at the wheel for BEBs. A hierarchical clustering algorithm was applied for driving cycles' data clustering. Then, support vector machine method was applied to predict current driving cycle. The upper and lower thresholds for the road slope are assumed to be 3% and -3% respectively. Linear mapping was applied as results contain more than 90% information of the variance in the data. In [72], the vehicle longitudinal dynamics model was applied to calculate the required power for EBECs. The required auxiliary power for air conditioning systems, pumps, lights, and instruments assumed to be constant power of 6 kW. Authors in [73] proposed a predictive air-conditioner control for EBECs with passenger amount variation forecast. They assumed that each BEB always stops at each station for 30 second and drives between two adjacent stations for 120 second; and thus, the stopping time and driving time's impact was ignored. The driving profile is assumed to follow a fixed driving pattern between all bus stops. However, real–life driving conditions are more complicated. Ref. [74] proposed

a segment-based method for generating large numbers of varying synthetic driving cycles and passenger numbers for a specific bus route. The uncertainties due to weather condition variations and heater power were not included in the simulation model. Moreover, traffic-related stops were not included to avoid excessively short segments, and the simulation model is validated only for a specific ambient temperature.

In [67] a model to optimize charging infrastructure for BEBs in urban context is presented. The presented model did not include road elevation and it was assumed that any increases of energy consumption due to uphill direction will be compensated by the downhill direction of the route. Also, 1.5 kWh/km was applied as an average value for the energy consumption rate. Ref. [4] explored a charging infrastructure for electric road freight operations including auxiliary services for Electric Bus (EB)s. The average energy consumption rate was calculated at 1.7 kWh/km. Authors assumed that vehicles are 50% loaded with an overall mass of 2.8 ton. Also, a 2 kW constant load was assumed to model the drawn power from the refrigeration unit.

2.3.2 BEB Integration into the Power Distribution System

The lack of modeling tools, standardization, and real–life experience of BEB systems along with the availability of different configurations i.e., on–board battery packs and charging technologies, have created a new transportation–energy matrix, which is incomprehensible to transit and power utility stakeholders [30]. On one hand, transit agencies have a near complete lack of knowledge for the operation of BEB systems and interaction with power utilities [30]. Further, PBT operators have rigid bus schedules and operational logistics that must be maintained when BEB systems are implemented. In this regard, previous works investigated the relation between the charger's capacity and the charging queuing time of buses and its subsequent impact on the transit operation schedule. In [70], the authors highlighted the need to increase the BEBs dwelling time at the bus stops to sufficiently

charge the BEBs, thereby avoiding the need to integrate additional bus stops to charge the BEBs on-route. The authors in [75] reveal that the queuing time of charging might cause a decrease in the transit service frequency and/or increase in the trip time. However, increasing the dwelling time, adding extra bus stops and decreasing the service frequency challenge the predefined transit operational scheduling [70, 75]. In contrast, the work in [76] shows that adopting appropriate charging strategy can maintain the transit schedule requirements. On the other hand, power utilities have concerns regarding the negative impacts of adopting the electrified transit fleet systems on power grids. The charging schedules of the BEBs might impact the stability and losses of the power grid [53]. The authors in [28] showed that BEBs opportunity–charging creates serious voltage regulation challenges in power distribution systems. In order to mitigate a similar issue imposed by personal BEVs on the Power Distribution System (PDS), authors in [77] proposed a coordinated charging mechanism for BEVs according to the PDS condition. Also, in [78] an optimization approach is presented to optimally charge the BEVs, in such a way as to not violate the PDS operational constraints. However, flexible charging coordination of BEBs is not a viable solution, due to the transit rigid operational requirements that are defined by the transit schedules.

Few attempts were recently carried out in literature to provide seamless adoption of BEB systems. The authors in [79] proposed a charging schedule based on minimizing the operational charging cost. However, the BEBs system' configuration was predefined. Also, a fixed charging time window was assumed i.e., it was not optimally allocated. Moreover, the deadhead travel of the BEBs toward the charging station located at the transit depot was neglected. In [80], a scenario–based BEB transit operation scheduling was developed for routing network design and fleet planning; however the transit operational requirements i.e., defined schedule and routes, were not maintained. In [81], a new configuration design algorithm was developed to minimize the construction cost of BEB transit systems. The developed algorithm in [81] assumed that the number of chargers is equal to the number of

BEBs. Optimal wireless charging schedule for BEBs that considers the day–ahead electricity market is proposed in [53], that aims to minimize the charging operation cost. In [27], the authors proposed a mixed integer linear algorithm to design the BEBs charging stations for different transit networks for a predefined capacity of the bus battery packs. The work in [82] proposed an operational energy management model to design and coordinate the operation of an energy storage system, which aims to minimize the BEBs operation charging cost.

2.4 State of the Art in the Adoption of Fuel Cell Electric Vehicles

FCEV powertrain is introduced as a promising technology to reduce the GHG emissions associated with the conventional ICE vehicles [31]. Compared to battery–based EVs, FCEVs are known for their higher mileage range, faster refueling rate, and the absence of energy storage degradation issues [31]. However, the limited existence of hydrogen infrastructure: production; storage; and transportation; impedes the investment and deployment of FCEVs technologies [27].

Hydrogen gas, the FCEV feedstock, needs to be produced and made available to the transportation sector [32]. Hydrogen can be produced using an electrolyzer, known as the PtH technology, whereby electricity is utilized to diffuse water into hydrogen and oxygen [32]. Steam Methane Reformer (SMR) is another means that can also lead to hydrogen production by utilizing natural gas (i.e., methane). In such a technology, methane gas can be accessed from renewable biogas resources, e.g., landfills, agricultural residues, waste, etc. The generated hydrogen from PtH and/or SMR can be stored in the form of liquid or gas in a reservoir for later use. Hydrogen can then be converted back into electricity and supplied to the power grid using a fuel cell, or it can be directly sold to the transportation

sector (i.e., to supply FCEVs) [33]. It should be noted that hydrogen can be generated either centrally in large scale and then be transported to hydrogen fueling stations, or produced on site (i.e., at hydrogen fueling stations). Despite the fact that mass production at central hydrogen generation plants is more economical, the transportation cost of the hydrogen to the consumption areas could escalate the overall cost. For this reason, it has been argued that the production of hydrogen should take place within the fueling station facility in order to alleviate the transportation cost and increase the reliability of hydrogen availability [34, 35].

Electrolysis process to generate renewable hydrogen is a mature technology since the early of the 20th century [83]. Since then, world–wide large electrolyzer plants have been built close to the hydro power stations to utilize low electricity prices during off–peak periods [83]. There are three types of electrloyzer technologies known as alkaline, polymer electrolyte membrane, and solid oxide. Both the alkaline and polymer electrolyte membrane electrolyzers are currently commercially available, however solid oxide electrolyzers are still under research and development stage [83]. Alkaline electrolyzer are developed in the early of the 20th century, where in 1902 there was above 400 of operated alkaline electrolyzers around the world [83]. The alkaline electrolyzers are known of their high operation efficiency for large plants with high hydrogen production rates. According to the literature, the deployment of hydrogen fueling stations has increased over the past few years. In 2013, there were 224 hydrogen stations around the world, 37 of which had on–site electrolyzers [84]. Ever since, more hydrogen stations have been deployed around the world. Currently, there are 62 hydrogen fuel stations in the US, 30 of which have been deployed in California between 2015 and 2017 [35].

2.4.1 Distributed Hydrogen Generation

The implementation of distributed hydrogen fueling stations has attracted the attention of industry sectors [36], though such stations have not been completely materialized yet. This is mainly due to the following reasons: (i) the development of the FCEVs is currently at the demonstration/commissioning stage [37]; and (ii) there is a gap between the present rate of return and the expected profit from the investment in such stations [35].

Deployment of hydrogen fueling stations over the transportation network is required for the success of the FCEVs. However, the economic viability of such stations needs to be justified in order for them to be proliferated. The main role of hydrogen stations would be to generate hydrogen, store it, and sell it to the vehicles as fuel. Single purpose utilization of such stations, however, may not justify their intensive capital investment [35]; but rather, they should be utilized for multiple purposes at the same time so that they could generate revenue from multiple sources. This would, in turn, necessitate the development of new models in order to optimize the scheduling of distributed hydrogen stations for multiple purposes concurrently.

Several studies in the literature focus on the application of hydrogen storage units integrated with the electric grid. In [85], the authors perform an optimal sizing for a hydrogen storage system that utilizes the curtailed wind generation for hydrogen production. A fuzzy–based real–time power management mechanism for a hybrid system including fuel cell, electrolyzer, and hydrogen storage is presented in [86]. A hydrogen–based stand–alone system for rural communities is proposed in [32], where the hydrogen is used to maximize the penetration of renewable power and to perform active/reactive power management. In [87], a local energy market for hydrogen–based hybrid power systems is proposed to reduce the peak demand, and to eliminate the power mismatch between renewable generation and the demand. An operational algorithm for an integrated wind generation and hydrogen storage unit is proposed in [88], where the algorithm aims to exploit the arbitrage

opportunities through a day–ahead contracted power trading mechanism with the power grid. The authors in [89] perform an economic feasibility study for a hydrogen storage system embedded with the power grid. The outcomes of the study highlight that storing electricity in the form of hydrogen for later electricity generation is not economical, unless hydrogen is sold to the hydrogen market (i.e., supplying FCEVs), or for ancillary services to the grid such as voltage and frequency regulations. In [34], the authors develop a model to schedule the hydrogen production for hydrogen fueling stations, which aim to meet the hydrogen demand and minimize the generation cost. A techno–economic study is evaluated in [90] for central hydrogen production plant integrated with wind and PV units. An energy management system for hydrogen–based microgrids is presented in [91], where hydrogen energy is exploited to alleviate the mismatch between the power demand and generation. An optimal sizing method for hybrid microgrids and storage systems is proposed in [92] that includes a mix of renewable generation as well as battery and hydrogen storage unit. This is to investigate the optimal mix between various energy storage systems that would ensure the system reliability and resilience. It is pointed out that hydrogen storage can be economically justified when it is used to maximize the renewable energy integration. An energy management system based on fuzzy logic is proposed in [93] to optimize the operating cost for a standalone hybrid microgrid which hosts a mix of renewable sources, battery storage, and hydrogen storage. In [94], the authors present an optimization–based algorithm to size a hydrogen generation hub consisting of electrolyzers and interconnected wind turbines. Supervisory–based controllers for distributed hydrogen fueling stations using on–site electrolyzer is developed in [6]. The supervisory controller aims to optimally schedule the electrolyzers and determine the hydrogen fuel prices, while allowing the participation of the stations to the DR program.

Numerous studies are conducted in prior research works, as cited above, to facilitate the utilization of hydrogen storage for multiple applications; yet, the economic features of the hydrogen storage units for multiple applications from the private investor's perspective

is not adequately investigated in the literature.

Previous studies on the green transportation technologies mainly identify the BEVs as the most viable option to replace ICE–based vehicles. For instance, the authors in [95] propose an on–line pricing scheme to provide a fixed profit for the BEVs charging stations, based on the energy and the time window at which BEVs charge. In [96], a safeguard profit constraint is considered in a dynamic pricing algorithm for BEVs charging stations in the presence of renewable generation and battery storage. The model is operated in the wholesale electricity market and aims to achieve a certain level of guaranteed profit via the profitability constraints, where the authors present a multi–objective optimization framework for BEV charging that would determine the charging prices and the amount of energy to be purchased from the real–time market. The authors in [97] develop a real–time algorithm to maximize the profit of fast charging stations equipped with energy storage and renewable generation units, where the algorithm considers providing reserve regulation services to the grid. The algorithm aims to control the energy and reserve prices for BEVs so that BEVs can determine their charging setpoints and reserve strategies accordingly. Similarly, a multi–stage optimization–based algorithm is proposed in [98] for BEVs charging stations equipped with battery storage and renewable generation units, where the model updates the BEVs charging prices and setpoints on an hourly basis for maximizing the profit. In [99], the optimal pricing for BEVs in a competitive market is proposed, so that each station can have its own price as a function of the electricity market data. The authors in [100, 101] consider the BEVs charging facilities as flexible resources for DR programs to maximize the revenue.

2.4.2 Centralized Hydrogen Generation

Hydrogen–based transportation technologies are among the most promising solutions that could contribute significantly to the mitigation of the environmental issues by replacing

the fossil–fueled vehicles. For this reason, research on hydrogen generation, storage, and transportation has been widely devoted. Besides, the LOHC technology is now offering a reliable and safe solution for hydrogen storage and transportation. The LOHC technology allows hydrogen storage in a dense liquid medium using a catalytic hydrogenation reaction. Thus, the need for high pressure and super insulated reservoirs for hydrogen storage and transportation is eliminated [102]. This would also reduce the high transportation cost associated with the transportation of the low density hydrogen gas. The superiority of the LOHC technology is not limited to its high energy density, but also lies in its seamless integration with the current fossil fuel logistics and supply chain [103]. Given that LOHC can be transported and stored using the existing infrastructures, the initial expenditure for diffusion of the LOHC–based fueling stations can be decreased considerably [104].

Several works in the literature investigate the implication of LOHC technologies as cited and discussed below. An economic study for the supply chain of various hydrogen storage technologies is carried out in [104]. The results indicate that the LOHC technology offers an economic solution to store massive amounts of hydrogen. In [90] a techno–economic study for LOHC–based storage systems is investigated. The study found that storage systems are economically viable when the majority of the energy is provided from on–site renewable sources. The study further shows that the LOHC technology is an economically viable solution for storage when compared to alternative approaches [90]. The work in [102] highlights the ability of the LOHC–based hydrogen storage systems to dynamically respond to the variation of power demand. The study investigates how a dehydrogenation unit can effectively and reliably release the hydrogen gas that would feed a fuel cell unit, in order to dynamically supply variable loads. The authors in [105] develop an integrated LOHC storage and combined heat and power system. The study uses the integrated system to maximize the self–sufficiency of heat and electrical demand/generation and to improve the efficiency of the system.

2.5 Research Gaps in Electrified Transport Systems

Firstly, the deployment of EVFSs as the critical infrastructure is a prerequisite for the successful proliferation of FCEVs and BEVs. In such a case, it is imperative that these stations are properly sized to minimize the CAPEX and maximize the operating profit of the stations. This would, in turn, promote private investments in this sector. To that end, private investors are in need to have accessible analytical tools for the estimation of the ratings of the EVFSs and the rate of return depending on the electricity market and transportation demand in which the station is operated. Although, several optimization–based sizing models are presented in the literature, analytical sizing models for electrified trans portion fueling infrastructures are missing from prior studies. An analytical sizing model compromises a set of mathematical equations as functions of the optimal sizing and system's reliability constraints [49]. The main challenge to solve such analytical models would be the estimation of the unknown parameters and coefficients of the derived analytical equations [50].

Secondly, with respect to the EBEC estimation, most state-of-the-art methods have one or more of the following limitations: 1) require high time-resolution speed profiles which are difficult to obtain due to lack of operational data and high associated costs; 2) do not consider complexity and variations of extensive real-world operational conditions; and 3) depend on typical driving cycles and do not consider randomness in speed and uncertainty in energy demand. In order to overcome the aforementioned issues, this thesis proposes a practical alternative to calculate EBEC without the need for a high time-resolution speed profile data, while still considering the operational details of transportation networks.

Thirdly, while several ongoing demonstration and pilot projects around the world will provide the real–life data and experience, exploring the wide adoption of different BEB fleet sizes requires appropriate modeling and design tools. Previous attempts in the design of BEB systems share a common shortfall to: (i) develop a mathematical model for elec-

trified PBT fleets; (ii) incorporate accurate modeling for the energy consumption of BEBs taking into account the route topology, weather conditions, and traffic flow; (iii) consider the operational requirements of power distribution networks; and (iv) define the optimal configuration of both bus battery packs and chargers. As a result, transit agencies and power utilities face substantial technological and operational obstacles in integrating off–the–shelf BEB systems and thus research and development efforts are required to explore their challenges and mitigation techniques

Fourthly, prior studies in the literature do not adequately address the techno–economic aspects of a model for joint scheduling of distributed hydrogen fueling stations across the transportation network. As such, the opportunity for these stations to provide distributed ancillary services to the grid is not contemplated and studied in previous studies. In addition, there is a need for exploring various strategies that could promote the deployment of hydrogen fueling stations which is missing from the literature. Such strategies should aim to utilize the full benefit for the stations in order to magnify the overall profit of the investment.

Fifthly, the above–cited studies on the LOHC–based storage systems share common shortfalls for not considering: (i) integration of the LOHC system with the power grid, (ii) optimal sizing and scheduling to meet the transportation sector demand, and (iii) the opportunities for participation in the ancillary services market. Hence, the LOHC–based generation and storage plants should be sized and operated for joint applications in order to enhance the system rate of return.

Chapter 3
Analytical Size Estimation for Electrified Transportation Fueling Infrastructures

3.1 Introduction

The analytical models for size estimation of electrified transportation infrastructures are missing from prior studies in the literature. Such models would be required to promote the proliferation of electrified transportation around the globe. Such analytical models do not require any optimization solver [49]; thus, they can be developed at the backend of globally accessible website or software applications (e.g. available online financial and investment estimators), where the input data from everywhere around the globe is given to the model, and various sizing parameters related to each location are returned to the user as shown in Fig. 3.1. As shown in the figure, a platform could be publicly deployed for size estimation of EVFSs. The optimal size of the EVFSs has to be determined based on the location at which such stations are to be deployed. Accordingly, the public–domain input data of that location should be adopted for size estimation. As shown in Fig. 3.1,

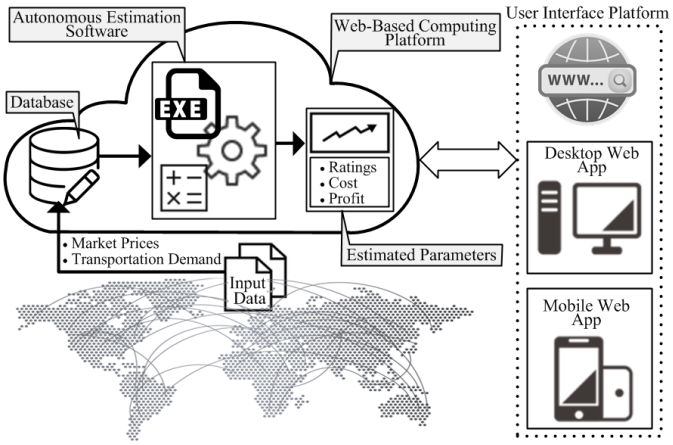

Figure 3.1: Globally accessible platform for size estimation of fueling stations.

the input data including market prices and transportation demand from around the globe can be given to the size estimation model, where a user interfaces with the model via websites, desktop software, or mobile applications. Accordingly, the size is estimated, and the estimation results are returned to the user for the location from which the input data are adopted. The output of the size estimation model would include the ratings of the EVFS's production and storage units, in addition to the calculated cost and profit. Such analytical sizing models can readily be implemented in a user friendly web–based environment, which does not have computational complexity.

To fill the gap between the existing and an analytical sizing approach, this research work presents a new formulation that can be utilized for sizing of both the battery–based and hydrogen–based EVFSs. In particular, the main contributions of this work are listed as:

1. The mathematical formulation for sizing of various components of an EVFS using public–domain data is presented. The proposed model aims to minimize the stations CAPEX while maximizing the net profit resulted from arbitrage opportunities in the electricity market and fuel sale to the transportation sector. The ratings of various components are expressed in terms of operation percentage using the proposed

formulation, and the desired ratings are selected at which the net profit reaches to the maximum point.

2. The models are developed such that they suit both the BEVs and FCEVs charging stations. Thus, the estimated parameters for both types of stations are returned with one set of input parameters from the user. This would allow the user to comparatively observe the size, cost, and profit quantities associated with both types of electrified transportation infrastructures.

3. The proposed models are developed in such a way that they do not require any optimization solver. As such, they can be developed at the backend of globally accessible platforms or software applications, where the input data from around the globe is given to the model, and various sizing parameters related to each location are returned to the user.

Historical operating data from real–world systems are utilized for numerical evaluation of the proposed formulation. The estimation error of the proposed model is analyzed in order to demonstrate the accuracy and efficacy of the proposed estimation methods.

3.2 Problem Description and Hypothesis

Deployment of EVFSs as the critical infrastructure is a prerequisite for the successful proliferation of FCEVs and BEVs. In such a case, it is imperative that these stations are properly sized to minimize the CAPEX and maximize the operating profit of the stations. This would, in turn, promote private investments in this sector. To that end, private investors are in need to have accessible analytical tools for the estimation of the ratings of the EVFSs and the rate of return depending on the electricity market and transportation demand in which the station is operated. Accordingly, this chapter aims to present a new

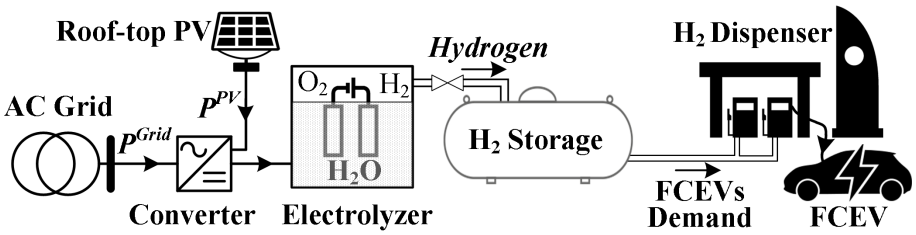

Figure 3.2: Schematic diagram for the main components of FCEVs fueling station.

analytical approach that would lead to the mathematical modeling for sizing of various components of a BEVs and hydrogen–based fueling stations using public–domain historical demand and market data local to the fueling station.

Fig. 3.2 shows a schematic diagram of an on–site hydrogen generation unit in a hydrogen fueling station. As shown in the figure, the electrolyzer that is used for hydrogen generation is coupled with the AC–grid through an AC–DC converter. The electrolyzer utilizes direct current to diffuse water molecules into the hydrogen and oxygen. Equation (3.1) below expresses the steady–state hydrogen generation quantity in terms of the input power to the electrolyzer [6]:

$$F_{Elz} = P_{Elz} \cdot \lambda_{Elz} \cdot \eta_{Elz}, \tag{3.1}$$

where, P_{Elz} and F_{Elz} represent the electrolyzer input power (MW) and hydrogen outflow (m^3/h); λ_{Elz} is the power to hydrogen conversion rate (m^3/MWh); and η_{Elz} is the electrolyzer efficiency in percentage. The electrolyzer can be integrated with renewable energy sources such as rooftop PV units across the fueling station. The produced hydrogen should be stored in a hydrogen storage unit that would supply energy to the FCEVs. In such a case, the following components are required to be sized in a hydrogen fueling station: the AC–DC converter, electrolyzer, and hydrogen storage. Without loss of generality, the PV panel is sized in this work based on the rooftop footprint at the station location.

Fig. 3.3, on the other hand, represents a schematic diagram for a BEVs fueling station.

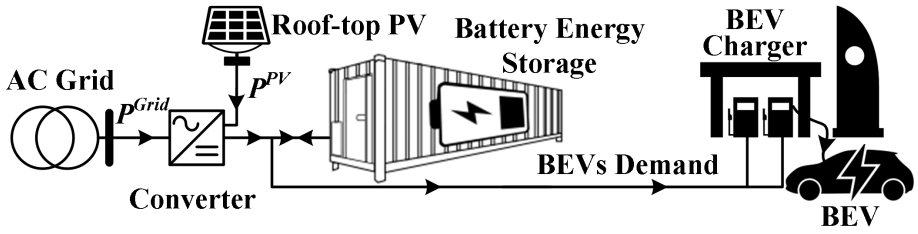

Figure 3.3: Schematic diagram for the main components of BEVs fueling station.

As shown in the figure, the station is composed of the following components that are to be sized: AC–DC converter and optional combined battery energy storage and on–site rooftop PV panels for local energy storage and generation. Here it is worth noting that BEV chargers can be energized directly from the AC grid directly and/or through the battery energy storage unit.

In what follows, the proposed sizing formulation is given, where each component of the fueling station is represented as a unit i that supplies the demand $D_i(t)$. The relationship between the unit's demand (i.e., output) and the input power is determined based on the unit's efficiency η_i and conversion factor λ_i.

3.3 Proposed Sizing Methodologies

This work proposes a new analytical estimation–based sizing approach for EVFSs. In particular, this section aims to size BEVs and FCEVs fueling stations that purchase power from the market and are equipped with optional on–site generation units. Where, the EVFSs are assumed in this work to deal with the wholesale electricity market and experience real-time pricing. Fig. 3.4 shows the process flow for size estimation of various components of EVFSs using the proposed model. As shown in the figure, the historical FCEVs/BEVs demand and electricity prices are input to the sizing estimator. Such data are location specific; i.e., they should be provided from the location at which the EVFSs are to be set up. The mathematical formulation for various components of the EVFSs is

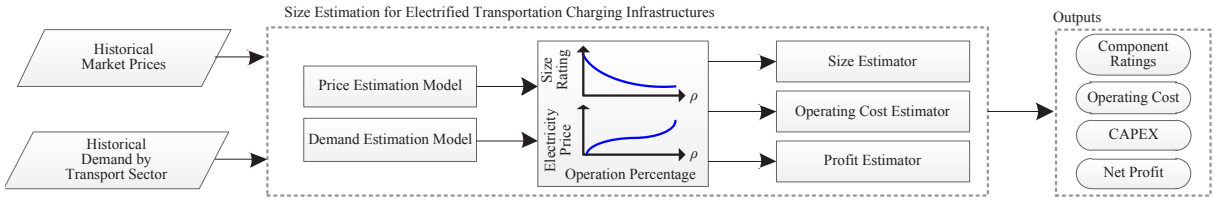

Figure 3.4: Proposed model for size estimation of various components of FCEVs and BEVs fueling stations using public–domain market data.

extracted based on the operation percentage. Accordingly, the component ratings, cost, and profit quantities are estimated using the given inputs. The final output would be the facility ratings, operating cost, CAPEX, and net profit; the net profit is computed considering the generated revenue while the operating cost and CAPEX values are deducted. The sizing of various components are decided that would maximize the system net profit.

It is worth noting that the following assumptions are made in development of the proposed model:

- The EVs demand data used for numerical studies are assumed to be forecasted [44]. In particular, such data represent the predicted probability for the EVs arrival across the day and throughout the week, in addition to the average demand over the months in one year [44].

- Historical electricity prices are inputted to the model. The model, then, assesses the probability of the production unit operation at the hours corresponding to the historical low electricity price instances.

- The EVFS is assumed to be owned and operated by a private investor in a competitive market environment. As a private asset, the EVFS is not subject to financial penalties for any unsatisfied demand although losing potential customers can adversely impact the service quality. Hence, the financial penalties for unsatisfied demand are not incorporated in this study.

- The proposed analytical sizing model in this work does not deal with the scheduling of individual EV demands, but rather it aims to size the EVFS components and storage plants that would supply the aggregated EVs demand. In the sizing application, the aggregated consumption pattern of EVs demand follows a rather predictable pattern with lower uncertainties [106]; this is contrary to the consumption pattern of individual vehicles which is associated with higher forecast inaccuracies. Hence, it is assumed that the forecasted EVs demand is accompanied with negligible uncertainties.

In the next sections, the proposed formulation for the analytical size estimation is given.

3.3.1 Modeling of Data Input

3.3.1.1 Demand Estimation Model

The EVFS demand, $D_i(t)$, is essentially a periodic signal with respect to the time of the day, week, and month [107, 108]. Due to the periodic nature of the demand, it can be modeled using Fourier series function, as follows:

$$D_i(t) = a_0 + \sum_{n=1}^{n=N} \Big(a_n Cos(\omega_n t) + b_n Sin(\omega_n t) \Big) \; \forall \; i \in I, \tag{3.2}$$

where a_o, a_n, and b_n are unknown coefficients that need to be estimated; I states the set of EVFS components; it is worth noting that the demand here refers to the power consumption by converter, storage, and electrolyzer (in case of hydrogen fueling stations). It is noteworthy that the estimated demand is not associated with uncertainties since actual historical data are utilized rather than forecast parameters. In (3.2) ω_n represents the periodic frequency of the demand signal as follows:

$$\omega_n = 2\pi h_n f \quad \forall \, n \in \{1, 2, 3, \cdots, N\}; \tag{3.3}$$

equation (3.3) indicates the demand as a function of the frequency component h_n with the fundamental frequency of f. Here it is worth noting that the number N – the order of the frequency components – are determined based on the analysis of the historical demand data. Equation (3.2) can be expanded as follows:

$$\begin{aligned} D_i(t) = a_0 + \Big(a_1 Cos(\omega_1 t) + a_2 Cos(\omega_2 t) + \cdots + a_N Cos(\omega_N t)\Big) \\ + \Big(b_1 Sin(\omega_1 t) + b_2 Sin(\omega_2 t) + \cdots + b_N Sin(\omega_N t)\Big) \forall\, i \in I; \end{aligned} \tag{3.4}$$

equation (3.4) can be expressed in the matrix form as:

$$D_i(t) = \begin{bmatrix} a_0 & a_1 & \dots a_N & b_1 & \dots b_N \end{bmatrix} \begin{bmatrix} 1 \\ Cos(\omega_1 t) \\ \vdots \\ Cos(\omega_N t) \\ Sin(\omega_1 t) \\ \vdots \\ Sin(\omega_N t) \end{bmatrix} \forall\, i \in I. \tag{3.5}$$

In order to determine the unknown coefficients in (3.5), the least error square (LES) technique is utilized. Where (3.5) can be stated in the matrix form as given in the following:

$$\boldsymbol{\Omega K} = \boldsymbol{D(t)} + \boldsymbol{e_d}; \tag{3.6}$$

where (3.6) is expanded to the following using simple conversion techniques [109]:

$$\boldsymbol{\Omega}^{tr} \boldsymbol{K}^{tr} \boldsymbol{K}\, \boldsymbol{\Omega} - 2\, \boldsymbol{\Omega}^{tr} \boldsymbol{K}^{tr} \boldsymbol{D(t)} + \boldsymbol{D(t)}^{tr} \boldsymbol{D(t)} = \boldsymbol{e}_{\boldsymbol{d}}^{tr} \boldsymbol{e_d}; \tag{3.7}$$

the unknown matrix in (3.7) is stated by $\boldsymbol{\Omega}$ to be determined towards minimizing the error

$\boldsymbol{e_d}$. Accordingly, the derivation of (3.7) versus $\boldsymbol{\Omega}$ is extracted that would result in:

$$2\,\boldsymbol{K}^{tr}\,\boldsymbol{K}\,\boldsymbol{\Omega} - 2\,\boldsymbol{K}^{tr}\,\boldsymbol{D(t)} = 0, \tag{3.8}$$

where $\boldsymbol{\Omega}$ can be expressed as follows:

$$\boldsymbol{\Omega} = \left[\left[\boldsymbol{K}^{tr}\,\boldsymbol{K}\right]^{-1}\boldsymbol{K}^{tr}\right]\boldsymbol{D(t)}. \tag{3.9}$$

3.3.1.2 Price Estimation Model

Electricity prices are volatile in the electricity market as set by the independent electricity system operator. Therefore, the average cost of the electricity purchased by an EVFS varies based on the EVFS operation hours across the year and can be given as follow:

$$E(\rho) = \frac{\sum_{t\in T}\left\{\min\limits_{h}\left(E_t^{Prc}\right)\right\}}{\rho\cdot h^{Ann}}\;\forall\, h = \rho\cdot h^{Ann} \tag{3.10}$$

where h is the product of the percentage of annual operation, ρ, and the annual hours h^{Ann} i.e., 8760 hours. The average value of the electricity prices in this work implies calculating the average of the minimum electricity prices across the year for a given operation hour percentage per annum. In this regard, lower operation percentage enables the EVFS to exploit the lower electricity prices in the market, and thus the average cost for the power purchase goes lower. On the other hand, higher operation percentage across the year leads to an increase in the average cost for the purchased electricity. Thus, the relationship between the average electricity purchase cost, E, and the annual percentage of operation, ρ, can be modeled as a polynomial function:

$$E(\rho) = \sum_{j=0}^{j=n}\nu_j\cdot\rho^j \quad \forall\, j\in J, \tag{3.11}$$

where ν_j states a set of unknown parameters in (3.11) that is to be estimated using the historical values of electricity prices and operation percentage, as follows:

$$E(\rho) = \begin{bmatrix} \nu_0 \, \nu_1 \, \ldots \, \nu_n \end{bmatrix} \begin{bmatrix} 1 & 1 \ldots & 1 \\ \rho_1 & \rho_2 \ldots & \rho_j \\ \vdots & & \\ \rho_1^n & \rho_2^n \ldots & \rho_j^n \end{bmatrix}, \tag{3.12}$$

In order to determine the unknown parameters in (3.12), the LES technique is utilized. Where (3.12) can be stated in the matrix form as given in (3.13):

$$\boldsymbol{\Psi \rho_e} = \boldsymbol{E(\rho)} + \boldsymbol{e_e}; \tag{3.13}$$

similar to the LES method demonstrated in (3.6)–(3.9), $\boldsymbol{\Psi}$ can be expressed as follows:

$$\boldsymbol{\Psi} = \left[[\boldsymbol{\rho}_{\boldsymbol{e}}^{tr} \, \boldsymbol{\rho}_e]^{-1} \, \boldsymbol{\rho}_{\boldsymbol{e}}^{tr} \right] \boldsymbol{E(\rho)}. \tag{3.14}$$

After estimating the demand and electricity prices, the model aims to determine the net profit, NP, of such stations, as formulated in the following:

$$NP(\rho) = \sum_{t \in T} R_t - O(\rho) - C(\rho)/LS + \sum_{t \in T} P_t^{RE} \cdot E^{Prc,Fit}, \tag{3.15}$$

where, LS denotes the lifespan of the fueling station. Equation (3.15) expresses the EVFS profit as a function of the station annual operation hour ρ, where the station operating cost $O(\rho)$ and the annualized CAPEX $C(\rho)/LS$ are deducted from the gross revenue. The parameters P_t^{RE} and $E^{Prc,Fit}$ represent the renewable power generation and the sale price associate with it. In (3.15), the station revenue R_t is calculated as the product of the

demand $D_i(t)$ and the fuel price V^{Prc} as stated in the following:

$$R_t = \sum_{t \in T} D_i(t) \cdot V^{Prc}. \tag{3.16}$$

In order to compute the net profit as formulated above, the station CAPEX and operating cost are to be estimated as described below.

3.3.2 CAPEX Estimation

The CAPEX of an EVFS system consists of the following costs: the converter cost (κ_i), storage cost (κ_{Sto}), energy dispenser cost (κ_{ED}), and the cost related to the implementation of the on–site renewable generation unit ($\kappa_{r,RE}$). The size of each component as mentioned above is estimated in the below sections that would minimize the total CAPEX. After sizing each component, the cost of the component is computed considering the $ value per unit of the component size. The CAPEX is then calculated by adding up the cost of each component.

3.3.2.1 Converter Unit

In general, the higher the percentage of operation (i.e., ρ) is, the smaller the size of the converter unit needs to be. This is because the same amount of demand can be met with a smaller converter once a longer generation time is utilized. Thereby, the size of the station converter unit varies as a multiplicative inverse function with respect to ρ, as stated below. The validity of this function is later confirmed in Section 3.4.

$$S_i(\rho) = \frac{\sum_{t \in T} D_i(t)}{\rho \cdot h^{Ann} \cdot \eta_i \cdot \lambda_i} \quad \forall\, i \in I, \tag{3.17}$$

where h^{Ann} represents the annual hours (i.e., 8760 hours), i refers to the station's converter and electrolyzer in case of hydrogen fueling stations; while it refers to the station's converter in case of BEVs fueling station. Equation (3.17) states that the sizing of any unit within the station depends on the demand, the operation hours, efficiency, and the energy conversion factor.

3.3.2.2 Energy Storage Unit

The energy storage unit is represented by the SOC equation in (3.18) indicating the energy balance at each time step t as a function of the storage input energy ($\eta^{Chg} \cdot S_i \cdot \lambda_i \cdot \eta_i \cdot \vartheta_t$), demand $D_i(t)$, and the dissipation rate $\gamma^{Dsp} \cdot SOC_t$.

$$SOC_{t+1} = SOC_t + \Big(\eta^{Chg} \cdot S_i(\rho) \cdot \lambda_i \cdot \eta_i \cdot \vartheta_t(\rho) - \frac{D_i(t)}{\eta^{Dhg}} - \gamma^{Dsp} \cdot SOC_t\Big) \cdot \Delta t \;\; \forall\, t \in T \wedge \forall\, i \in I; \tag{3.18}$$

as stated in (3.18), the storage input energy is the product of unit i capacity S_i, the unit efficiency η_i, conversion factor λ_i, and the operation probability ϑ_t. Where, η^{Chg} and η^{Dsp} denotes the charging and discharging efficiency, respectively; and γ^{Dsp} represents the storage dissipation rate. The EVFS storage aims to satisfy the demand of the vehicles at any time instant. Besides, exploiting the lower electricity price for fuel provision, known as the arbitrage, is aimed by the storage unit.

Equation (3.19) expresses the probability of the production unit operation, $\vartheta_t(\rho)$, at each hour based on the historical data of the electricity prices.

$$\vartheta_t(\rho) = \frac{\sum_{t \in T} \Lambda_{t,a}}{N_a} \;\; \forall\, a \in A, \tag{3.19}$$

where (3.19) shows the total operation hours over the number of years, N_a, of historical

data. Accordingly, the station operation state is given in (3.20) at each time step t:

$$\Lambda_{t,a} = \begin{cases} 1 \;\; \forall\, E_{t,a}^{Prc} \leq E_a^{BE}(\rho) \\ 0 \;\; \forall\, E_{t,a}^{Prc} > E_a^{BE}(\rho) \end{cases} \quad \forall\, t \in T \;\wedge\; \forall\, a \in A, \tag{3.20}$$

$$\text{where,} \quad E_a^{BE}(\rho) = \max\left\{\min_h \left(E_{t,a}^{Prc}\right)\right\} \;\; \forall t \in T \wedge \forall a \in A \wedge \forall\, h = \rho \cdot h^{Ann}. \tag{3.21}$$

As stated in (3.20), the station operates (i.e., $\Lambda_{t,a} = 1$) when the market price is below the break–even price (i.e., $E_a^{BE}(\rho)$) to ensure the system profitability; and it does not operate (i.e., $\Lambda_{t,a}= 0$) when the market price is above the break–even value. The break–even price is defined in (3.21) where h is the product of the desired utilization factor of the station ρ, and the annual hours h^{Ann}. Accordingly, the size of the storage device is defined as the product of the storage utilization and the difference between the maximum and minimum SOC over the annual time horizon.

$$SOC_{max} = \frac{1}{\mu^{SOC}} \cdot \Big(\max\{SOC_t\} - \min\{SOC_t\}\Big) \forall\, t \in T \wedge \forall\, \mu^{SOC} = SOC^{ub} - SOC^{lb}, \tag{3.22}$$

where SOC^{ub} and SOC^{lb} state the allowable upper and lower bounds of stored energy in the storage device.

3.3.2.3 Energy Dispenser Units

Based on the predicated EVs demand, one of the sizing parameters of EVFSs that would be calculated by the proposed sizing model is the number of energy dispensers. In particular, these represent the number of charging points and hydrogen dispenser hoses for BEVs and FCEVs fueling stations, respectively. The number of energy dispenser would be calculated to satisfy the maximum hourly arrivals of EVs across the year as follows:

$$N^{ED} = \max\{\mathcal{N}^{EV,Wek} \cdot \mathcal{P}(D^{Wek})\} \times \;\max\{\mathcal{P}(D^{Day})\} \cdot T^{Fil,Avg}, \tag{3.23}$$

where $\mathcal{P}(D^{Wek})$ and $\mathcal{P}(D^{Day})$ represent the EVs arrival probability per week and day, respectively; N^{ED} and $T^{Fil,Avg}$ denote the number of required energy dispensers by an EVFS and the average refueling rate of EVs, respectively; and $\mathcal{N}^{EV,Wek}$ indicates the number of served EVs per week.

After the determination of the various components, the CAPEX equation is given as:

$$C(\rho) = \kappa_{Sto} \cdot SOC_{max} + \sum_{i \in I} \kappa_i \cdot \frac{\sum_{t \in T} D_i(t)}{\rho \cdot h^{Ann} \cdot \eta_i \cdot \lambda_i} + N^{ED} \cdot \kappa_{ED} + \sum_{r \in R} \kappa_{r,RE} \cdot S_{r,RE} \quad (3.24)$$

where $\kappa_{r,RE}$ and $S_{r,RE}$ represent the CAPEX and the rated power of the renewable unit r, respectively; and κ_{ED} represents the energy dispenser CAPEX.

3.3.3 Operating Cost Estimation

The operating cost of the station is defined as the operation and maintenance cost of each unit within the station and the cost for electricity purchase from the market, as follows:

$$O(\rho) = \rho \cdot h^{Ann} \cdot \sum_{i \in I} \big(OC_i + E(\rho)\big) \cdot S_i(\rho) - \sum_{r \in R} S_{r,RE} \cdot \big(E^{Prc}_{t,a} - OC_{r,RE}\big) \; \forall \, t \in T \wedge \forall \, a \in A, \quad (3.25)$$

where OC_i denotes the operation cost of unit i, and $OC_{r,RE}$ denotes the operation cost of renewable unit r. Having the CAPEX and operating cost terms estimated, the net profit can be determined using (3.26).

$$\begin{aligned} NP(\rho) = & \sum_{t \in T} D_{i,t}(t) \cdot V^{Prc} - \rho \cdot h^{Ann} \cdot \sum_{i \in I} \big(OC_i + E(\rho)\big) \cdot \frac{\sum_{t \in T} D_i(t)}{\rho \cdot h^{Ann} \cdot \eta_i \cdot \lambda_i} \\ & - \frac{1}{LS} \cdot \left(\kappa_{Sto} \cdot SOC_{max} + \sum_{i \in I} \kappa_i \cdot \frac{\sum_{t \in T} D_{i,t}(t)}{\rho \cdot h^{Ann} \cdot \eta_i \cdot \lambda_i} + N^{ED} \cdot \kappa_{ED} + \sum_{r \in R} \kappa_{r,RE} \cdot S_{r,RE} \right) \\ & + \sum_{r \in R} S_{r,RE} \cdot \big(E^{Prc}_{t,a} - OC_{r,RE}\big) \; \forall \, t \in T \wedge \forall \, a \in A, \end{aligned} \quad (3.26)$$

In the next section, the numerical studies are conducted to evaluate the accuracy and feasibility of the proposed model in this section.

3.4 Numerical Results

The proposed sizing model for EVFSs is coded and evaluated using the MATLAB software package. The proposed model is evaluated at different operating percentages to find out the ratings that would yield the maximum net profit. The historical electricity prices is adopted from Ontario electricity market [110]. The FCEVs and BEVs demand data are adopted from [107, 108]. The required set of frequency components for estimating the FCEVs demand is found to be 84, while 20 polynomial order coefficients are considered for market price estimation. The simulation and modeling parameters are given for a lifespan of $LS = 15$ years as [6]:

1. **Electrolyzer:** Power to hydrogen conversion rate is considered as $\lambda_i = 360\ \mathrm{m}^3/\mathrm{MWh}$ with an efficiency rate of $\eta_i = 60\%$; a CAPEX of $\kappa_i = \$0.6\ \mathrm{M}\ /\mathrm{MW}$; and maintenance cost of $OC_i = \$2.05\ /\mathrm{MWh}$ [6].

2. **AC–DC Converter:** Power conversion rate is considered as $\lambda_i = 1$ with an efficiency rate of $\eta_i = 99\%$; a CAPEX of $\kappa_i = \$0.12\ \mathrm{M/MVA}$; and maintenance cost of $OC_i = \$0.41\ /\mathrm{MWh}$ [42].

3. **Energy Storage:** Hydrogen storage CAPEX and maintenance are considered as $\kappa_{Sto} = \$50/\mathrm{m}^3$ and $OC_i = 2\% \times \kappa_{Sto}/\ (8760 \times LS)\ \$/\mathrm{m}^3.\mathrm{h}$, respectively. The hydrogen charging and discharging efficiency of $\eta^{Chg} = \eta^{Dhg} = 99.5\%$ are considered [6, 104]. The battery energy storage CAPEX and maintenance are considered as $\kappa_{Sto} = \$1\,\mathrm{M/MWh}$ and $OC_i = 2.5\% \times \kappa_{Sto}/(8760 \times LS)\ \$/\mathrm{MWh}$, respectively. Besides, the battery energy storage charging and discharging efficiency is assumed to

be $\eta^{Chg} = \eta^{Dhg} = 92\%$ [6]. The dissipation rates of the studied storage systems is considered to be $\gamma^{Dsp} = 0.006\%$ [6].

4. **Energy Dispenser:** BEVs charging point dispenser CAPEX is considered to be κ_{ED}= \$ 25 k/charger [111], the average charging time per BEV $T^{Fil,Avg} = 20$ minutes, where the BEV charging price is considered to be $V^{Prc} = 145$ \$/MWh in this study [6]. The hydrogen energy dispenser hose is considered as κ_{ED} = \$ 75 k/dispenser [112], the average refueling time per FCEV is $T^{Fil,Avg} = 5$ minutes per fill [112], while the hydrogen sale price is considered to be $V^{Prc} = \$6$ /kg [6, 104].

5. **Rooftop Solar Panels:** A 160 rooftop PV panels of $S_{r,RE} = 300$ W/panel are assumed to be deployed at the stations. The PV CAPEX is given as $\kappa_{r,RE} = \$1300$ /kW and the maintenance is given as $OC_{r,RE} = 13\% \times \kappa_{r,RE}/(8760 \times LS)$ \$/kWh. The feed-in tariff price for the PV generation is considered as $E^{Prc,Fit} = \$200$ /MWh [113].

3.4.1 Model Validation

The accuracy of the proposed estimation techniques is evaluated by computing the Mean Absolute Percentage Error (MAPE) and the Standard Deviation of Absolute Percentage Error (SAPE), where SAPE is defined as follows:

$$\text{SAPE}_{T^*} = \sqrt{\frac{1}{H-1} \cdot \sum_{g \in G} (\text{APE}_g - \text{MAPE}_{T^*})^2}, \tag{3.27}$$

where T^* indicates the SAPE period (i.e., hourly, daily, weekly, etc.), H states the number of hours within T^*, and G expresses the set of hours within the T^* period.

Fig. 3.5 shows the hourly, daily, and monthly hydrogen and electric demand by the FCEVs and BEVs, respectively, used for simulation studies, which are adopted from [107] and [108]. As shown in Figs. 3.5 (a) and (b), demand changes on an hourly basis while

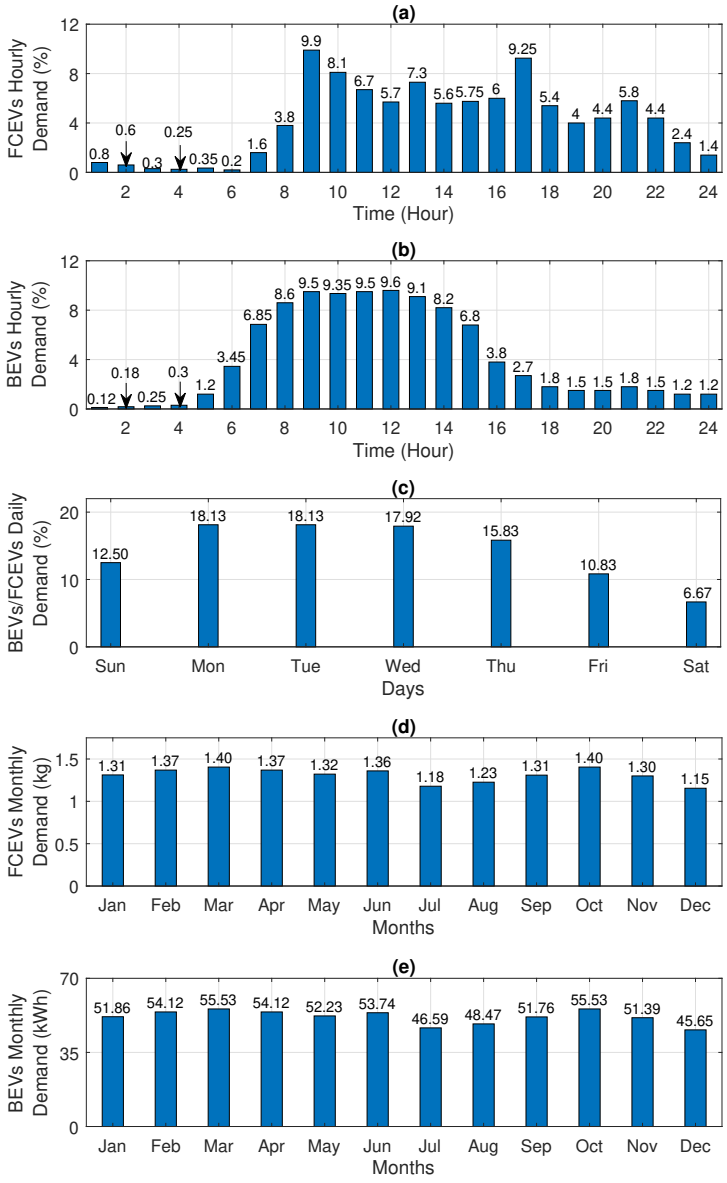

Figure 3.5: (a): FCEVs hourly demand probability, (b): BEVs hourly demand probability, (c): BEVs/FCEVs daily demand probability, (d): FCEVs monthly demand, and (e): BEVs monthly demand.

it is minimum early in the morning and late at night, maximum during rush hours, and medium for the rest of the times. In addition, Figs. 3.5 (c)–(e) indicate the daily and monthly changes in the demand.

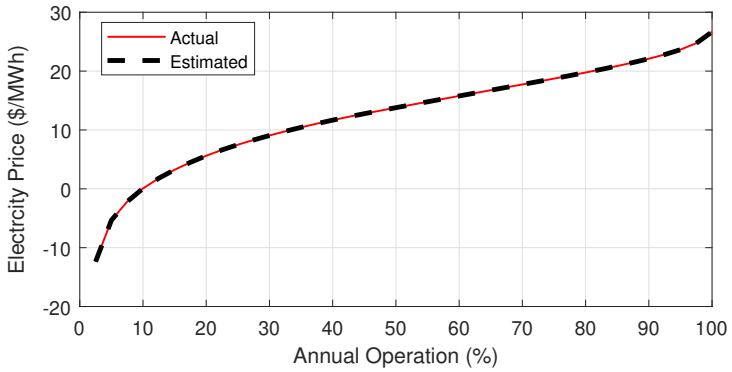

Figure 3.6: Estimated and actual average electricity prices.

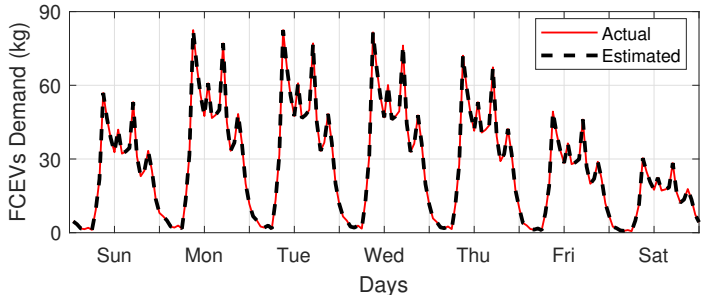

Figure 3.7: Estimated and actual FCEVs demand for a typical week.

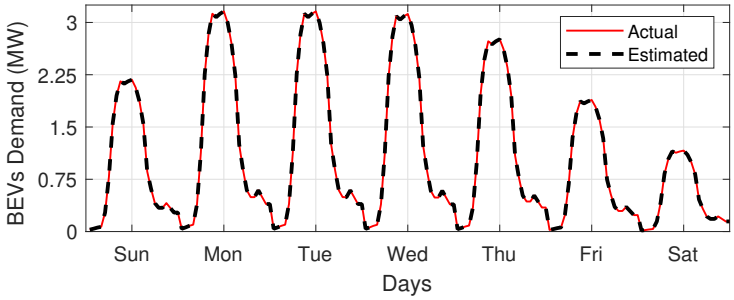

Figure 3.8: Estimated and actual BEVs demand for a typical week.

Figs. 3.6, 3.7, and 3.8 depict the actual/estimated values of electricity price, FCEVs demand, and BEVs demand, respectively, using the proposed method for a typical week out of the studied year. The results show that the estimated and the actual curves are almost a perfect match, indicating the accuracy of the proposed estimation model. Here

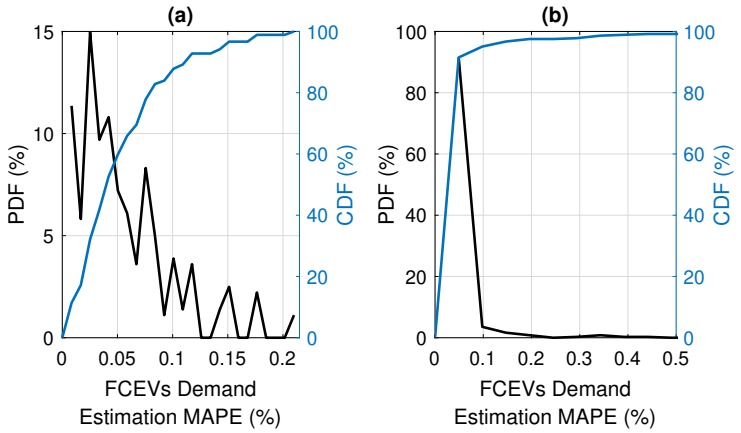

Figure 3.9: FCEVs demand estimation MAPE under (a): proposed time–based Fourier series, and (b): Neural Network.

it is worth noting that the estimated curve does not represent forecast results, thereby is not associated with the forecast uncertainties. The average electricity prices in this work implies calculating the average of the annual minimum electricity prices for a given annual operation percentage. Fig. 3.6 shows that the average electricity prices are negative at low annual operation percentage. This is due to the surplus power generation in Ontario that causes low and even negative prices in the wholesale electricity market [110]. Utilizing such negative or low electricity prices would enhance the overall profit of the EVFSs. Nonetheless, at higher annual operation percentages, when the EVFS tends to operate more over the year, the average of the utilized market prices increases since the model has to utilize higher price instances as well.

Fig. 3.9 shows the Probability Density Function (PDF) and Cumulative Density Function (CDF) of the demand MAPE using the proposed method as compared with the Neural Network technique. While the estimation error is small under all methods, the MAPE value using the proposed model is considerably lower than the one under the Neural Network method. In addition, Fig. 3.10 shows that the SAPE value under the proposed model is lower than the one under the Neural Network method.

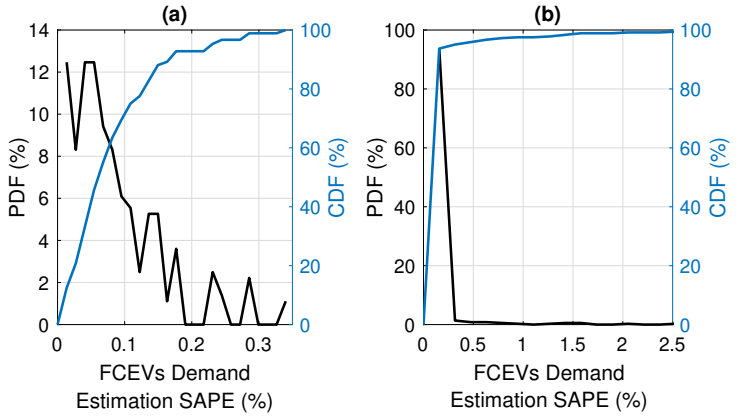

Figure 3.10: FCEVs demand estimation SAPE under (a): proposed time–based Fourier series, and (b): Neural Network.

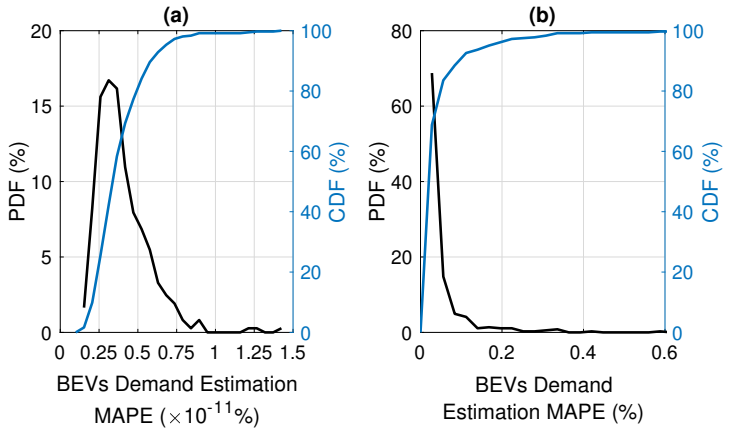

Figure 3.11: BEVs demand estimation MAPE under (a): proposed time–based Fourier series, and (b): Neural Network.

Figs. 3.11 and 3.12 represent the MAPE and SAPE values of the BEVs demand estimation using the proposed model compared to common artificial intelligence based technique e.g. Neural Network technique. The Neural Network is selected as a feed-forward network with one hidden layer of 30 neurons. Where, Neural Network samples are divided into 70% for training, and 15% each for validation and testing. The results show that the MAPE and SAPE quantities are negligible under the proposed model indicating the accuracy of the proposed estimation model compared to the Neural Network technique.

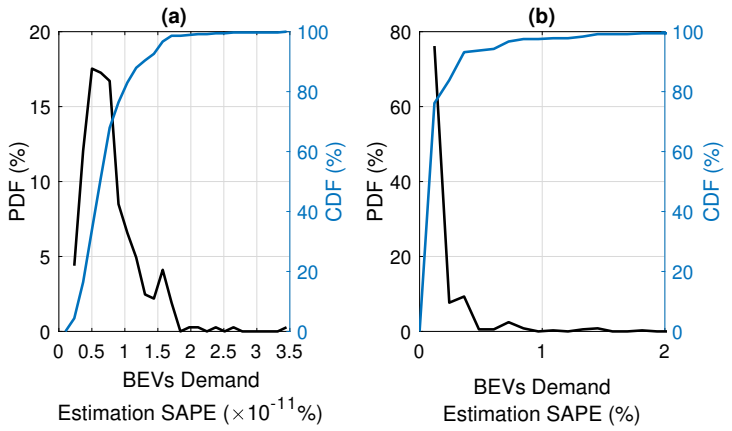

Figure 3.12: BEVs demand estimation SAPE under (a): proposed time–based Fourier series, and (b): Neural Network.

3.4.2 FCEVs Fueling Station Size Estimation

The FCEVs hydrogen station used for numerical studies aims to serve a reasonable number of FCEVs per week (i.e., 3500 FCEVs/week) with the consumption trend depicted in Fig. 3.5. In such a case, the hydrogen supply from the station comes to 650 kg/day on average. Moreover, it is worth mentioning that the maximum probability of BEVs arrival per day is found to be 18.3% as shown in Fig. 3.5 (c), while the maximum probability of FCEVs arrival per hour is found to be 9.9% as shown in Fig. 3.5 (a). Given that the EVFS is designed to serve 3500 FCEVs per week and the average fueling time for FCEVs is 5 minutes [112], the number of required hydrogen dispensers is calculated using (3.23) that would be equal to 6. Fig. 3.13 shows the profit, CAPEX, operating cost, and sizing characteristic curves for the hydrogen fueling stations in terms of the percentage of operation. Given that the main criterion for sizing in the proposed model is to maximize the net profit, the component sizing would be considered optimal where the system net profit is maximized.

As shown in Fig. 3.13 (a), the system net profit increases with the increase of the percentage of operation from the lower bound to the mid point. The figure shows that the curve is almost flat between 55 to 75 operation percentages; it then tends to decrease when

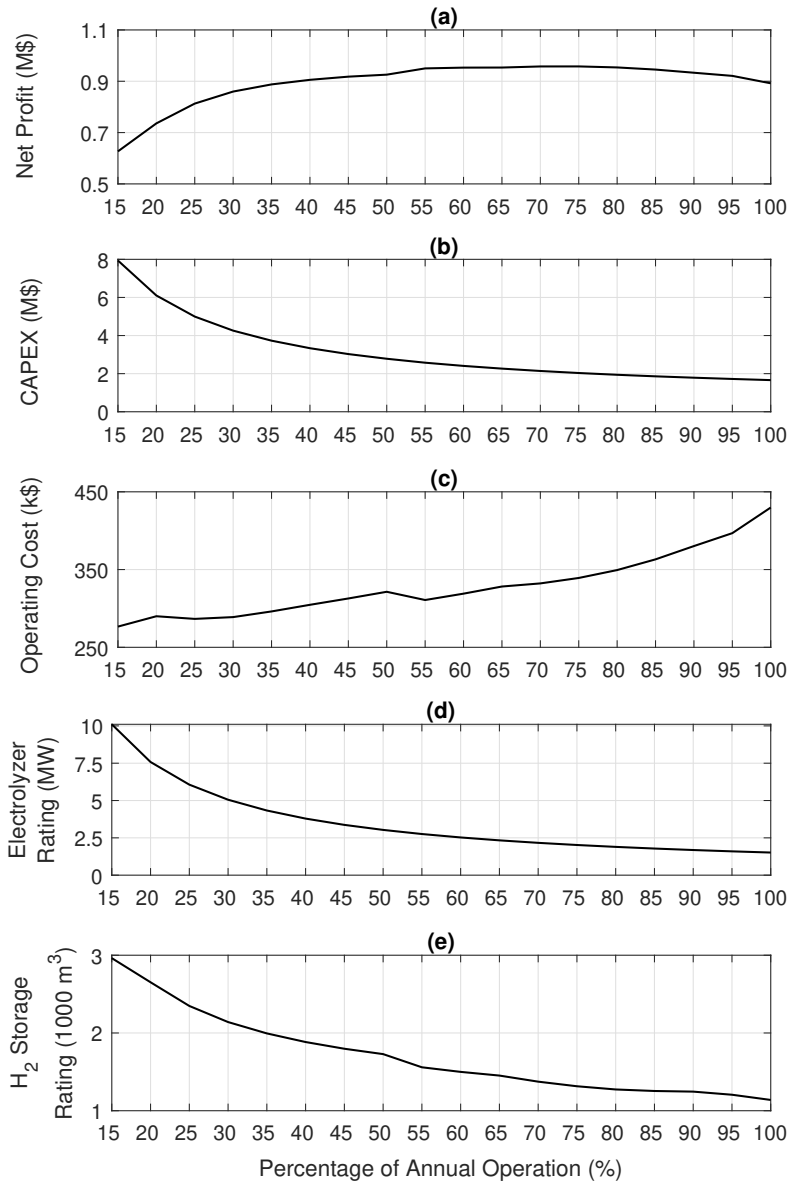

Figure 3.13: Estimated parameters of the FCEVs fueling station using the proposed model; (a): Annual net profit, (b): CAPEX, (c): Operating cost, (d): Electrolyzer rating, and (e): Storage rating.

the percentage of operation is more than 75%. The total cost is composed of two components as follows: (i) the energy purchase cost and (ii) the initial investment. Operation at lower percentages necessitates large components so that the system would be able to meet the demand in a shorter period of time. Operation at higher percentages, on the other

hand, implies that smaller components can meet the demand as shown in Figs. 3.13 (d) and (e). In such a case, the CAPEX tends to decrease as shown in 3.13 (b). However, the facility operator would have to make a larger payment for power purchase from the market at higher operation percentages; as depicted in Fig. 3.13 (c) the operating cost increases with the increase of the operating percentages. This is because the facility utilizes lower market price instances over the year, but as it operates more throughout the year, it has to utilize higher market price instances as well. As such, an optimal trade off would have to be determined aiming at profit maximization, which happens at percentage of operation between 55% to 75% as shown in Fig. 3.13 (a).

3.4.3 BEVs Fueling Station Size Estimation

A similar analysis as the one conducted in Section 3.4.2 is performed for BEVs station optimal sizing, and the results are presented in Fig. 3.14. The BEVs station used for numerical studies aims to serve 3500 BEVs per week with the consumption trend depicted in Fig. 3.5. In such a case, the power supply from the station comes to 26 MWh/day on average. Using (3.23), it is found that the required charging points to be deployed in the BEVs charging stations is 21. This is because the maximum probability of BEVs arrival per day is found to be 18.3% as shown in Fig. 3.5 (c), and the maximum probability of BEVs arrival per hour is found to be 9.6% as shown in Fig. 3.5 (b). In addition, the EVFS expects the arrival of 3500 BEVs per week and the average fueling time for BEVs would be 20 minutes [111]. Fig. 3.14 (a) shows that the net profit tends to increase with an increase in the percentage of operation from lower bound of 15% up to 70%. Once the operation rate further increases from 70% to 100%, the profit tends to decrease. Fig. 3.14 (b) shows that the CAPEX of the BEV station shrinks at higher operation percentages due to a decrease in the cost of the battery charger and the storage components (see Figs. 3.14 (d) and (e)). At higher operation percentages, however, the facility operator has to utilize

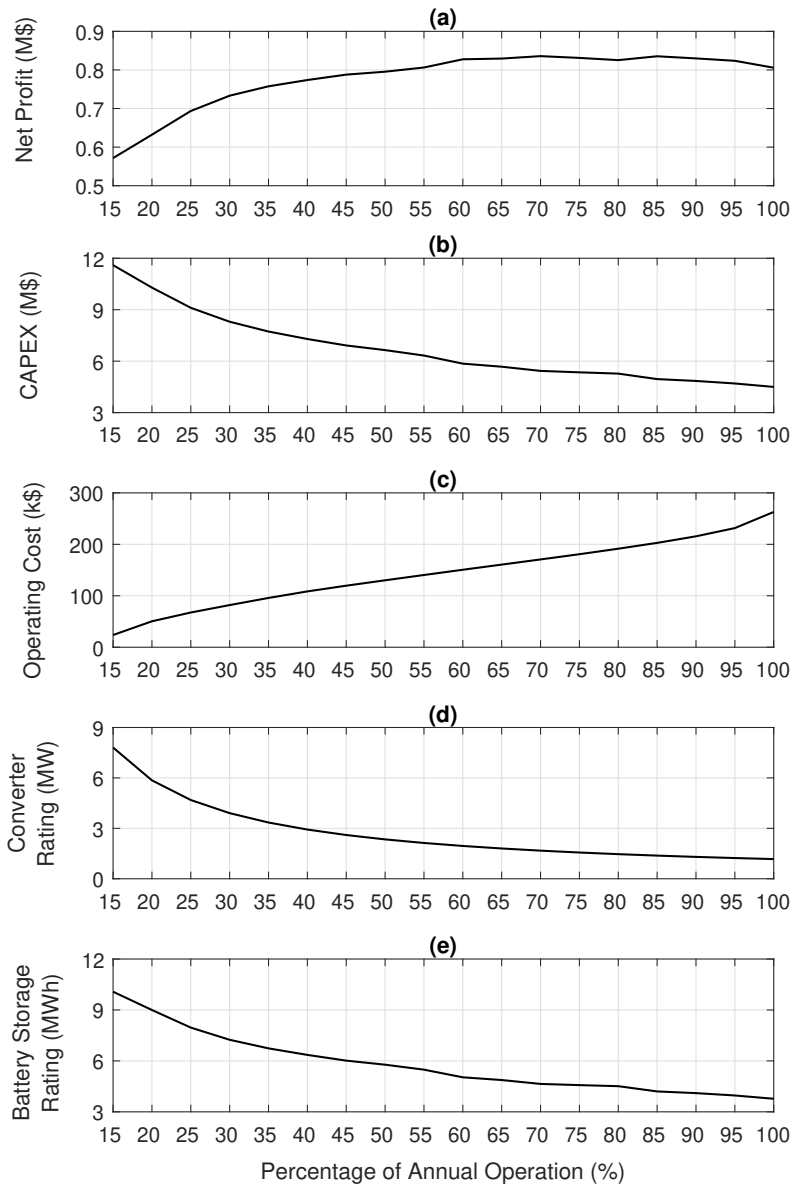

Figure 3.14: Estimated parameters of the BEVs fueling station using the proposed model; (a): Annual net profit, (b): CAPEX, (c): Operating cost, (d): Converter rating, and (e): Storage rating.

higher market prices, and thus, the cost of energy purchase tends to increase as shown in Fig. 3.14 (c). As such, a balance has to be made between the cost of the components and the cost paid for the energy purchase from the market. Fig. 3.14 (a) represents that such

Table 3.1: Optimal Ratings of FCEVs and BEVs Fueling Station Components

FCEVs Fueling Station	BEVs Fueling Station
ρ= 75%	ρ= 70%
$NP(\rho)$= \$0.9578 M	$NP(\rho)$= \$0.836 M
$C(\rho)$= \$2.034 M	$C(\rho)$= \$5.43 M
$O(\rho)$= \$339.2 k /year	$O(\rho)$= \$170.6 k /year
$E(\rho)$= \$18.22 /MWh	$E(\rho)$= \$17.73 /MWh
$P_{Elz} = S_{Con}$ = 2 MW/MVA	S_{Con}= 1.673 MVA
SOC_{max}= 1315 m^3	SOC_{max}= 4.65 MWh
N^{ED}= 6	N^{ED}= 21

a balance is made at operation between 65% to 70% when the net profit maximizes.

The final optimum ratings of the FCEVs and BEVs fueling stations components are extracted from Figs. 3.13 and 3.14, and the results are reported in Table 3.1.

3.4.4 Impact of PV Panel Implementation

In order to evaluate the impact of PV panels implementation on the EVFS net profit, the size estimation for the EVFS are evaluated without considering rooftop PV panels. Then, it is compared with the results given in Sections 3.4.2 and 3.4.3 for the FCEVs and BEVs fueling stations, respectively. It is found that the sizing results is neither sensitive to existence of the PV panels nor adding considerable cost to the EVFS CAPEX. The PV panels implementation would not add a financial burden to the operator of the EVFSs, but rather they can enhance the system net profit. For instance, implementing the PV panels within the EVFS would increase the CAPEX by \$ 62.4 k. However, the existence of PV panels would reduce the dependence of EVFSs on the grid electricity. Therefore, the OPEX would decrease by \$ 13.33 k per year. This leads to a higher net profit by \$ 9.13 k per annum when compared with the case without PV panels.

3.5 Discussion and Summary

This chapter presents analytical approaches for the application to the size estimation of electric and hydrogen–based fueling stations as the two major foundations for electrified transportation. The mathematical formulation for sizing of various components of the fueling stations using public–domain market data is presented. The proposed models are developed in such a way that they do not require any optimization solver. As such, they can be developed at the backend of globally accessible websites or software applications, where the input data from everywhere around the globe is given to the model, and various sizing parameters related to each location are returned to the user. As such, the proposed analytical models in this work can be utilized to promote the proliferation of electrified transportation at a global scale. Historical operating data from real–world systems are utilized for numerical evaluation of the proposed formulation. The accuracy of the proposed estimation model is analyzed using the MAPE and SAPE quantities and validated as compared with the artificial intelligence–based methods; where, the estimated parameters are not forecasted, thereby not associated with forecast uncertainties. Various components of the FCEVs and BEVs fueling stations are sized using the proposed sizing model. The results indicate that a trade–off has to be made between capital and operation costs in order to maximize the annual net profit while meeting the FCEVs/BEVs demand. It is demonstrated that the optimal value for the operation percentage can be estimated using the proposed model, and components can be sized accordingly towards maximizing the net profit.

Chapter 4
BEB Energy Consumption Model based on Probabilistic Synthetic Speed Profile

4.1 Introduction

Operating range and energy consumption are primary factors in determining EBs' operating strategy and cost analysis [65]. EBEC has high economic and ecological importance as a key parameter in determining the fuel cost and the GHG emissions from PBT [57]. Appropriate estimation of EBEC is a vital requirement for their planning, deployment, and required charging infrastructure [63]. The speed profile for EBs is one of the main factors that impacts the EBEC, and should be available for the accurate assessment of the EBEC. To that end, in this chapter a probabilistic model is applied to generate synthetic speed profiles using basic information of the EB trip (i.e., trip time, distance, and stop locations). This model is anticipated as a practical alternative to overcome the unavailability of real–world speed profiles data, in addition to EBEC literature gap with respect to: 1) the requirement of high time-resolution speed profiles which are difficult to obtain due to

lack of operational data and high associated costs; 2) the inconsideration of complexity and variations of extensive real-world operational conditions; and 3) the dependence on typical driving cycles that lack the randomness behaviour in speed and uncertainty in energy demand. The proposed probabilistic model of EBEC considers route characteristics, traffic conditions, weather conditions, and the operation of HVAC systems. Using such model, PBT planners can accurately assess the energy consumption characteristics of EBs at different operating conditions. Hence, they link EBs' feasibility to real-world performance and facilitates accurate design of the on board batteries and charging infrastructure. To that end, Table 4.1 presents the definition of the proposed model indices, sets, parameters, and variables.

Table 4.1: Chapter 4 Nomenclature

A. Indices

s	Indices for designated bus stops.
j	Indices for generated speed profile.
t	Indices for time step.
n	Indices for sections within a speed profile.

B. Sets

$\mathcal{S}$	Set of designated bus stops for a given route.
$\mathcal{J}$	Set of generated speed profiles.
$\mathcal{N}_j^{Stp}$	Set of actual bus stops for speed profile j.
Υ^{Stt}	Set of different possible combinations of bus stop states by an electric bus (EB).
Λ_j^{Stt}	Set of EB stop states at each bus stop s for speed profile j.
$\mathcal{T}$	Set of speed profile time steps.
$\mathcal{T}_n$	Set of section n travel time steps.
$\mathcal{T}_d$	Set of section n dwelling time steps.
$\mathcal{T}^+, \mathcal{T}^-$	Set of acceleration and deceleration time instants.
X_n	Set of generated speed values within section n.

C. Parameters

N_s	Number of designated bus stops for a route.
N_j^{Stp}	Number of actual stops and speed profile sections within the generated speed profile j.
n_t	Number of the speed profile time steps.
Δt	Speed profile time step resolution (s).
$\lambda_{s,j}^{Stt}$	Binary state representing the EB stop status at bus stop s for speed profile j.
ϱ_s^{Stp}	Probability of EB to stop at bus stop s (%).

Table 4.1: Chapter 4 Nomenclature ... continued

$\boldsymbol{\chi}_j^{Stt}$ Probability of Λ_j^{Stt} stop states combination (%).

$T_n^{Stp,0}$ Randomly generated EB travel time for section n (s).

$\Delta t_n^{Stp,0}$ Randomly generated EB dwelling time after section n (s).

v/c Ratio of traffic volume v, to roadway practical capacity c.

D^{Trp} Trip distance (m).

$T^{Trp,N}$ Nominal trip time (s).

V^{Avg} Trip average velocity (m/s).

T_n^{max}, T_n^{min} Maximum and minimum travel time for section n, respectively (s).

$\Delta t_{max,n}^{Stp}$ Maximum dwelling time after section n (s).

$\Delta t_{min,n}^{Stp}$ Minimum dwelling time after section n (s).

D_n^{Stp} Section n distance (m).

x^{max} Roadway maximum free flow speed (m/s).

ξ^{Avg} Average roadway velocity factor (%).

x_t^0 Randomly generated speed at time step t (m/s).

x^{max}, x^{min} Maximum and minimum speed limits (m/s).

a^{Acc}, a^{Dec} EB acceleration and deceleration limits (m/s^2).

c_d, f_r EB drag and rolling resistance coefficient.

A^F EB frontal surface area (m^2).

m_t EB mass weight at time t (kg).

g Gravitational force (m/s^2).

ρ^{Air} Air density (kg/m^3).

η^{Bat} EB battery discharge efficiency (%).

η^{Reg} EB regenerative braking efficiency (%).

m^{Air} Mass of air inside the EB (kg).

C_p Air specific heat capacity (kJ/kg K).

k^s Temperature set point inside the EB (K).

k^{ub}, k^{lb} Comfort temperature upper–bound and lower–bound range, respectively (K).

R_{eq} EB absolute thermal resistance (K/W).

L^{Win}, L^{Chs} EB windows and chassis thickness (m).

A^{Win}, A^{Chs} EB windows and chassis area, respectively (m^2).

u_c^{Win}, u_c^{Chs} EB windows and chassis thermal conductivity, respectively (W/m K).

A, A^{dor} EB total surface and door area, respectively (m^2).

h_c^{Ext}, h_c^{Int} EB external and internal convective heat transfer coefficients (W/m^2 K).

C_A Air flow coefficient (m^3/s)/(m^2 Pa$^{0.5}$).

R_p Pressure factor (Pa).

ψ^{Vnt} EB ventilation requirement (%).

$\dot{V}^{Hvac}$ HVAC air flow rate (m^3/s).

h^{Pas} heat gain per passenger (W).

η^{COP} HVAC system coefficient of performance.

Q_R^{Hvac} HVAC rated power (kW).

D. State Variables

$\phi(d_t)$ Route grade at distance d_t (rad).

κ_t Dwelling time and traffic stops indicator/differentiator.

Table 4.1: Chapter 4 Nomenclature ... continued

F_t^{Trc}	EB traction force at time t (N).
k_t^{EB}	EB internal temperature at time t (K).
k_t^{Ext}	EB external temperature at time t (K).
β_t^{Pas}	Passengers number at time t.
Q_t^{Hvac}	HVAC system thermal power at time t (kW).
Q_t^{Los}	Conductive and convective thermal losses at time t (kW).
Q_t^{Inf}	Infiltration losses at time t (kW).
Q_t^{Vnt}	Ventilation losses at time t (kW).
Q_t^{Pas}	Passenger heat gain at time t (kW).
V_t^{Inf}	Air infiltration flow rate (m^3/s).
γ_t	HVAC cooling/heating operation mode indicator.
P_t^{Hvac}	HVAC power consumption at time t (kW).
P_t^{Aux}	Auxiliary power consumption at time t (kW).
P_t^{Fan}	HVAC fan Power consumption at time t (kW).
v_t^{Fan}, i_t^{Fan}	HVAC system's fan voltage (V) and current (A) at time t, respectively.
E^{Trc}	EB total traction energy (kWh).
E^{Hvac}	Total HVAC consumption within a trip (kWh).
E. Optimization Variables	
T_n^{Stp}	EB travel time within section n (s).
Δt_n^{Stp}	EB dwelling time after section n (s).
T^{Trp}	Variable trip time according to traffic flow condition (s).
V_n^{Avg}	Section n average speed (m/s).
x_t	Generated speed at time step t (m/s).
$\dot{x}_t$	EB acceleration at time t (m/s^2).
d_t	EB covered distance at time t (m).

4.2 Probabilistic Synthetic Speed Profile Model

The speed profile for EBs is essentially random, where each single trip results in a different speed profile according to the traffic conditions, driver behaviour, and passenger boarding and/or alighting. Nonetheless, the speed profile for an EB on a specific route attains some common characteristics such as the trip time, maximum speed limit, trip distance, and the designated locations of bus stops. In this sense, and in order to overcome the need for a set of high time-resolution speed data to assess the EBEC, this work aims to propose a model that generates speed profiles, which mimic the bus speed behaviour. In particular,

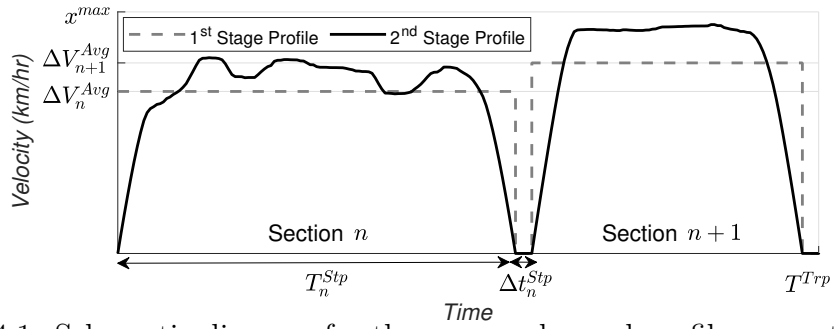

Figure 4.1: Schematic diagram for the proposed speed profile generator model.

the following data is required to be inputted to the proposed model:

1. Trip distance (D^{Trp}) and nominal trip time ($T^{Trp,N}$).
2. Stop location(s) i.e., distance between bus stops (D_n^{Stp}).
3. Probability of an EB to stop at each designated bus stop (ϱ_s^{Stp}).
4. Traffic condition parameter (v/c). Where, the traffic condition is incorporated in the proposed model as a constraint, as such the traffic condition parameter impacts the simulated trip time. For instance, heavy traffic condition will lead to higher trip time, and vice versa.
5. Maximum (T_n^{max}) and minimum (T_n^{min}) dwelling time of EBs at bus stops.
6. Maximum acceleration (a^{Acc}) and deceleration (a^{Dec}) of the EB.
7. Maximum (x^{max}) and minimum (x^{min}) velocity of the simulated route.

Fig. 4.1 illustrates the proposed mechanism for generating the speed profile. As shown in Fig. 4.1, the predefined bus trip time is divided into sections based on the number of bus stops. Each section n has its own average speed, V_n^{Avg} and dwelling time at the bus stop, Δt_n^{Stp}. In this regard, the proposed model consists of two stages. The first stage aims to allocate the time of each speed profile section, T_n^{Stp}, in addition to the EB

dwelling time, Δt_n^{Stp}, between two consecutive sections. The average speed profile between each two consecutive bus stops is determined in the first stage based on three predefined parameters: 1) trip time, 2) trip distance, and 3) number of bus stops the EB might have. Those parameters are utilized to formulate the first stage constraints as shown in Section 4.2.1. Here it is worth noting that the EB might not stop at each located bus stop. In this regard, the number of bus stops an EB might have in each trip is determined based on a probabilistic model described in Section 4.2.1. The second stage utilizes the output of the first stage (i.e., average speed in each section n) to randomly generate a speed profile, as shown in Fig. 4.1, which satisfies the first stage average speed and the EB acceleration and deceleration limits. The following two subsections elaborate on the details of the proposed mechanism for generating the speed profile.

4.2.1 Stage 1: Evaluating Bus Stops Probability, Average Speed, and Dwelling Time

The set of designated bus stops for a given route can be expressed as:

$$\mathcal{S} = \Big\{1, 2, 3, \ldots, s, \ldots, N_s\Big\}. \tag{4.1}$$

Based on the passenger boarding and/or alighting requirements, a bus may choose to skip on-route stops during trips (i.e., EB may not stop at each designated stop). In this regard, the set of actual number of bus stops and speed profile sections during a trip for a generated speed profile j is defined as:

$$\mathcal{N}_j^{Stp} = \{1, 2, 3, \ldots, n, \ldots, N_j^{Stp}\} \quad \forall\, j \in \mathcal{J} \wedge N_j^{Stp} \leq N_s, \tag{4.2}$$

where, N_j^{Stp} denotes the number of actual stops and speed profile sections within the generated speed profile j. The N_j^{Stp} might be smaller than the number of designated bus

stops, if the EB skip bus stops. Otherwise, the N_j^{Stp} would be equal to the number of designated bus stops N_s. The number of actual bus stops of each generated speed profile, N_j^{Stp}, is modeled using a probabilistic model, given that EBs stops is based on the stochastic nature of passengers alighting/boarding process at each bus stop. Where, $\lambda_{s,j}^{Stt}$ is a binary state representing the EB stop state for speed profile j; it equals one when the EB stops at the designated bus stop s, and it is zero otherwise. It is also noted in (4.2) that the number of speed profile sections equals the number of bus stops. Therefore, the number of actual stops for the speed profile j is given as the summation of the EB stops state, $\lambda_{s,j}^{Stt}$:

$$N_j^{Stp} = \sum_{s \in \mathcal{S}} \lambda_{s,j}^{Stt} \quad \forall\, j \in \mathcal{J} \;\wedge\; \forall\, \lambda_{s,j}^{Stt} \in \Lambda_j^{Stt} \;\wedge\; \forall\, \Lambda_j^{Stt} \in \Upsilon^{Stt}, \tag{4.3}$$

where, Υ^{Stt} is the EB set of different possible combinations of bus stop states, ($\Upsilon^{Stt} = \{\Lambda_j^{Stt}\}$), and different j combination of EB stop states, Λ_j^{Stt}, is given as follows:

$$\Lambda_j^{Stt} = \left\{\lambda_{1,j}^{Stt}, \lambda_{2,j}^{Stt}, \ldots, \lambda_{s,j}^{Stt}, \ldots, \lambda_{N_s,j}^{Stt}\right\} \quad \forall\, s \in \mathcal{S} \wedge \forall\, j \in \mathcal{J}. \tag{4.4}$$

The joint probability of each possible combination j could be expressed as the product of the bus stops' probabilities and is stated as:

$$\begin{aligned} \boldsymbol{\chi}_j^{Stt} &= \prod_{s \in \mathcal{S}} \left(\varrho_s^{Stp} \cdot \lambda_{s,j}^{Stt} + (1 - \varrho_s^{Stp}) \cdot \overline{\lambda_{s,j}^{Stt}} \right) \\ \forall s \in \mathcal{S} \wedge \forall j \in \mathcal{J} \wedge \forall\, \lambda_{s,j}^{Stt} &\in \Lambda_j^{Stt} \wedge \forall\, \Lambda_j^{Stt} \in \Upsilon^{Stt}, \end{aligned} \tag{4.5}$$

where, ϱ_s^{Stp} is the probability for the bus to stop at designated stop s; and $\overline{\lambda_{s,j}^{Stt}}$ is the complement state of $\lambda_{s,j}^{Stt}$.

The problem in the first stage is formulated mathematically as an optimization model. Equation (4.6) represents the objective function of the developed optimization model. As shown, in order to preserve the randomness of the generated average speed profile, equation

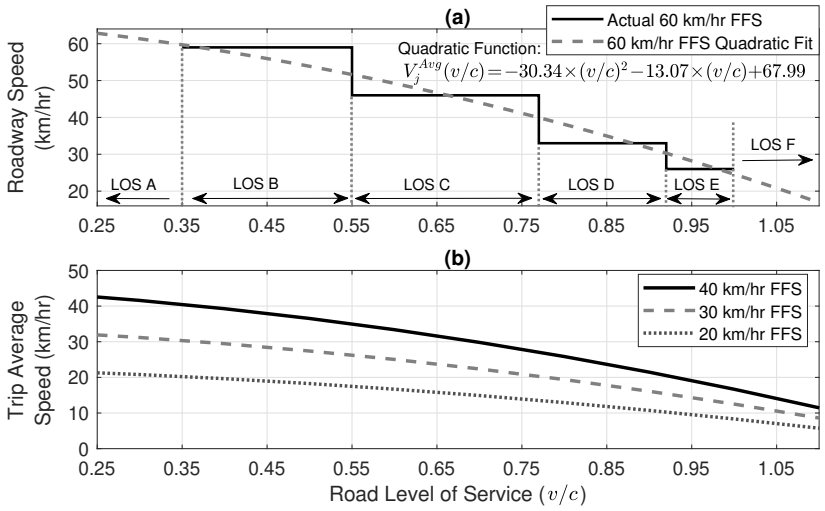

Figure 4.2: Speed versus different LoS, (a) standard roadway 60 km/h FFS, (b) at different trip's average speed.

(4.6) is formulated to minimize the deviation between: 1) the randomly generated time, $T_n^{Stp,0}$, and T_n^{Stp} for each section n, and 2) the random generated dwelling time, $\Delta t_n^{Stp,0}$, and Δt_n^{Stp} between two consequent sections.

$$\text{Min.:} \sum_{n \in \mathcal{N}_j^{Stp}} \left(T_n^{Stp} - T_n^{Stp,0}\right) + \left(\Delta t_n^{Stp} - \Delta t_n^{Stp,0}\right) \quad \forall\, j \in \mathcal{J}. \tag{4.6}$$

The objective function in (4.6) is subjected to the time of the EB trip, where the summation of the trip sections' travel times and dwelling times is constrained to the trip time as follows:

$$\sum_{n \in \mathcal{N}_j^{Stp}} \left(T_n^{Stp} + \Delta t_n^{Stp}\right) = T^{Trp}. \tag{4.7}$$

It is noteworthy that the trip time, T^{Trp}, varies according to the traffic flow conditions, which is known as the roadway LoS. The LoS, (v/c), is defined as the ratio of traffic volume, (v), to roadway practical capacity (c) [114]. Fig. 4.2 (a) shows different roadway

LoS (i.e., LoS A - F) with an average of 60 km/h Free Flow Speed (FFS) [114]. As shown in Fig. 4.2 (a), the LoS relation with the roadway speed is estimated using a quadratic function. Similarly, the average speed of the EB trip will be impacted by the roadway LoS, and consequently the trip time. In this regard, the variation of the average EB trip velocity has been modeled using the estimated quadratic function as shown in Fig. 4.2 (b). Therefore, the trip time can be determined as a function of the traffic flow parameter (v/c) as follows:

$$T^{Trp} = \frac{D^{Trp}}{V^{Avg}(v/c)} \tag{4.8}$$

$$V^{Avg}(v/c) = \frac{D^{Trp}}{T^{Trp,N}} \cdot \Big(-0.51\Big[\frac{v}{c}\Big]^2 + 0.219\frac{v}{c} + 1.14\Big), \tag{4.9}$$

where, D^{Trp} and $T^{Trp,N}$ denote the trip distance and trip nominal time, respectively.

The time between two consecutive bus stops (i.e., section n), T_n^{Stp}, is constrained to its maximum and minimum time limits as expressed in (4.10) and (4.11).

$$T_n^{min} \leq T_n^{Stp} \leq T_n^{max} \quad \forall\, n \in \mathcal{N}_j^{Stp} \tag{4.10}$$

$$T_n^{max} = \frac{D_n^{Stp}}{V^{Avg}(v/c)},\; T_n^{min} = \frac{D_n^{Stp}}{\xi^{Avg} \cdot x^{max}}\; \forall\, n \in \mathcal{N}_j^{Stp}. \tag{4.11}$$

Equation (4.11) defines section n maximum time, T_n^{max}, as a function of section n distance, D_n^{Stp}, over the roadway LoS average velocity. Similarly, section n minimum time, T_n^{min}, is calculated based on the product of the average roadway velocity factor, ξ^{Avg}, and maximum roadway FFS, x^{max}.

The objective function in (4.6) is also subjected to the dwelling time constrained after each section n stated as:

$$\Delta t_{min,n}^{Stp} \leq \Delta t_n^{Stp} \leq \Delta t_{max,n}^{Stp}\; \forall\, n \in \mathcal{N}_j^{Stp}. \tag{4.12}$$

After solving the problem in (4.6)–(4.12), the average speed of each section n can be calculated as follows:

$$V_n^{Avg} = \frac{D_n^{Stp}}{T_n^{Stp}} \; \forall \, n \in \mathcal{N}_j^{Stp}. \tag{4.13}$$

The outputs of the first stage in the proposed model (T_n^{Stp}, Δt_n^{Stp}, and V_n^{Avg}) are inputted to the second stage problem explained in the next subsection to generate the synthetic speed profile.

4.2.2 Stage 2: Generating Synthetic Speed Profile

The second stage aims to generate a speed profile that mimics the actual behaviour of the EBs along the trip route under the study. In this regard, the second stage starts by initializing a random speed profile, x_t^0, at each time step t within the trip time horizon defined as follows:

$$\mathcal{T} = \Big\{1, 1 + \Delta t, 1 + 2\Delta t, \ldots, t, \ldots, n_t - \Delta t, n_t\Big\}, \tag{4.14}$$

where, Δt is the speed profile time step resolution and $n_t = T^{Trp}/\Delta t$ is the number of trip time steps.

Similar to the first stage, the problem in the second stage is formulated as an optimization model. The objective function of the second stage is defined in Equation (4.15). As depicted, in order to preserve the generated speed profile randomness, (4.15) aims to minimize the deviation between the randomly generated speed profile and the estimated values of the speed profile that satisfy the objective function constraints.

$$\text{Minimize:} \quad \sum_{t \in \mathcal{T}} x_t - x_t^0. \tag{4.15}$$

Equation (4.15) is constrained by the maximum and minimum route speed limits as:

$$x^{min} \leq x_t \leq x^{max} \quad \forall\, t \in \mathcal{T}, \tag{4.16}$$

where, the generated speed profile is also subjected to the EB acceleration, a^{Acc} and deceleration, a^{Dec}, limits expressed as:

$$a^{Dec} \leq \frac{x_{t+1} - x_t}{\Delta t} \leq a^{Acc} \quad \forall\, t \in \mathcal{T}. \tag{4.17}$$

Equation (4.15) is also subjected to the average speed constraints at each section n given as:

$$\overline{X}_n = V_n^{Avg} \quad \forall \;\; X_n = \{x_t\} \;\wedge \forall\, n \in \mathcal{N}_j^{Stp} \;\wedge \forall\, t \in \mathcal{T}_n \wedge \forall\, \mathcal{T}_n \subset \mathcal{T}. \tag{4.18}$$

Equation (4.18) implies that the average speed values, $\overline{X}_n$, at each section n is equal to the yielded average speed from the first stage of the proposed model. Where, $\mathcal{T}_n$ is the set of section n time steps, $\mathcal{T}_n = \{t, t + \Delta t, t + 2\Delta t, \ldots, t + T_n^{Stp} - 1\}$. Equation (4.19) below defines the bus stop instant by equating the velocity to zero at time steps that does not belong to the trip sections time steps and belongs to the dwelling time steps, $\mathcal{T}_d = \{t, t + \Delta t, t + 2\Delta t, \ldots, t + \Delta t_n^{Stp} - 1\}$.

$$x_t = 0 \;\; \wedge \;\; \kappa_t = 1 \quad \forall \;\; t \in \mathcal{T} \wedge \forall \;\; t \in \mathcal{T}_d \wedge \forall\, t \notin \mathcal{T}_n \wedge \forall\, n \in \mathcal{N}_j^{Stp}, \tag{4.19}$$

where, κ_t is defined to differentiate whether the EB stops for passenger boarding and/or alighting (i.e., $\kappa_t = 1$), or due to traffic conditions (i.e., $\kappa_t = 0$).

4.3 Electric Bus Energy Consumption

In this section, a detailed consumption model for the EB propulsion, HVAC, and auxiliary loads is presented.

4.3.1 Electric Bus Propulsion Energy Consumption Model

The calculation of the propulsion EBEC model based on Newton's second law of motion is evaluated. The main inputs to the propulsion EBEC model are the bus speed profile, passenger profile, route gradient, and the bus technical specifications such as the drag coefficient, c_d, rolling resistance coefficient, f_r, and frontal surface area, A^F. Here it is worth noting that, the bus speed profile input can be obtained from: (i) the proposed synthetic speed profile model proposed in Section 4.2, in case of it's unavailability, or (ii) the actual real-world speed profile data recorded by the transit network telematics system, if it is available. Equation (4.20) represents the required traction force, F_t^{Trc}, to propel the EB with a specified, x_t velocity [70], [115].

$$F_t^{Trc} = m_t \cdot \dot{x}_t + m_t \cdot g \cdot \sin\left(\phi\left(d_t\right)\right) + m_t \cdot g \cdot f_r \cdot \cos\left(\phi\left(d_t\right)\right) + \frac{1}{2}\rho^{Air} \cdot c_d \cdot A^F \cdot x_t^2, \quad \forall\, t \in \mathcal{T}, \tag{4.20}$$

where, $\phi\left(d_t\right)$ is the route grade as a function of the distance, d_t, covered by the EB at t:

$$d_t = \sum_{t'=1}^{t'=t} x_{t'} \cdot \Delta t \quad \forall\, t \in \mathcal{T}. \tag{4.21}$$

Equation (4.20) yields a positive traction force during acceleration and thus the power is transferred from the battery to the wheel to propel the EB. During deceleration instants, however, the traction force is negative and thus the kinetic power is transferred to recharge

the battery. Accordingly, the EBEC due to traction during a trip could be formulated as:

$$E^{Trc} = \sum_{t \in \mathcal{T}^{+}} \frac{F_t^{Trc} \cdot x_t \cdot \Delta t}{\eta^{Bat}} + \sum_{t \in \mathcal{T}^{-}} F_t^{Trc} \cdot x_t \cdot \Delta t \cdot \eta^{Reg} \quad \forall\, \mathcal{T}^{+} \subset \mathcal{T} \wedge \forall\, \mathcal{T}^{-} \subset \mathcal{T}. \quad (4.22)$$

4.3.2 HVAC Consumption Model for EBs

The HVAC operation of EBs is modeled in this work using the steady state thermal and mass balance equation as expressed in (4.23). Equation (4.23) implies that the change in the stored thermal energy in the EB, $m^{Air} \cdot C_p \cdot (k_t^{EB} - k_{t+1}^{EB})$, is equal to the added HVAC thermal energy, Q_t^{Hvac}, while the conductive and convective thermal energy losses, Q_t^{Los}, the air infiltration energy loss due to the frequent opening of the EB door, Q_t^{Inf}, and the energy loss due to ventilation requirements, Q_t^{Vnt}, are deducted. Also, the developed HVAC model accounts for the passenger heat energy gain, Q_t^{Pas}, as depicted in (4.23).

$$m^{Air} \cdot C_p \cdot \left(k_t^{EB} - k_{t+1}^{EB}\right) = \left(Q_t^{Hvac} - Q_t^{Los} - Q_t^{Inf} - Q_t^{Vnt} + Q_t^{Pas}\right) \cdot \Delta t \quad \forall t \in \mathcal{T}. \quad (4.23)$$

The HVAC system operates in either heating–mode (i.e. $\gamma_t = 1$), cooling–mode (i.e. $\gamma_t = 2$), or off–mode (i.e. $\gamma_t = 0$) according to the EB internal temperature, k_t^{EB}, as:

$$\gamma_t = \begin{cases} 1 \;\; \forall\, (k_t^{EB} < k^{lb}) \;\vee\; (\forall \gamma_{t-1} = 1 \wedge \forall\, k_t^{EB} < k^{S}) \\ 2 \;\; \forall\, (k_t^{EB} > k^{ub}) \;\vee\; (\forall \gamma_{t-1} = 2 \wedge \forall\, k_t^{EB} > k^{S}) \qquad \forall\, t \in \mathcal{T}. \\ 0, \;\; \text{Otherwise} \end{cases} \quad (4.24)$$

As shown in (4.24), the HVAC operates in heating–mode under either of the following two conditions: 1) when the EB internal temperature is below the lower bound of the comfort temperature range (k^{lb}); or 2) when the HVAC is operating in heating–mode, while the EB temperature is still below the desired temperature set point, k^{S}. Similarly,

the HVAC operates in cooling–mode when: 1) the EB internal temperature is above the upper bound of the comfort temperature range (k^{ub}); or 2) the HVAC is operating in cooling–mode, while the EB temperature is still above the desired temperature set point, k^S. Otherwise, the HVAC is turned off. Here it is worth noting that, the HVAC operation is either on or off according to the aforementioned operation mode [116], thus the added thermal energy by the HVAC at each time step is expressed in this work as follows:

$$Q_t^{Hvac} = \begin{cases} Q_R^{Hvac} & \forall\, \gamma_t = 1 \wedge \forall\, t \in \mathcal{T} \\ -Q_R^{Hvac} & \forall\, \gamma_t = 2 \wedge \forall\, t \in \mathcal{T} \\ 0 & \forall\, \gamma_t = 0 \wedge \forall\, t \in \mathcal{T}. \end{cases} \tag{4.25}$$

The conductive and convective thermal losses are given as the difference between the EB' internal and external temperatures, over the EB thermal resistivity as [117]:

$$Q_t^{Los} = \frac{\left(k_t^{EB} - k_t^{Ext}\right)}{R_{eq}} \quad \forall\, t \in \mathcal{T}, \tag{4.26}$$

$$R_{eq} = \frac{L^{Win}}{A^{Win} \cdot u_c^{Win}} + \frac{L^{Chs}}{A^{Chs} \cdot u_c^{Chs}} + \frac{1}{A \cdot h_c^{Ext}} + \frac{1}{A \cdot h_c^{Int}}, \tag{4.27}$$

It is worth noting that the external convective heat transfer coefficient in (4.27) is impacted by the speed of the wind flow over the heated/cooled object and is expressed as follows [118]:

$$h_c^{Ext} = h_c^{Int} - x_t + 10\, x_t^{0.5} \quad \forall\, t \in \mathcal{T}, \tag{4.28}$$

with out loss of generality, in this work the speed of the EB represents the speed of wind flow over the EB with respect to the EB position. The impact of the EB door opening at bus stops is modeled according to the American Society of Heating, Refrigerating and Air-Conditioning Engineers (ASHRAE) modeling for air infiltration rate through door

openings, and is expressed as follows [119]:

$$Q_t^{Inf} = \rho^{Air} \cdot C_p \cdot \left(k_t^{EB} - k_t^{Ext}\right) \cdot V_t^{Inf} \quad \forall\, t \in \mathcal{T}, \tag{4.29}$$

where, V_t^{Inf} is the air infiltration flow rate in (m^3/s) [119]:

$$V_t^{Inf} = \begin{cases} C_A \cdot A^{dor} \cdot \sqrt{R_p} \quad \forall\, \kappa_t = 1 \wedge \ \forall\, t \in \mathcal{T}. \\ 0 \qquad \forall\, \kappa_t = 0 \wedge \ \forall\, t \in \mathcal{T}. \end{cases} \tag{4.30}$$

The designing process of any HVAC system accounts for an adequate ventilation rate to provide comfortable fresh air mixture [120]. In this regard, the ventilation requirements for the EB add burden to the HVAC operation, by allowing a controlled flow rate of fresh air with exterior temperature. The ventilation requirements impact on the HVAC operation is given as follows:

$$Q_t^{Vnt} = \psi^{Vnt} \cdot \dot{V}^{Hvac} \cdot \rho^{Air} \cdot C_p \cdot \left(k_t^{EB} - k_t^{Ext}\right) \quad \forall\, t \in \mathcal{T}. \tag{4.31}$$

The impact of the passenger heat gain on the HVAC operation in (4.23) is modeled as follows [121]:

$$Q_t^{Pas} = h^{Pas} \cdot \beta_t^{Pas} \quad \forall\, t \in \mathcal{T}, \tag{4.32}$$

where, h^{Pas} is the heat gain per passenger (W), which is the product of the passenger metabolic rate (i.e., 1 W/m^2 for rested passenger) and the passenger average skin area (i.e., 1.8 m^2) [122]. While, β_t^{Pas} denotes the passenger profile.

Therefore, the HVAC power consumption can be calculated over the trip duration as:

$$P_t^{Hvac} = \frac{\mid Q_t^{Hvac} \mid}{\eta^{Bat} \cdot \eta^{COP}} \quad \forall\, t \in \mathcal{T}, \tag{4.33}$$

where, η^{COP} indicates the relation between the thermal energy and the consumed electrical energy [116, 123]). In addition to the Q_t^{Hvac} consumption that is responsible for EB heat exchange (Q_t^{Hvac}), the HVAC fan units power consumption for ventilation should be considered as:

$$P_t^{Fan} = v_t^{Fan} \cdot i_t^{Fan} \quad \forall\, t \in \mathcal{T}, \tag{4.34}$$

Therefore, the total HVAC consumption over the trip duration can be calculated as follows:

$$E^{Hvac} = \sum_{t \in \mathcal{T}} (P_t^{Hvac} + P_t^{Fan}) \cdot \Delta t. \tag{4.35}$$

Based on the above discussion, the total EBEC can be expressed as the summation of the traction energy expressed in (4.22), HVAC consumption represented in (4.35) and the consumption of the auxiliary loads (i.e., light, sound and radio system), P_t^{Aux}. Hence, the normalized rate of EBEC in kW h/km could be calculated as:

$$E^{EB} = \frac{E^{Hvac} + E^{Trc} + \sum_{t \in \mathcal{T}} P_t^{Aux} \cdot \Delta t}{D^{Trp}}. \tag{4.36}$$

4.4 Numerical Studies

The proposed EBEC model is coded and simulated in the MATLAB environment. Where, the speed profile resolution, Δt, is defined in this study as one second. The numerical studies is divided into two case studies. First case aims to study the traffic conditions on the EBEC of Route 17 city–bus service in Brampton, Ontario, Canada [124]. While, the second case study investigates different traffic conditions impact of an intercity bus service. In both cases, the HVAC consumption of the generated speed profiles is evaluated

at different temperature conditions. Route 34 of the GO transit is selected for the second case study, where Go transit is an intercity bus service within the Greater Toronto and Hamilton Area (GTHA), Ontario, Canada [125].

Without loss of generality, the EB mass weight (m_t) is considered as the EB gross vehicle weight rating (GVWR). Where, the GVWR defines the maximum total weight of the EB including the passengers and their belongings (i.e., bags, Baggage's, etc.) as specified by the manufacturer [126]. While in the HVAC energy consumption numerical studies, the EB is assumed to have a full passenger capacity, i.e., 38 passengers for the single-decker EB [127], and 81 passengers for the double–decker EB [128]. Here it is worth mentioning that the simulated traffic conditions in this study are neither historical nor forecasted. In fact, this model allows the users such as transit network planners to simulate the speed profile according to their different traffic conditions across the day, by setting the LoS parameter. For this reason, the numerical studies in this work are evaluated at different LoS values to cross compare the impact of traffic condition on the EBEC.

The proposed optimization model is identified as a linear optimization problem. Different methods can be used to solve the formulated optimization model. It is solved, in this work, using Interior Point linear programming algorithm. This method is coded as a built-in function in the Matlab optimization toolbox. Thereby, the optimization model is coded and solved in the MATLAB environment. The optimization problem is executed in a PC with the following specifications: Core i7-6700, 3.4 GHz CPU, 16 GB RAM, and 64 bits system. The convergence tolerance and the maximum number of iterations are set to 10^{-6} and 250, respectively. The optimization problem solution is converged in an average of 32 iterations for all scenarios.

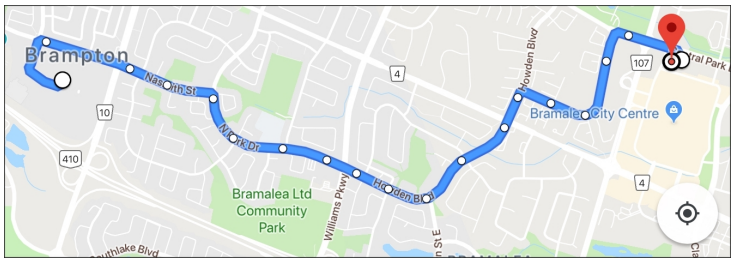

Figure 4.3: The studied Brampton transit Route 17 at the southbound direction between Trinity Common Terminal toward Bramalea Terminal.

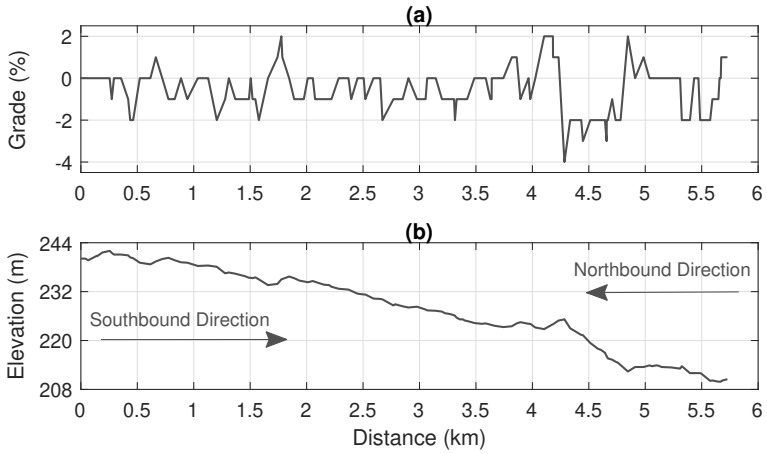

Figure 4.4: Brampton Route 17 northbound: (a) grade, and (b) elevation.

4.4.1 First Case Study: Traffic Conditions Impact on the Energy Consumption of Single–Decker EB

This section aims to generate a set of speed profiles for different traffic conditions for the first case study. This is to analyze the impacts of traffic conditions on the energy consumption due to traction, regenerative, auxiliary, and HVAC system. As shown in Fig. 4.3, Route 17 in Brampton, Ontario, Canada is used for the first case studies. Route 17 has a round bus service trip in southbound and northbound directions with a total distance of 5.75 km for each direction. The studied route delivers the bus transportation service in an average of 16 minutes in both of the trip directions [124]. Fig. 4.4 shows the grade and elevation of the studied route. In which, each of southbound and northbound

Table 4.2: Route and Speed Profile Modeling and Simulation Parameters

$D^{Trp} = 5.75$ km	$T^{Trp,N} = 16$ min	N_s =18
$x^{max} = 50$ km/h	$x^{min} = 0$ km/h	$\xi^{Avg} = 75\%$
$\Delta t^{Stp}_{min,n} = 15$ s	$\Delta t^{Stp}_{max,n} = 30$ s	$\rho^{Air} = 1.2258$ kg/m^3
$\Delta t = 1$ s	$C_p = 1.005$ kJ/kg.K	$g = 9.8$ m/s^2

Table 4.3: EB Modeling and Simulation Parameters

$m_t = 19700$ kg	$\eta^{Bat} = 95\%$	$\eta^{Reg} = 50\%$
$a^{Acc} = -a^{Dec} = 7.2$ km/h^2	$f_r = 0.015$	$c_d = 0.65$
$A^F = 9.095$ m^2	$m^{Air} = 111$ kg	$Q^{Hvac}_R = 30$ kW
$k^S = 21$°C	$k^{lb} = 18.9$°C	$k^{ub} = 23.1$°C
$u^{Win}_c = 0.0566$ W K/m	$A^{Win} = 31.8$ m^2	$L^{Win} = 20$ mm
$u^{Chs}_c = 0.0738$ W K/m	$A^{Chs} = 138.2$ m^2	$L^{Chs} = 50$ mm
$h^{Int}_c = 10.45$ W/m^{2}K	$A = 170$ m^2	$A^{dor} = 1.85$ m^2
$C_A = 0.1$ (m^3/s)/(m^2 Pa$^{0.5}$)	$R_p = 0.3$ Pa	$\psi^{Vnt} = 20\%$
$\dot{V}^{Hvac} = 1.13$ m^3/s	$h^{Pas} = 1.8$ W	$\eta^{COP} = 2$
$v^{Fan}_t = 27$ V	$i^{Fan}_t = 106$ A	$P^{Aux}_t = 9$ kW

trip direction has eighteen specified bus stops. In this study, each bus stop has a stop probability of 50% (i.e., $\varrho_s = 50\%$), except three bus stops, which are a must stop locations at major intersections and thus they have stop probabilities of 100%. The studied route and generated speed profiles modeling parameters are given in Table 4.2 [124]. Table 4.3 presents the EB modelling and simulation parameters, where a 40 ft single-deck city bus is considered in this study [116, 118, 119, 120, 122, 129].

In order to evaluate the impact of the traffic conditions on the EBEC due to propulsion, regenerative, auxiliary, and HVAC, a set of 100 synthetic speed profiles is generated for different LoS (i.e., (v/c) values). Where, the generated speed profiles follow the number of bus stops probability distribution for the studied route number of bus stops given in Fig. 4.5. A sample of three generated speed profiles for free, light, and congested traffic

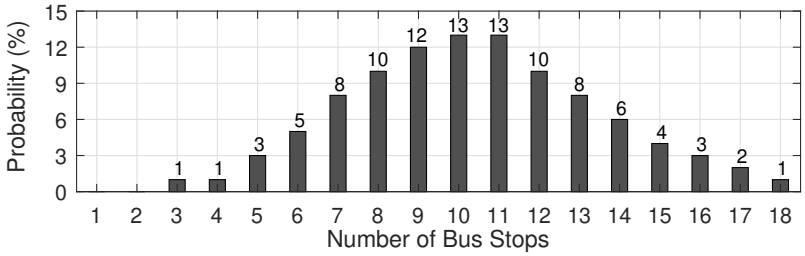

Figure 4.5: Number of bus stops probability for Brampton Route 17.

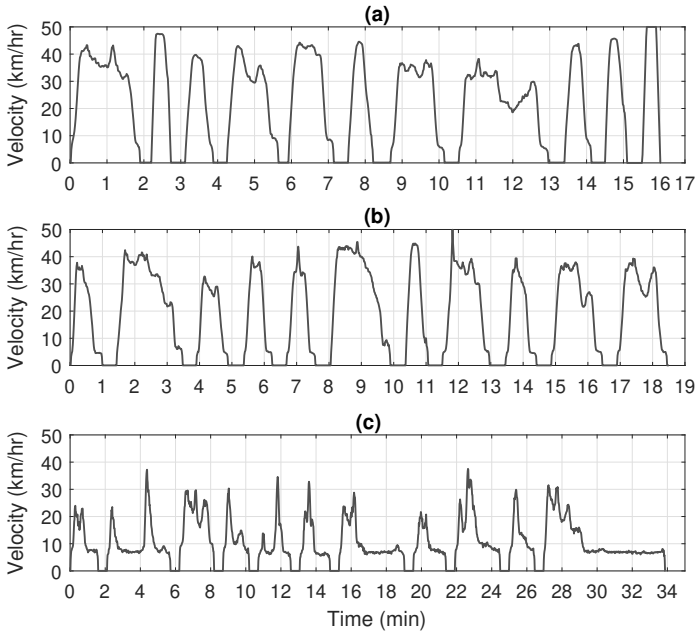

Figure 4.6: Samples from the southbound generated speed profiles: (a) Free traffic condition, (b) Light traffic condition, and (c) congested traffic condition.

conditions that corresponds to 0.35, 0.55, and 0.95 LoS, respectively are shown in Fig. 4.6. As depicted, free and light traffic conditions have higher speed values as shown in Fig. 4.6 (a) and (b), compared to congested traffic condition in Fig. 4.6 (c). It is also shown that the impact of the traffic condition is reflected on the trip duration. Where, the trip duration for the free, light, and congested traffic condition are 16 minutes, 18.5 minutes, and 34 minutes, respectively, as shown in the figure. As such, the average speed of the free, light and congested traffic conditions are 21.7 km/h, 18.77 km/h, and 10.3 km/h, respectively. Table 4.4 presents a breakdown of the EBEC associated with the speed profiles depicted in

Table 4.4: Energy Consumption Breakdown for the Sampled Speed Profiles in Figure 4.6 using Single–Deck EB

Consumption Breakdown (kW h/km)	Free Traffic (v/c =0.35)	Light Traffic (v/c =0.55)	Congested Traffic (v/c =0.95)
Traction Southbound	1.46	1.344	1.1
Traction Northbound	1.854	1.726	1.53
Regenerative Southbound	−0.331	−0.3	−0.22
Regeneration Northbound	−0.24	−0.2	−0.149
Auxiliary	0.417	0.483	0.884
HVAC at 5°C	0.289	0.332	0.56
Total Southbound	1.835	1.859	2.324
Total Northbound	2.32	2.341	2.825

Fig. 4.6. Where, the HVAC consumption is evaluated at exterior temperature of 5°C. As shown in Table 4.4, trips in the northbound direction yield a higher average of EBEC due to traction of 0.4 kW h/km higher than the southbound direction, as a result of the uphill elevation during the northbound trip as shown in Fig. 4.4 (b). For the same reason, the results show that the regenerative energy into the EB battery is lower in the northbound trip direction compared to the southbound direction. The results also show that both the traction and regenerative energies decreases with the increase of the LoS, due to the lower velocity values at high LoS conditions. However, energy consumption due to auxiliary loads and HVAC increases with the increase of the LoS, where they are impacted by the trip duration, which relies on the LoS. It is, thus, noteworthy that although the traction energy decreases at higher LoS conditions, the total EBEC increases due to the impact of LoS on the regenerative energy, auxiliary loads, and HVAC.

Figs. 4.7, 4.8, and 4.9 show the EBEC histogram for the generated speed profiles at free, light, and congested traffic conditions, respectively. Figs. 4.7 (a), 4.8 (a), and 4.9 (a) present the traction EBEC histograms for the aforementioned traffic conditions, respectively. As depicted in the figures, traction EBEC varies between 1-2 kW h/km in

free traffic condition, 1-1.8 kW h/km in light traffic conditions, and 0.8-1.8 kW h/km in congested traffic conditions. Where, lower traction EBEC's are noted at congested traffic conditions. While, Figs. 4.7 (b), 4.8 (b), and 4.9 (b) show the regenerative energy histograms for the three traffic conditions, respectively. Although, the mean of the regenerative energy in the shown traffic conditions is almost the same around -0.317 kW h/km, chances of higher regenerative energy occur at free and light traffic conditions. Figs. 4.7 (c), 4.8 (c), and 4.9 (c) show the auxiliary loads consumption that have a fixed value, given that all the generated speed profiles have the same time duration at a given traffic condition. While, Figs. 4.7 (d), 4.8 (d), and 4.9 (d) present the histograms for the HVAC energy consumption for the aforementioned traffic conditions, respectively. As shown in the figures, the energy consumption due to HVAC has a slight distribution variation around the mean consumption value. This variation occurs due to the changes of the actual stops of the bus during trips, as per the probability described in Fig. 4.5, and thus different rate of air infiltration occurs due to the bus door opening.

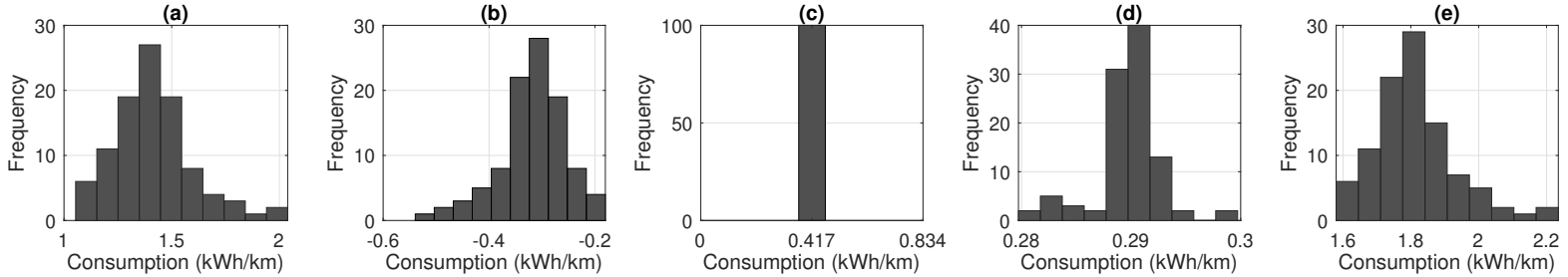

Figure 4.7: Southbound trip histogram for the free traffic conditions: (a) Traction consumption, (b) Regenerative energy, (c) Auxiliary consumption, (d) HVAC consumption, and (e) Total consumption.

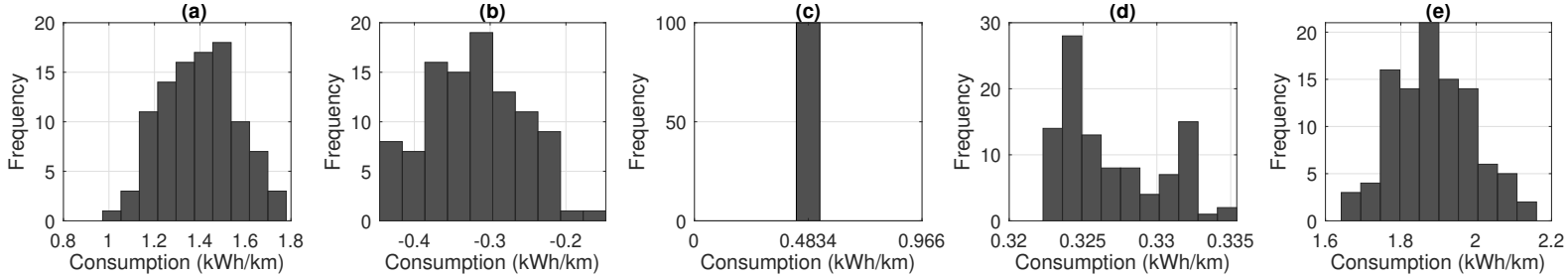

Figure 4.8: Southbound trip histogram for the light traffic conditions: (a) Traction consumption, (b) Regenerative energy, (c) Auxiliary consumption, (d) HVAC consumption, and (e) Total consumption.

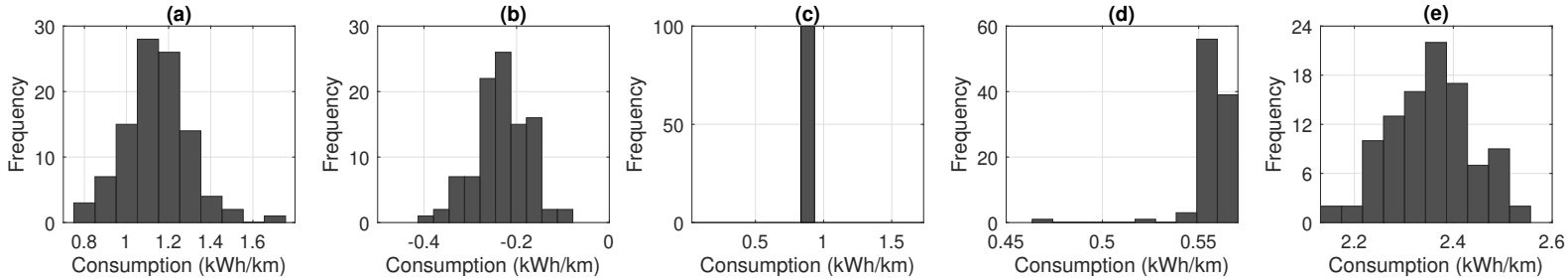

Figure 4.9: Southbound trip histogram for the congested traffic conditions: (a) Traction consumption, (b) Regenerative energy, (c) Auxiliary consumption, (d) HVAC consumption, and (e) Total consumption.

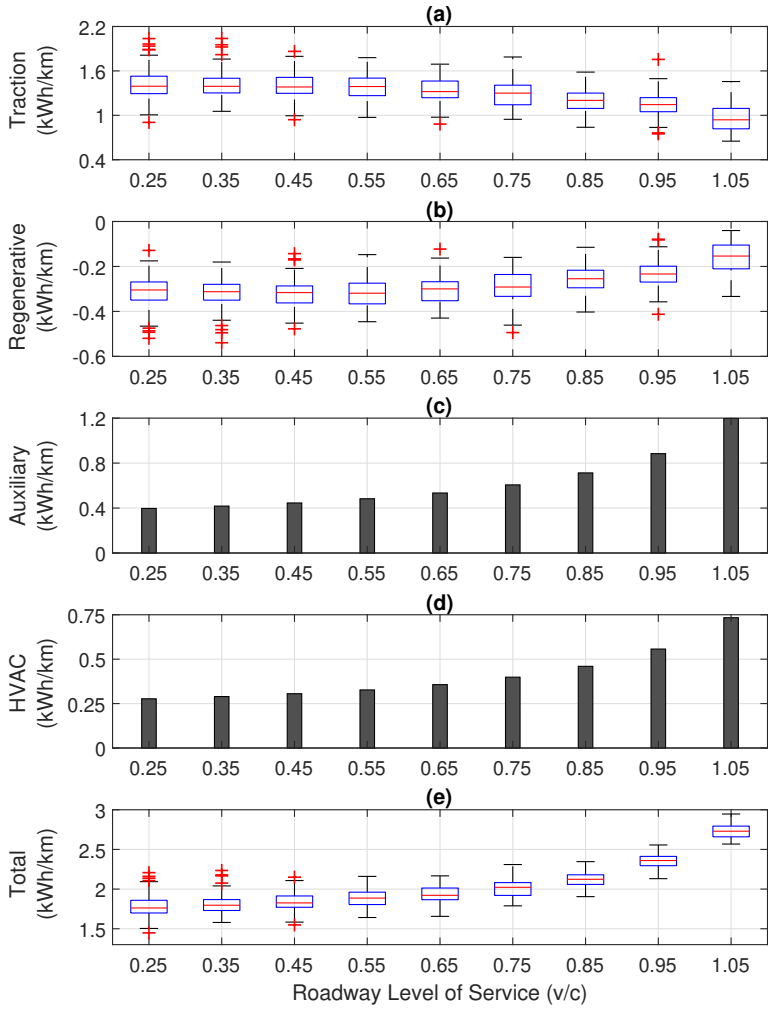

Figure 4.10: Energy consumption at different LoS conditions: (a) Traction, (b) Regenerative, (c) Auxiliary, (d) HVAC, and (e) Total consumption.

Fig. 4.10 depicts the distribution of the EBEC at different LoS conditions at the southbound trips direction. The central mark in Figs. 4.10 (a), (b), and (e) depicts the median of the energy consumption, while the box top and bottom edges depicts the 75^{th} and 25^{th} percentiles of the EBEC data, respectively. While, the bar chart in Fig. 4.10 (c) and (d) represent the auxiliary loads and the HVAC average energy consumption. As shown in Fig. 4.10, the trend of the EBEC components is consistent versus the roadway LoS. Where, traction energy consumption and regenerative energy decrease with the increase of LoS.

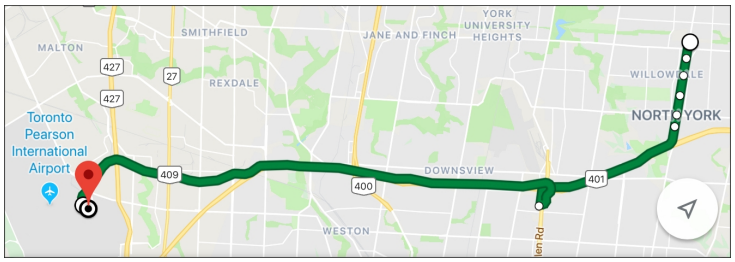

Figure 4.11: Route 34 of the GO transit at the westbound direction from Finch Bus Terminal towards Pearson Airport Terminal.

While, the energy consumption due to the auxiliary loads and HVAC system increases at higher roadway LoS. As a result, the total EB increases at higher roadway LoS as shown in Fig. 4.10 (e).

4.4.2 Second Case Study: Traffic Conditions Impact on the Energy Consumption of Double–Decker EB

There is a variation in transit network characteristics, besides different EB categories in the market. In such a case, studying the EBEC under different conditions is worth investigating. For this reason, this section aims to generate a set of 100 synthetic speed profiles for an intercity bus service. Fig. 4.11 shows the map of the studied GO transit route, between Finch bus terminal and Pearson Airport terminal in Toronto, Ontario, Canada [125]. Unlike a transit city bus service, intercity bus service has fewer bus stops, and travels long distances with high speed ranges through highway routes [66]. Additionally, the Go transit intercity bus service utilizes a double-decker buses that have higher GVWR, which is investigated in this case study. Table 4.5 presents the updated parameters to model the double-decker EB compared to Table 4.3. Route 34 has a round bus service in an eastbound and a westbound trip directions with an average time of 30 minutes for each trip direction. The trip distances for the eastbound and westbound trip directions are 24.4 km and 25.3 km, respectively. Fig. 4.12 shows the grade and elevation of the

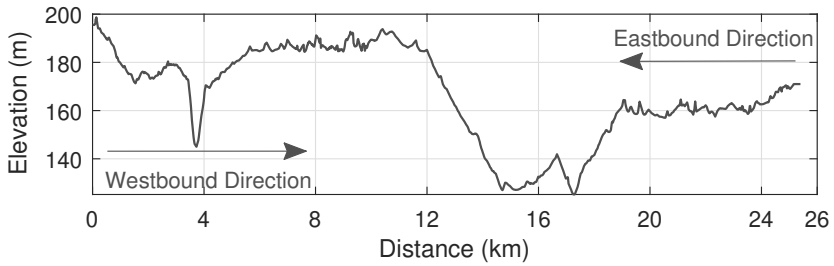

Figure 4.12: Elevation characteristics of the studied GO transit Route 34.

Table 4.5: Double–Decker EB Modeling and Simulation Updated Parameters Compared with Table 4.3

$m_t = 26500$ kg	$m^{Air} = 131.5$ kg
$A^{Win} = 76.94$ m^2	$A^{Chs} = 115.4$ m^2
$A^{dor} = 2.5$ m^2	$A^{F} = 10.4$ m^2
$A = 192.35$ m^2	$\dot{V}^{Hvac} = 2$ m^3/s
$Q_R^{Hvac} = 45$ kW	$P_t^{Aux} = 15$ kW

studied route with a minimum and maximum dwelling time at each bus stop of 60 to 180 seconds. In which, each of eastbound and westbound trip direction has eleven designated bus stops. Each bus stop has a stop probability of 50%, except three bus stops, which are a must stop locations at major terminals and thus they have stop probabilities of 100% [125]. To that end, a set of 100 synthetic speed profiles is generated for different settings of LoS. Where, the generated set of speed profiles follow the probability distribution given in Fig. 4.13. The generated set of speed profiles are then utilized to investigate the impact of the traffic conditions on the EBEC components: propulsion, regenerative, auxiliary, and HVAC. Three generated speed profiles for free, light, and congested traffic conditions are presented in Fig. 4.14. Similar to the first case study, the speed values decrease and the trip duration increases at higher LoS. It is found that, the trip duration for the free, light, and congested traffic conditions are 30 minutes, 35 minutes, and 64 minutes, respectively, as shown in the figure. Where, the average speed of the free, light and congested traffic conditions are 48.66 km/h, 42.23 km/h, and 23.14 km/h, respectively.

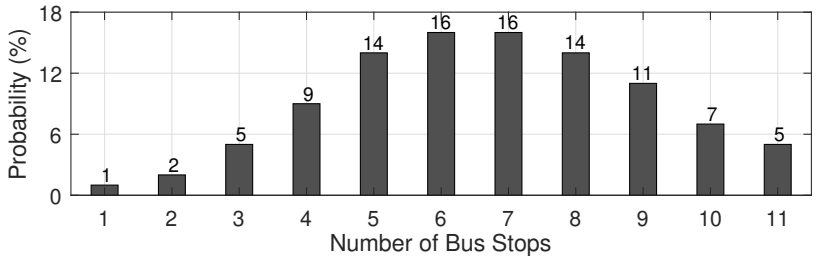

Figure 4.13: Probability of the number of bus stops for the studied GO transit route.

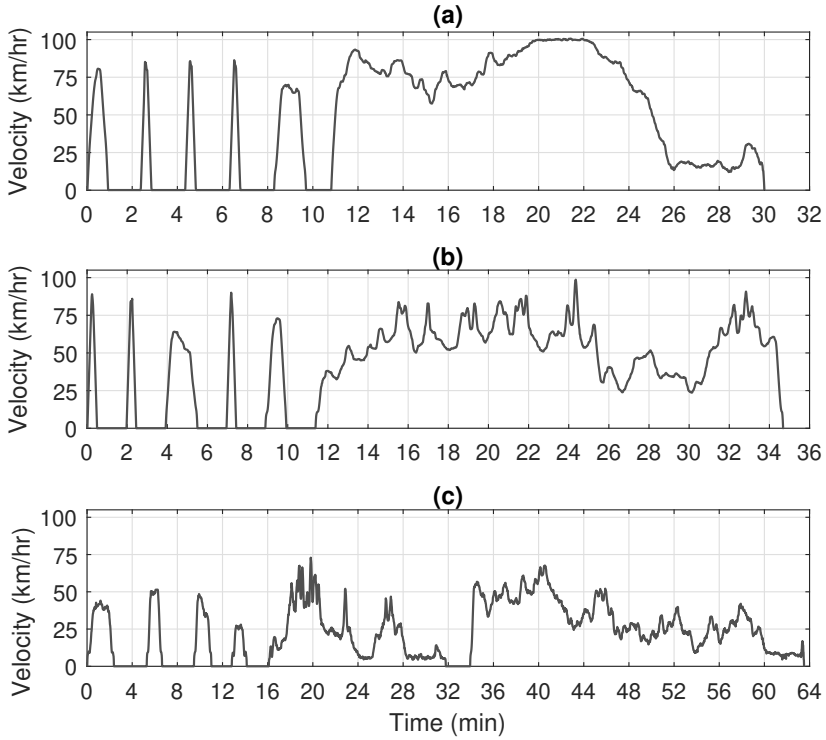

Figure 4.14: Samples from the westbound generated speed profiles: (a) Free traffic condition, (b) Light traffic condition, and (c) congested traffic condition.

The breakdown of the EBEC components for the speed profiles shown in Fig. 4.14 are presented in Table 4.6; where, the HVAC consumption is evaluated at exterior temperature of 5°C. Unlike the first case study, it is found that differences between eastbound and westbound traction and regenerative energy consumption are not consistent (i.e., eastbound might be higher, lower, or equal than/to the westbound energy consumption). This inconsistency is due to Route 34 topography shown in Fig. 4.12, where in both directions there

Table 4.6: Energy Consumption Breakdown for the Sampled Speed Profiles in Figure 4.14 using Double–Decker EB

Consumption Breakdown (kW h/km)	Free Traffic (v/c =0.35)	Light Traffic (v/c =0.55)	Congested Traffic (v/c =0.95)
Traction Eastbound	2.26	2.07	1.75
Traction Westbound	2.15	2.22	1.74
Regenerative Eastbound	−0.31	−0.274	−0.208
Regeneration Westbound	−0.25	−0.4	−0.267
Auxiliary	0.3	0.343	0.63
HVAC at 5°C	0.154	0.177	0.313
Total Eastbound	2.396	2.32	2.482
Total Westbound	2.351	2.344	2.414

are uphills and downhills elevation. Hence, neither of the trip directions is guaranteed to have higher EBEC than the other due to the route elevation. In contrast, the first case study always has an uphill elevation in the northbound, and vice versa for the southbound trip direction. For instance, as shown in Table 4.6, the traction consumption of the eastbound trip compared to the westbound trip is higher in free traffic condition, lower in light traffic condition, and almost equal in congested traffic condition. However, the traction and regenerative energies constantly decrease with the increase of the LoS. In some cases, it is observed that the traction energy consumption and regenerative energy for a given LoS are higher than their corresponding lower LoS. For example, Table 4.6 shows that the westbound traction and regeneration energy in light traffic condition of 2.22 kW h/km and -0.4 kW h/km, respectively, are higher than those in free traffic condition i.e., 2.15 kW h/km and -0.25 kW h/km, respectively. This result is due to the smooth speed profile shown in Fig. 4.14 (a) for free traffic condition. Where, lower instances of acceleration and deceleration results in lower traction and regenerative energy values. In contrast, the light traffic condition speed profile depicted in Fig. 4.14 (b) has many instances of acceleration and deceleration according to the traffic condition. As a result, the speed profile in Fig.

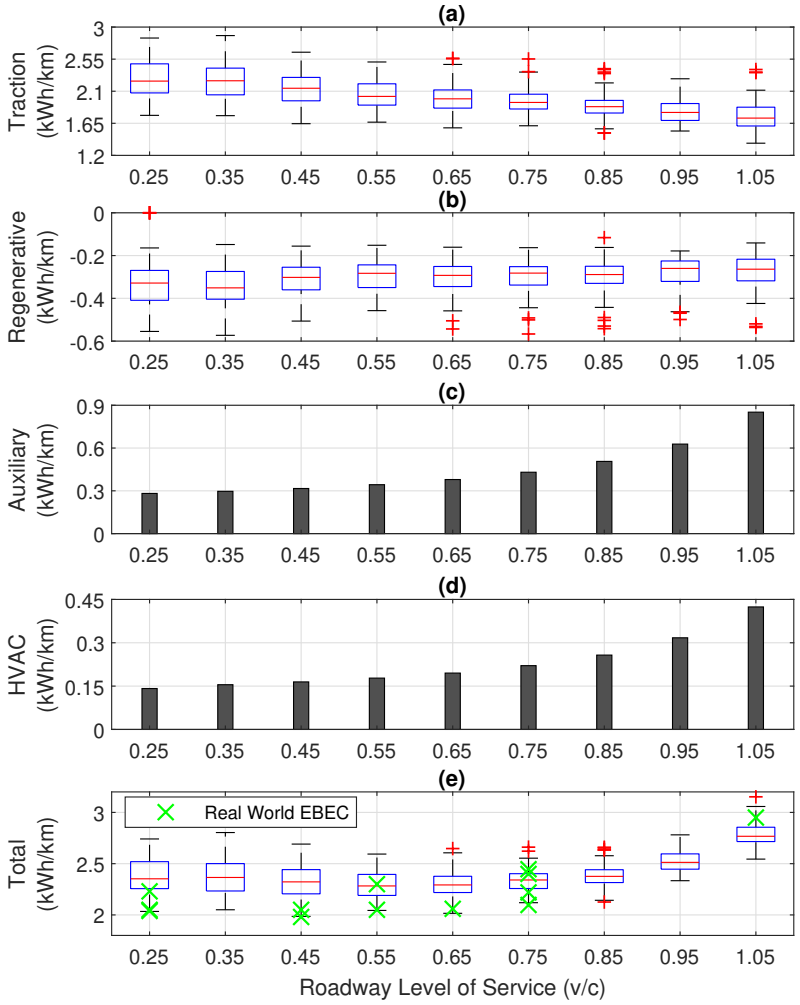

Figure 4.15: Energy consumption at different LoS conditions: (a) Traction, (b) Regenerative, (c) Auxiliary, (d) HVAC, and (e) Total consumption vs. real world speed profiles EBEC.

4.14 (b) has higher traction and regeneration energy compared to Fig. 4.14 (a).

Fig. 4.15 presents the distribution of the EBEC at different settings of the LoS at the westbound trips direction. As shown in Fig. 4.15, the traction and regenerative energies tend to decrease with the increase of LoS. While, auxiliary loads and HVAC system energy consumptions increase at higher roadway LoS. As shown in Fig. 4.15 (e), the total EBEC in the second case study slightly decreases from LoS of 0.25 to 0.65, then the total EBEC

increases once again until it reaches its higher level at LoS of 1.05. Whereas, the decrease rate in the traction energy consumption from LoS of 0.25 to 0.65 is higher than the increase in the regenerative energy.

Fig. 4.15 (e) also presents an EBEC comparison between the distribution of the proposed synthetic speed profiles and real–world speed profiles at different LoS conditions. In particular, thirteen real–world speed profiles for the second case study are utilized to validate the proposed model. The thirteen speed profiles are categorized based on their traffic LoS and then their energy consumption have been calculated using the same EB, route, and weather temperature specifications. As shown in the figure, the energy consumption of the real–world speed profiles are within the calculated range for the synthetic speed profiles. Where, the minimum and maximum absolute difference between the EBEC of the real–world speed profiles and the median of the synthetic speed profiles distribution are 0.75% and 13.9%, respectively. While the average absolute difference between the real–world speed profiles EBEC and their corresponding median is 8.5%.

4.4.3 Impact of Weather on the Energy Consumption of HVAC

In this section, the HVAC operation and consumption of the generated speed profiles will be evaluated. The operation of the HVAC system at 5°C for the speed profile shown in Fig. 4.6 (b) is depicted in Fig. 4.16. The interior EB temperature and the HVAC operation in the heating mode are shown in Fig. 4.16 (a) and (b), respectively. As shown in Fig. 4.16, at the beginning of the trip, the HVAC operation status is on to raise the EB temperature from the initial temperature of 5°C to the comfortable temperature range (18.9 - 23.1 °C). Once the EB interior temperature reaches the comfortable temperature range, the HVAC will operate only once the temperature falls below this range. Fig. 4.16 (c) shows the ventilation burden on the HVAC operation, where 20% of the HVAC airflow should be fresh air that is characterized by the EB external temperature [120]. Therefore, a portion

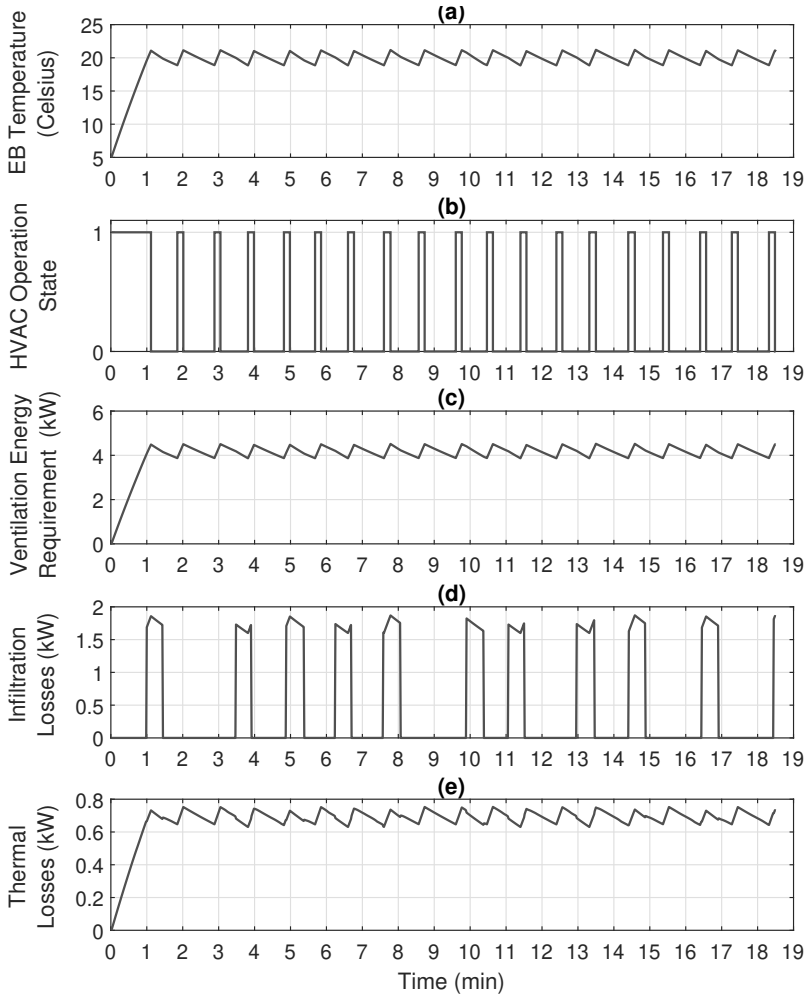

Figure 4.16: EB: (a) Interior temperature, (b) HVAC operation state, (c) HVAC ventilation energy, (d) HVAC infiltration losses, and (e) HVAC thermal losses.

from the HVAC heating capacity will be responsible for heating the fresh air, instead of heating the circulated air from inside the EB. Fig. 4.16 (d) depicts the infiltration losses due to the EB door opening at bus stops, which can be correlated with the temperature drop in Fig. 4.16 (a). Fig. 4.16 (e) presents the summed EB conduction and convection thermal losses, which are functions of the exterior and interior temperatures.

In order to better understand the consumption behaviour at different weather conditions, the HVAC energy consumption for the two studied cases in Section 4.4.1 and 4.4.2

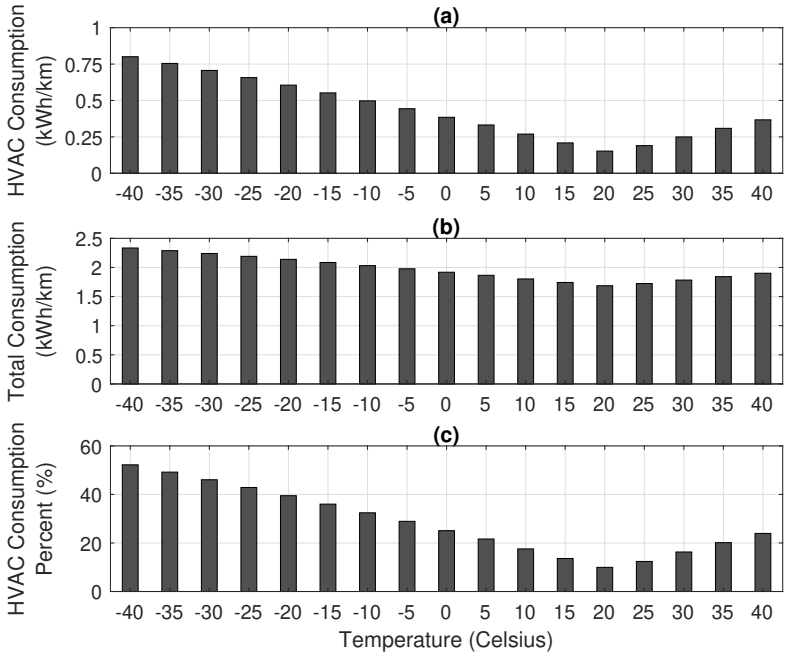

Figure 4.17: First case study EBEC at different weather temperature: (a) HVAC consumption, (b) Total consumption, and (c) HVAC consumption percentage.

are assessed at various temperature ranges from −40°C to 40°C. In this regard, Fig. 4.17 (a) presents the HVAC energy consumption for the first case study speed profile shown in Fig. 4.6 (b) at different temperature conditions. Fig. 4.17 (b) shows the total energy consumption at different temperature ranges. While, Fig. 4.17 (c) shows the contribution percent of the HVAC energy consumption to the total EBEC. It is worth noting that the HVAC consumption is maximum at 0.8 kW h/km during extreme cold temperature of -40°C, which raises the EBEC by 52.2%. As observed, the HVAC consumption decreases gradually as the temperature increase until it reaches the minimum consumption point of 0.152 kW h/km at 20°C. Although, the temperature condition at 20°C is within the passengers comfortable temperature range, the HVAC ventilation's fans might operate in case of closed EB windows. At this condition the HVAC fans operation increases the EBEC by 9.95%. The HVAC consumption, then, increases gradually with the increase of the temperature toward 40°C. In which, the HVAC consumes 0.37 kW h/km at 40°C, which increases the EBEC by 24%.

Similar analysis is carried out to evaluate the impact of HVAC consumption at temperature ranges from -40°C to 40°C for the second case study. The results demonstrate a similar behaviour to Fig. 4.17. The HVAC consumption varies from 0.51 kW h/km at -40°C, then decrease to a minimum consumption point of 0.067 kW h/km at 20°C, then increases once again to 0.21 kW h/km at 40°C. Where, the HVAC consumption contributes to an additional 23.41% at -40°C, only 3.1% at 20°C, and 9.65% at 40°C. Here it is worth mentioning that the impact of the HVAC consumption in the second case study in terms of kW h/km and contribution percent are lower than those found in the first case study because of the longer covered distance i.e., 24.4 – 25.3 km compared to 5.75 km in the first case study.

4.5 Discussion and Summary

A novel probabilistic model for generating large numbers of varying speed profiles of a specific bus route was developed in this work. The model does not require a high time-resolution speed profile data as it uses the basic information of the electric bus trip (i.e., trip time, distance, and stop locations). The proposed model has been utilized to analyze the electric bus energy consumption variations due to route characteristics, traffic conditions, weather conditions, and the operation of HVAC system. The conducted energy consumption analysis considers the impact of roadway level of service on the traffic average speed in order to simulate different real–world traffic conditions. Several case studies have been presented to quantitatively assess the parameters that impact the energy consumption of EBs at different real-world traffic and weather conditions. The case studies indicate that different trip directions (i.e., eastbound versus westbound and southbound versus northbound) might have different EBEC due to the route topography. Different weather temperatures also have a substantial impact on the EBEC that can increase the energy consumption by more than 50%. In addition, the numerical studies reveal that traffic con-

ditions impact the EBEC components. In particular, the EB traction energy consumption and regenerative energy decrease at higher traffic conditions, due to lower speed values at high traffic conditions. While, the auxiliary loads and HVAC energy consumption increase at higher traffic conditions, because of longer trip duration at higher traffic conditions. In overall, the total energy consumption rate increases at higher traffic conditions, due to the overall impact of traction, regenerative, auxiliary loads, and HVAC energy consumptions. Furthermore, the type of the EB (i.e., single–decker versus double–decker) and the type of the transit service (city versus intercity bus service) affect the EBEC. Double-decker EB has higher traction energy than single–decker EB due to higher GVWR; in addition intercity bus service has higher traction energy than city bus service due to higher speed ranges. The presented energy consumption modeling and analysis is immensely useful to conduct accurate feasibility and operation studies related to the adoption of EBs in transit systems. As such, the developed probabilistic model for the speed profiles is superior in capturing the true EBEC without the need for high resolution data.

Chapter 5
Integrated Utility–Transit Model for Optimal Configuration of BEB Fleets

5.1 Introduction

In this chapter, a new mathematical model is developed for electrified bus fleets. The proposed mathematical formulation is developed for the integrated utility–transit model, which aims at optimizing the BEB system configuration: these being battery capacity; chargers' rated size; and number of chargers. The formulated optimization model minimizes the capital expenditure, while considering the operational constraints imposed by both power and transit networks. Detailed BEB energy consumption model is also incorporated in the optimal configuration model to enhance its accuracy.

5.2 Problem Hypothesis

PBT has traditionally been designed to serve the public in relatively dense urban areas, where travel patterns and volumes enable service along fixed routes to follow predetermined

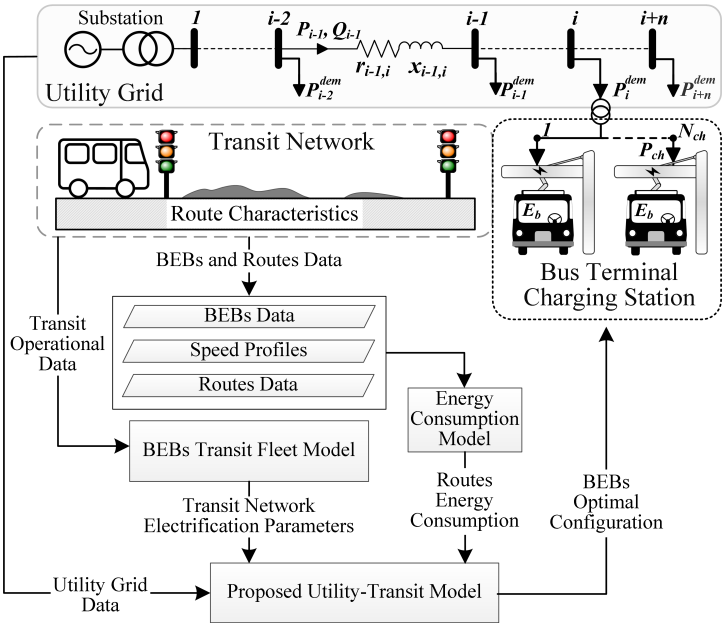

Figure 5.1: Framework for the proposed utility–transit optimization model.

schedules. Transit network scheduling is a process yielding a timetable that includes departure times from all the stops served by each route in the network. Each route–based timetable consists of the departure times from the initial terminal, the expected departure times from each bus–stop on the route, and expected arrival times at the final depot. The transit network timetabling is dependent on many factors; among which, the most prominent are: transit route networks, passenger demand, transfer coordination, and fleet size [130]. Hence, a seamless transition toward electric transit systems necessitates preserving the operation timetable [28, 30].

Fig. 5.1 shows a schematic overview for the proposed utility–transit electrification model. As shown in the figure, the transit network operational schedule is inputted to the BEBs transit fleet model. This would lead to the transit network electrification parameters that preserve the transit network operational requirements. Also, transit fleet data and network topology (i.e., BEBs weight, efficiencies, speed profiles, and routes distance and topography) is inputted to the energy consumption model to calculate the BEBs energy

consumption in kWh/km. To that end, the output of the BEBs transit fleet model and the energy consumption model, besides the utility grid data and operational requirements are inputted to the developed utility–transit model. The utility–transit model aims to determine the optimal configuration for an electric transit city bus fleet: BEBs battery capacity and the dimensions of the charging stations, e.g., size and number of chargers.

5.3 Modeling of BEBS Fleet and Energy Consumption

In this section, the mathematical modeling of the BEBs transit fleet and the BEBs energy consumption model are presented. Table 5.1 presents the definition of the proposed model indices, sets, parameters, and variables.

Table 5.1: Chapter 5 Nomenclature

A. Indices		*B. Sets*	
b, r	Indices for transit network buses / routes.	$\mathbb{B}$	Set of transit network buses.
a, j	Indices for bus's assignments / trips.	$\mathbb{R}$	Set of transit network routes.
t, d	Indices for time steps.	$\mathbb{A}$	Set of transit network assignments.
i	Indices for nodes / branches in PDS.	$\mathbb{J}_a$	Set of trips within assignment a.
		$\mathbb{T}_s$	Set of optimization time steps.
		$\mathbb{I}$	Set of nodes / branches in PDS.
		$\mathbb{T}_{b,j,a}$	Set of BEB b charging opportunity time steps after trip j within assignment a.

Table 5.1: Chapter 5 Nomenclature ... continued

C. Parameters

N_b Number of transit network buses.

N_r Number of transit network routes.

N_a Number of transit network assignments.

N_a^{trp} Assignment a number of trips.

N_t Number of optimization time steps.

$N_{j,a}^{opp}$ Number of charging opportunity time steps after trip j within assignment a.

l_r Route r length (km).

S_a Defined schedule for assignment a.

T_a^{str} Start time for assignment a (h).

T_a^{end} End time for assignment a (h).

t_a^{trp} Trip time for assignment a (mins).

t_a^{cyc} Cycle time for assignment a (mins).

t_a^{rec} Recovery time after each trip within assignment a trips (mins).

t_a^{nxt} Recovery time after completing assignment a trips (mins).

t^{pio} Time for plug in and out the charger (mins).

$t_{j,a}^{ch,max}$ Maximum charging time after trip j within assignment a (mins).

$k_{j,a}^{arr}$ Trip j arrival time step within assignment a.

T^{opt} Optimization problem time horizon (h).

Δt^{stp} Optimization time step interval (mins).

$F_{t,j,a}^{trc}$ BEB traction force at time t, trip j, and assignment a (N).

$E_{j,a}^{trc}$ BEB average traction energy at time t, trip j, and assignment a (kWh).

$E_{j,a}^{BtW}$ Battery–to–wheel traction energy for trip j within assignment a (kWh).

$E_{j,a}^{cons}$ BEB energy consumption for trip j within assignment a (kWh/km).

$P_{b,t}^{aux}$ BEB b auxiliary loads at time t (kW).

$m_{t,j,a}$ BEB mass at time t, trip j, and assignment a (kg).

$\phi_{t,j,a}$ Route gradient angle at time t, trip j, and assignment a (Rad).

$v_{t,j,a}$ BEB velocity at time t, trip j, and assignment a (m/s).

$\dot{v}_{t,j,a}$ BEB acceleration at time t, trip j, and assignment a (m/s^2).

g, ρ Gravitational force (m/s^2), and air density (kg/m^3).

A, c_t BEB cross section area (m^2) and drag coefficient, respectively.

f BEB rolling resistance coefficient.

η^{BtW} Battery-to-wheel efficiency (%).

η^{ch} Charger efficiency (%).

C_b^{exp} Battery expenditure cost ($/kWh).

C_{ch}^{exp} Charger expenditure cost ($/kW).

C_{ch}^{inst} Charger installation cost ($/charger).

SOC_b^{min} BEB b minimum SOC (%).

SOC_b^{max} BEB b maximum SOC (%).

E_b^{min} BEB b minimum battery capacity (kWh).

E_b^{max} BEB b maximum battery capacity (kWh).

P_{ch}^{min} Minimum charger size limit (kW).

P_{ch}^{max} Maximum charger size limit (kW).

Table 5.1: Chapter 5 Nomenclature ... continued

N_{ch}^{min}	Minimum charger's number limit.
N_{ch}^{max}	Maximum charger's number limit.
$P_{i,t}^{dem}$	Active power demand at node i and time t (MW).
$Q_{i,t}^{dem}$	Reactive power demand at node i and time t (MVAr).
$Y_{ii'}$	Admittance magnitude between node i and i' (pu).
$\theta_{ii'}$	Admittance angle between node i and i' (Rad).
V_i^{min}	Bus i minimum voltage limit (pu).
V_i^{max}	Bus i maximum voltage limit (pu).
P_i^{max}	Branch i maximum rating capacity (MW).
D. Variables	
$\mathcal{E}_b$	BEB b battery size (kWh).
$\mathcal{P}_{ch}$	Charger Size (kW).
$\mathcal{N}_{ch}$	Number of chargers.
$\mathcal{SOC}_{b,j,a}^{dep}$	BEB b departure SOC for trip j within assignment a (%).
$\mathcal{SOC}_{b,j,a}^{arr}$	BEB b arrival SOC after trip j within assignment a (%).
$\Delta\mathcal{SOC}_{b,j,a}$	BEB b charged SOC after trip j within assignment a (%).
$\mathcal{T}_{b,j,a}^{ch}$	BEB b charging time after trip j within assignment a (mins).
$x_{d=t}^{b}$	BEB b charging status binary variable at time t.
X^b	BEB b charging binary vector.
$N_{X_{j,a}}$	Number of available charging time steps after trip j within assignment a.
$P_{i,t}^{gen}$	Active power generation at node i and time t (MW).
$Q_{i,t}^{gen}$	Reactive power generation at node i and time t (MVAr).
$V_{i,t}$	Voltage magnitude at node i and time t (pu).
$\delta_{i,t}$	Angle at node i and time t (Rad).
$P_{i,t}$	Power flow at Branch i and time t (MW).
$P_{i'',t}^{dem}$	BEBs charging demand at node i'' and time t (MW).

5.3.1 Modeling of Electrified Public Bus Transit Fleet

PBT network integrates two components: N_b number of buses i.e., bus fleet, and N_r number of routes. Both could be represented with identification numbers in the form of sets and, respectively, as:

$$\mathbb{B} = \{1,\ 2,\ \ldots,\ b, \ldots,\ N_b\}, \tag{5.1}$$

$$\mathbb{R} = \{1,\ 2,\ \ldots,\ r, \ldots,\ N_r\}. \tag{5.2}$$

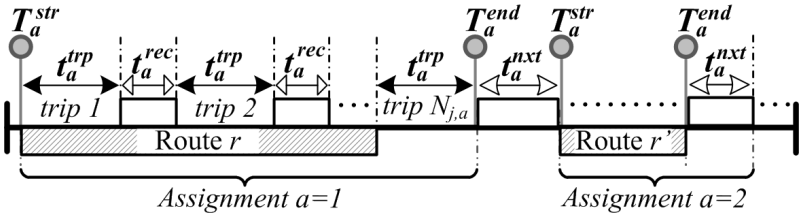

Figure 5.2: Schematic diagram for the transit schedule assignments for a bus b.

Transit operators assign buses to routes according to their operational requirements, which can be mathematically represented in the form of sets of assignments. Each set of assignments throughout the operating hours can be given as:

$$\mathbb{A} = \{1,\ 2,\ \ldots,\ a, \ldots,\ N_a\} \quad \forall\, a = [b,\ r,\ S_a], \tag{5.3}$$

where in each assignment a, bus b is scheduled for route r for a pre–specified scheduling period, defined as follows:

$$S_a = [T_a^{str},\ T_a^{end},\ t_a^{trp},\ t_a^{rec},\ t_a^{nxt},\ N_a^{trp}] \quad \forall\, a \in \mathbb{A}. \tag{5.4}$$

Fig. 5.2 shows a schematic diagram for bus b assignments described in (5.3) and (5.4). As shown in the figure, the schedule timeframe for each assignment a is defined by a start time, T_a^{str}, and an end time, T_a^{end}, for a specific assigned route r. Sequentially, each bus operates the given number of trips, N_a^{trp}, in a pre–specified time, which is followed by a given recovery time t_a^{rec} i.e., the time at which the bus is idling at the bus terminal station after each trip. It is noteworthy that each bus b may have more than one assignment with different routes and/or schedule during the daily operation hours. This concept is known in transit scheduling as interlining operation. As depicted in the figure, between two consecutive assignments there is a recovery time for the bus at the terminal defined as t_a^{nxt}. Such time is dependent on the interlining process defined by the PBT operators.

Given that the assigned buses and their operation schedules for a specific route r usually vary throughout the daily operation (i.e., peak vs off–peak operation), the set of assigned trips for each bus in a given assignment a can be defined as:

$$\mathbb{J}_a = \{1,\ 2,\ \ldots,\ j, \ldots,\ N_{j,a}\} \quad \forall\ a \in \mathbb{A}, \tag{5.5}$$

where, the number of trips in each assignment is calculated:

$$N_a^{trp} = \frac{T_a^{end} - T_a^{str} + t_a^{rec}/60}{t_a^{cyc}/60} \quad \forall\ a \in \mathbb{A}, \tag{5.6}$$

and the cycle time for each assignment a is given as follows:

$$t_a^{cyc} = t_a^{trp} + t_a^{rec} \quad \forall\ a \in \mathbb{A}. \tag{5.7}$$

It is worth noting that, the assignment end time, T_a^{end}, does not include a recovery time for the last trip, instead a recovery time between two consecutive assignments, t_a^{nxt}, is considered. For this reason, equation (5.6) considers the last trip recovery time term to maintain the equation time balance.

5.3.2 BEBs Consumption Model

Accurate estimation of the energy consumption for BEBs is vital requirement for the BEBs planning and operation [57]. In particular, BEBs energy consumption is required to determine the optimal configuration of the batteries and chargers in order to ensure satisfying the transit schedule requirement. Although, BEB manufacturers provide nominal energy consumption rate for the BEBs, the nominal values lack the special characteristics of the transit network i.e., routes topography and speed characteristics. In such a case, determining the accurate energy consumption based on the transit system characteristics of each

route is worth investigating. In this context, the battery–to–wheel energy consumption of a BEB depends on several factors; among which the most salient are: 1) route topography characteristics (i.e., length and altitude), 2) weather conditions (i.e., air density and temperature), 3) passengers occupancy rate (i.e., weight of BEB), and 4) traffic conditions (i.e., speed profile) [57]. Generally, the energy consumption depends on the forces that act upon the bus and the required traction force that overpower those forces to maintain the BEB velocity during the trip [70, 115]. Hence, the traction force at any time instant in trip j is deduced from Newton's second law of motion as:

$$F^{trc}_{t,j,a} = m_{t,j,a}\ \dot{v}_{t,j,a} + m_{t,j,a}\ g\ \sin\phi_{t,j,a} + m_{t,j,a}\ g\ f\ \cos\phi_{t,j,a} + \frac{1}{2}\ \rho\ c_t\ A\ v^2_{t,j,a} \quad \forall\, j \in \mathbb{J}_a \wedge \forall\, a \in \mathbb{A} \wedge \forall\, t \in \mathbb{T}_s. \tag{5.8}$$

Equation (5.8) expresses the required traction force to overcome inertial, gravitational, rolling resistance, and the aerodynamic forces. It is worth noting that during acceleration, the traction force is positive and thus the required power is transferred from the battery to the wheel. During deceleration, however, the traction force is negative and thus the kinetic power is transferred to recharge the battery. Accordingly, the BEBs' kinetic energy can be recovered by the regenerative braking system during deceleration situations. The required traction energy in kWh can be calculated through the summation of the bus traction force and velocity product over the duration of the trip as follows:

$$E^{trc}_{j,a} = \sum_{t \in \mathbb{T}_s} F^{trc}_{t,j,a} \cdot v_{t,j,a} \cdot \Delta t^{stp} \quad \forall\, a \in \mathbb{A} \wedge\ \forall\, j \in \mathbb{J}_a. \tag{5.9}$$

It is noted that the bus battery power is inverted through an on–board bidirectional DC/AC inverter to feed an electric motor. The motor then produces the traction power required for the bus velocity and acceleration. Therefore, the average traction energy (i.e.,

battery–to–wheel) can be given as:

$$E_{j,a}^{BtW} = E_{j,a}^{trc}/\eta^{BtW} \quad \forall\, j \in \mathbb{J}_a \wedge \forall\, a \in \mathbb{A}\,. \tag{5.10}$$

The battery–to–wheel overall efficiency is obtained via the product of the inverter, motor, and driver shaft efficiencies. For all battery electric buses, in addition to the traction energy, the BEB provides energy to supply the auxiliary loads, such as heating, cooling, lighting and sound systems. Therefore, the normalized total consumed energy per trip length in kWh/km is calculated as follows:

$$E_{j,a}^{cons} = \frac{1}{l_r}\big(E_{j,a}^{BtW} + \sum_{t \in \mathbb{T}_s} P_{b,t}^{aux} \cdot \Delta t^{stp}\big) \quad \forall j \in \mathbb{J}_a \wedge \forall a \in \mathbb{A}. \tag{5.11}$$

5.4 Integrated Utility–Transit Optimization Model

The objective function of the proposed optimization model consists of three terms as shown in (5.12): i) the cost of the BEBs battery packs, $(N_b \cdot \mathcal{E}_b \cdot C_b^{exp})$, as the product of the number of BEBs, their battery capacity, and the expenditure cost of the battery; ii) the cost of the charging units, $(\mathcal{N}_{ch} \cdot \mathcal{P}_{ch} \cdot C_{ch}^{exp})$, as the product of the number of chargers, charger rated power and the charger expenditure cost; and iii) the charger installation cost, $(\mathcal{N}_{ch} \cdot C_{ch}^{inst})$, as the product of the number of chargers and the installation cost per charger.

$$\underset{b \in \mathbb{B}}{\text{Minimize}} : N_b \cdot \mathcal{E}_b \cdot C_b^{exp} + \mathcal{N}_{ch} \cdot \mathcal{P}_{ch} \cdot C_{ch}^{exp} + \mathcal{N}_{ch} \cdot C_{ch}^{inst}. \tag{5.12}$$

Without loss of generality, it is assumed in this work that BEBs in the fleet are identical, i.e., BEBs have the same battery size in order to provide transit network operators with the flexibility to interline their buses (i.e., assign BEBs to different routes) [30]. Similarly, chargers are assumed to be equal in size. To this end, for each bus b at trip j, the departure

and arrival SOC (from/to the bus terminal) of the bus battery are constrained by the SOC limits imposed by the bus manufactures given as:

$$\mathcal{SOC}^{dep}_{b,j,a} \leq SOC^{max}_{b} \quad \forall\, b \in \mathbb{B} \wedge \forall\, j \in \mathbb{J}_a \wedge\ \forall\, a \in \mathbb{A}, \tag{5.13}$$

$$\mathcal{SOC}^{arr}_{b,j,a} \geq SOC^{min}_{b} \quad \forall\, b \in \mathbb{B} \wedge \forall\, j \in \mathbb{J}_a \wedge\ \forall\, a \in \mathbb{A}. \tag{5.14}$$

The bus manufacturers set those limits to maintain a long battery lifetime and avoid limp issues. Using the energy consumption model described in (5.11), the arrival SOC for each bus b can be calculated as:

$$\mathcal{SOC}^{arr}_{b,j,a} = \mathcal{SOC}^{dep}_{b,j,a} - 100 \times \frac{E^{cons}_{j,a}}{\mathcal{E}_b} \cdot l_r \quad \forall\, b \in \mathbb{B} \wedge \forall\, j \in \mathbb{J}_a \wedge\ \forall\, a \in \mathbb{A}. \tag{5.15}$$

Equation (5.15) determines the trip arrival SOC of each BEB as a function of its battery capacity and departure SOC, in addition to the trip consumption rate and distance. As such, the BEB battery size is constrained by the capacity limits available in the market as follows:

$$E^{min}_{b} \leq \mathcal{E}_b \leq E^{max}_{b}\ \ \forall\, b \in \mathbb{B}. \tag{5.16}$$

Equation (5.12) is also subject to the SOC charging equation upon the arrival of the BEB to the terminal after each trip:

$$\mathcal{SOC}^{dep}_{b,j,a} = \mathcal{SOC}^{arr}_{b,j,a} + \Delta\mathcal{SOC}_{b,j,a} \quad \forall\, b \in \mathbb{B} \wedge \forall\, j \in \mathbb{J}_a \wedge\ \forall\, a \in \mathbb{A}, \tag{5.17}$$

and

$$\Delta\mathcal{SOC}_{b,j,a} = \eta^{ch} \cdot \left(\frac{\left(\mathcal{P}_{ch}/60\right) \times \left(\mathcal{T}^{ch}_{b,j,a} - t^{pio}\right)}{\mathcal{E}_b} \right) \forall\, b \in \mathbb{B} \wedge \forall\, j \in \mathbb{J}_a \wedge\ \forall\, a \in \mathbb{A}. \tag{5.18}$$

Equation (5.18) shows that the added SOC ($\Delta\mathcal{SOC}_{b,j,a}$) depends on the battery capacity ($\mathcal{E}_b$), the plug–in charging power ($\mathcal{P}_{ch}$), and charging duration ($\mathcal{T}_{b,j,a}$). The design of the electrified transit system charging power is constrained by the minimum and maximum of the available charger specifications in the market, as follows:

$$P_{ch}^{min} \leq \mathcal{P}_{ch} \leq P_{ch}^{max}, \tag{5.19}$$

while, the BEBs charging duration decision variable after each trip is constrained as follows:

$$t^{pio} \leq \mathcal{T}_{b,j,a}^{ch} \leq t_{j,a}^{ch,max} \quad \forall\, b \in \mathbb{B} \wedge \forall\, j \in \mathbb{J}_a \wedge\ \forall\, a \in \mathbb{A}. \tag{5.20}$$

In the constraint set defined by (5.20) the BEBs charging duration is bounded to the charger plug–in and plug–out time duration as a lower–bound, and the maximum allowed charging duration as an upper–bound. Where, the maximum allowed charging duration is defined as:

$$t_{j,a}^{ch,max} = \begin{cases} t_a^{rec}\ \forall\, j \neq N_a^{trp} \wedge\ \forall\, j \in \mathbb{J}_a \wedge\ \forall\, a \in \mathbb{A} \\ t_a^{nxt}\ \forall\, j = N_a^{trp} \wedge\ \forall\, j \in \mathbb{J}_a \wedge\ \forall\, a \in \mathbb{A} \end{cases}. \tag{5.21}$$

As shown in (5.21), the maximum allowed charging duration equals to the recovery time when the bus has an upcoming trip within the same assignment, otherwise it equals to the recovery time for the next assignment (i.e., recovery time between consecutive assignments). In order to model the opportunity of charging for each bus during the scheduled time of operation, T^{opt} is divided into N_t equal time steps represented as follows:

$$\mathbb{T}_s = \{1,\ 2,\ \ldots,\ t, \ldots,\ N_t\}\ \forall\ N_t = \frac{T^{opt}}{\Delta t^{stp}/60}. \tag{5.22}$$

Based on (5.22), the opportunity of BEBs to charge at each time they arrive to the

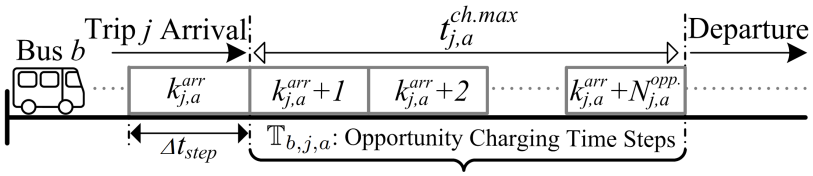

Figure 5.3: Schematic diagram for BEB charging opportunity after each trip j.

charging station is formulated in this work as a binary matrix given as:

$$\begin{bmatrix} X^1 \\ \vdots \\ X^b \\ \vdots \\ X^{N_b} \end{bmatrix} = \begin{bmatrix} x^1_{d=1} & \dots & x^1_{d=t} & \dots & x^1_{d=N_t} \\ \vdots & & \vdots & & \vdots \\ x^b_{d=1} & \dots & x^b_{d=t} & \dots & x^b_{d=N_t} \\ \vdots & & \vdots & & \vdots \\ x^{N^b}_{d=1} & \dots & x^{N^b}_{d=t} & \dots & x^{N^b}_{d=N_t} \end{bmatrix} \quad \forall\, b \in \mathbb{B} \wedge \forall\, t \in \mathbb{T}_s. \tag{5.23}$$

The dimension of the binary matrix defined in (5.23) is $N_b \times N_t$. Each binary variable in the matrix is assigned "one" when the bus charges and "zero" when the bus skips the charging opportunity. As such, each row in (5.23) represents the charging opportunities of a BEB during its scheduled operation period. It is noteworthy that the binary variables for charging opportunities of each bus are defined only in the time steps at which the bus stops at the charging station. To that end, Fig. 5.3 shows a schematic diagram of the opportunity charging for each BEB upon it arrival to the charging station after a scheduled trip j. As shown in the figure, the recovery time of the arrived bus is represented as a set of charging opportunity time steps ($\mathbb{T}_{b,j,a}$) as follows:

$$\mathbb{T}_{b,j,a} = \{k^{arr}_{j,a} + 1,\ k^{arr}_{j,a} + 2,\ \dots,\ k^{arr}_{j,a} + N^{opp}_{j,a}\}\ \forall\, b \in \mathbb{B} \wedge \forall\, j \in \mathbb{J}_a \wedge\ \forall\, a \in \mathbb{A}, \tag{5.24}$$

where,

$$k^{arr}_{j,a} = \frac{60 \times T^{str}_a + j \cdot t^{cyc}_a - t^{rec}_a}{\Delta t^{stp}}\ \forall\, j \in \mathbb{J}_a \wedge\ \forall\, a \in \mathbb{A}, \tag{5.25}$$

$$N_{j,a}^{opp} = \left\lfloor \frac{t_{j,a}^{ch,max}}{\Delta t^{stp}} \right\rfloor \quad \forall\, j \in \mathbb{J}_a \wedge \ \forall\, a \in \mathbb{A}, \tag{5.26}$$

where, $k_{j,a}^{arr}$ is the time step at which the bus arrives to the charging station after trip j and $\lfloor\ \rfloor$ is a floor function of the charging opportunity time steps, $N_{j,a}^{opp}$, at which the charging time variable ($\mathbb{T}_{b,j,a}$) can take place. Defining the charging opportunity of each BEB is crucial in the proposed utility–transit model, to allocate the BEB charging duration ($\mathcal{T}_{b,j,a}^{ch}$) decision variable within the available charging opportunities ($\mathbb{T}_{b,j,a}$), in addition to integrate the transit system charging profile into PDS. As such, the charging allocation optimally coordinate the transit system BEBs charging duration, in such a way as to: (i) minimize the number of required chargers, and (ii) ensure that there is no negative impact upon the PDS. Also, it is worth noting that the charging opportunity binary variables have impact on the optimal design of the BEBs battery capacity and charging power. For instance, the optimization problem may decide that the BEB will either not charge (i.e., binary variables are set to zero) or charge for small time duration after a certain trip due to any reason (e.g. negative impact on PDS and/or minimize the number of charger). In this context, the BEB battery capacity and/or the charger size might increase to ensure that the BEB has sufficient energy to perform the next trip service. Hence, the binary vector for any BEB b is constrained by the opportunity charging time steps as follows:

$$\sum_{t \in \mathbb{T}_{b,j,a}} x_{d=t}^{b} = \begin{cases} N_{X_{j,a}}, & \forall\, \mathbb{T}_{b,j,a} \subseteq \mathbb{T}_s \\ 0, & \text{Otherwise} \end{cases} \quad \forall\, b \in \mathbb{B} \wedge \forall\, j \in \mathbb{J}_a \wedge \ \forall\, a \in \mathbb{A}, \tag{5.27}$$

$$N_{X_{j,a}} = \left\lceil \frac{\mathcal{T}_{b,j,a}^{ch}}{\Delta t^{stp}} \right\rceil \quad \forall\, b \in \mathbb{B} \wedge \forall\, j \in \mathbb{J}_a \wedge \ \forall\, a \in \mathbb{A}, \tag{5.28}$$

where $\lceil\ \rceil$ is a ceil function of the required charging time steps. Equation (5.27)–(5.28) limits the charger utilization to the number of time steps that satisfies the charging time. In order to avoid the assignment of discontinuous charging for the bus during the charging

opportunity duration, the following constraint is applied:

$$|x^b_{d=y} - x^b_{d=y-1}| + \sum_{t \in \mathbb{T}_{b,j,a}} |x^b_{d=t+1} - x^b_{d=t}| = \begin{cases} 0, \ \forall \ \mathcal{T}^{ch}_{b,j,a} = t^{pio} \\ 2, \ \forall \ \mathcal{T}^{ch}_{b,j,a} > t^{pio} \end{cases}$$
$$\forall \ y = k^{arr}_{j,a} + 1 \wedge \ \forall \ b \in \mathbb{B} \wedge \forall \ j \in \mathbb{J}_a \wedge \ \forall \ a \in \mathbb{A}. \tag{5.29}$$

Equation (5.29) states that during the charging opportunity period, only one rising edge (i.e., charging status changes from 0 to 1) can exist. Similarly, one falling edge (i.e., charging status changes from 1 to 0) can exist. Therefore, the BEB charging status changes twice, if the BEB charges during the available charging time. Accordingly, equation (5.29) will be equal two, otherwise equation (5.29) is equal zero that means no change in the charging status. The number of required chargers is function of the assigned charging in (5.23) and it can be represented mathematically as follows:

$$\mathcal{N}_{ch} = \text{Max}\Big(\sum_{b \in \mathbb{B}} X^b\Big), \tag{5.30}$$

as such, the number of chargers in (5.30) is the maximum of the summation of the binary matrix in equation (5.23) at each time t, which is constrained by its design limits as follows:

$$N^{min}_{ch} \leq \mathcal{N}_{ch} \leq N^{max}_{ch}. \tag{5.31}$$

In this regard, the BEBs charging coordination in (5.23) plays a key role in minimizing the number of the required chargers as per the objective function in (5.12).

The objective in (5.12) is also subjected to the operation constraints of the PDS including the active and reactive power balance given in (5.32) and (5.33), respectively [131].

$$P^{gen}_{i,t} - P^{dem}_{i,t} = |V_{i,t}| \sum_{i' \in \mathbb{I}} \Big[|V_{i',t}| \cdot |Y_{ii'}| \times Cos\big(\delta_i - \delta_{i'} - \theta_{ii'}\big)\Big] \forall i \in \mathbb{I} \wedge \forall t \in \mathbb{T}_s, \tag{5.32}$$

$$Q_{i,t}^{gen} - Q_{i,t}^{dem} = |V_{i,t}| \sum_{i' \in \mathbb{I}} \Big[|V_{i',t}| \cdot |Y_{ii'}| \times Sin\big(\delta_i - \delta_{i'} - \theta_{ii'}\big) \Big] \forall i \in \mathbb{I} \wedge \forall t \in \mathbb{T}_s. \quad (5.33)$$

It is noted that the power demand of node i'' at which the BEB charging station is located can be expressed at a given time t as follows:

$$P_{i'',t}^{dem} = \mathcal{P}_{ch} \cdot \sum_{b \in \mathbb{B}} x_{d=t}^{b} \;\; \forall\, t \in \mathbb{T}_s \wedge \forall\, i'' \in \mathbb{I}, \quad (5.34)$$

where, equation (5.34) express the aggregated charging demand of the transit system as a function of the charger power and the BEBs charging status in (5.23) at each time t.

Equation (5.12) is also subjected to the allowable node's voltage limit and the branches' capacity limits defined as:

$$V_i^{min} \leq V_{i,t} \leq V_i^{max} \quad \forall\, i \in \mathbb{I} \;\wedge \forall\, t \in \mathbb{T}_s, \quad (5.35)$$

$$|P_{i,t}| \leq P_i^{max} \quad \forall\, i \in \mathbb{I} \;\wedge \forall\, t \in \mathbb{T}_s. \quad (5.36)$$

5.5 Simulation Results

The optimization model described in (5.12)–(5.36) is a Mixed Integer Non-Linear Programming (MINLP) problem. In this work, the proposed formulated optimization problem is solved using the Basic Open-source Nonlinear Mixed INteger (BONMIN). BONMIN solver uses a combined Interior Point nonlinear programming and branch and cut linear programming techniques for solving the MINLP optimization problem [132]. Also, it is worth noting that BONMIN algorithm has the functionality to incorporate heuristic techniques to handle large MINLP problems. In particular, the incorporated heuristic techniques help speeding up the detection of an infeasible solution search path and thus rapidly finds a feasible solution [133]. BONMIN optimization solver is bundled as a MATLAB built-in

Belleville Transit Operational Data

a	b	r (routes ID)	S_a					l_r	$N_{j,a}$
			$T_a^{st.}$	T_a^{end}	t_a^{trp}	$t_a^{rec.}$	t_a^{nxt}		
1	1	Plaza Dundas	6:30	18:25	25	5	725	9.564	24
2	2	Parkwood Heights	5:00	20:25	25	5	545	9.705	31
3	3	College East	5:30	19:55	25	5	575	12.392	29
4	4	Mall North Front	6:30	9:55	25	5	5	9.601	7
5	4	Mall North Front	10:00	16:40	40	20	20	9.601	7
6	4	Mall North Front	17:00	20:25	25	5	605	9.601	7
7	5	Mall North Front	10:30	17:10	40	20	1055	9.601	7
8	6	Parkdale Mall	5:00	10:25	25	5	20	9.448	11
9	6	Parkdale Mall	11:15	17:55	40	20	665	9.448	7
10	7	Parkdale Mall	10:45	17:25	40	20	5	9.448	7
11	7	Parkdale Mall	17:30	20:25	25	5	860	9.448	6
12	8	Avondale	6:30	18:25	25	5	725	10.378	24
13	9	Loyalist	6:30	20:55	25	5	605	12.157	29
14	10	North Park	6:30	20:25	25	5	725	9.998	28
15	11	Quinte Sport Centre	8:30	19:55	25	5	755	8.508	23

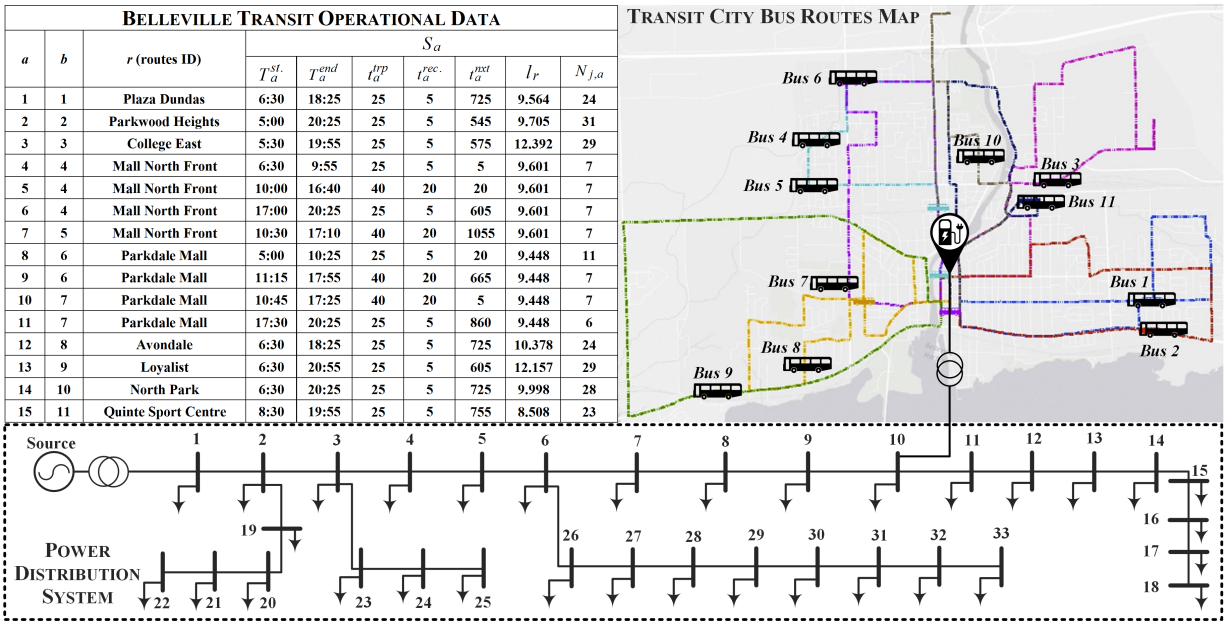

Figure 5.4: Belleville city PBT map, BEBs assignments data, and its integration with the 33-power distribution system.

function in the OPTimization Interface (OPTI) toolbox [134]. Hence, the problem has been coded and solved using the interfaced OPTI toolbox. The coded optimization algorithm is executed in a PC with the following specifications: Core i7-6700, 3.4 GHz CPU, 16 GB RAM, and 64 bit windows operating system. The convergence tolerance is set to 10^{-7}, while, the maximum number of iterations, function evaluations and integer solver nodes are set to 10^4.

Fig. 5.4 shows a schematic diagram for the integrated utility-transit system utilized to test the effectiveness of the proposed model. As shown in the figure, the studied integrated utility–transit system includes a 33–bus PDS coupled with a PBT network at node 10, besides the transit network weekday operational timetable. The PBT network shown in Fig. 5.4 is a real-world network for the city of Belleville in Ontario, Canada. For the purpose of this study, the network is assumed to be fully electrified i.e., all diesel buses are replaced by BEBs. Due to the unavailability of the PDS data at Belleville, the well-known

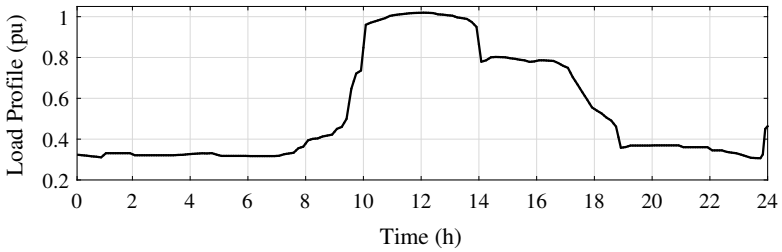

Figure 5.5: Typical daily load profile for the studied system.

Table 5.2: Data of on–Board Bus Batteries and Fast Chargers

$SOC_b^{min} = 20\%$	$SOC_b^{max} = 90\%$
$E_b^{min} = 75$ (kWh)	$E_b^{max} = 500$ (kWh)
$P_{ch}^{min} = 75$ (kW)	$P_{ch}^{max} = 500$ (kW)
$N_{ch}^{min} = 1$	$N_{ch}^{max} = 6$
$t^{pio} = 2$ (minutes)	$C_b^{exp} = 300$ ($/kWh)
$C_{ch}^{inst} = 450$ ($/kW)	$C_{ch}^{exp} = 35{,}000$ ($/charger)
BEB GVWR = 17,200 (kg)	$P_{b,t}^{aux} = 15$ (kW)

GVWR: Gross vehicle weight rating

33 bus PDS is utilized in this study [135]. The charging station of the BEBs is located at the bus terminal that is usually located at the city center [28]. In this context, the charging station is assumed to be connected to node 10, which is the PDS center load. Fig. 5.5 shows a typical daily load profile that is adopted for the studied PDS system loads i.e., without the BEBs. As such, the acceptable voltage deviation is considered as per the American National Standards Institute Range A (i.e., 5%) [136]. Table 5.2 shows the input parameters for the bus batteries and the fast chargers [111, 137], where the time step of the studied utility–transit model is 5 minutes.

Given the temporal variation in the traffic flow characteristics, the speed profile is not constant during the scheduled trips. Therefore, three traffic flow conditions, using the ratio (v/c) of traffic volume (v) to roadway practical capacity (c), are considered to accommodate

the temporal variation in traffic conditions. These traffic conditions are free flow, light, and congested traffic. In addition, the speed profile of each bus under each traffic flow condition is calculated and aggregated for the transit network. To that end, two scenarios are carried out in this work to determine the optimal BEBs configuration for the studied transit network. Scenario 1 is the base case scenario, where neither the utility model nor the traffic conditions are considered. In this scenario, the rate of energy consumption of the BEBs is assumed to be fixed at an average of 1.05 kWh/km as claimed by most of the bus manufactures [27]. Scenario 2 represents the proposed integrated model that accounts for traffic flow conditions and the utility operational requirements stated in (5.32)–(5.36).

In Scenario 2, the BEBs energy consumption models are calculated using the Advanced Vehicle Simulator (ADVISOR) according to their manufacture technical specifications, routes topology, trips time frame, and the corresponding traffic flow conditions. ADVISOR is a simulation tool for vehicle modeling developed by the National Renewable Energy Laboratory of the United States Department of Energy. In order to accurately calculate the energy consumption in Scenario 2, the BEB speed profile, route topography, and auxiliary loads rating should be inputted to the BEBs' energy consumption model shown in Section 5.3.2. For instance, Fig. 5.6 (a)–(c) show the elevation and gradient for Loyalist route (one of Belleville city PBT routes shown in Fig. 5.4) and the speed profile for its assigned BEB in a congested traffic condition, respectively. Figs. 5.7 (a) shows the corresponding power consumption in Scenario 2 for the simulated trip. It is noted that the positive power consumption in Fig. 5.7 (a) refers to the drawn power from the BEB energy storage units to drive the BEB and supply the auxiliary loads, while the negative power represents the recovered power during deceleration. Figs. 5.7 (b) shows the BEB SOC in both scenarios (i.e., Scenario 1 and Scenario 2) for the simulated trip. As depicted in the figure, the first scenario SOC is linear as it lacks the route characteristics, while the second scenario SOC reflects the route topography and speed characteristics. The simulation has been conducted for all eleven routes at the three traffic conditions i.e., free flow, light, and congested traffic.

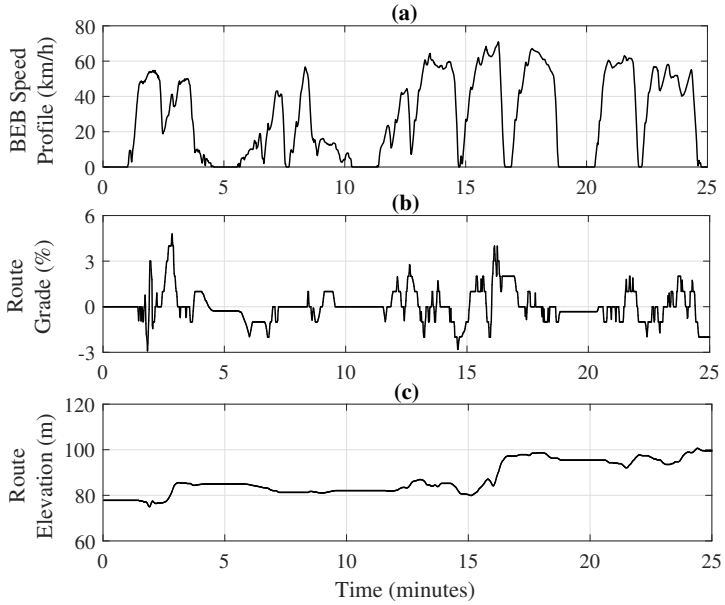

Figure 5.6: Scenario 2: (a) Speed profile, (b) gradient, and (c) elevation, for Loyalist route.

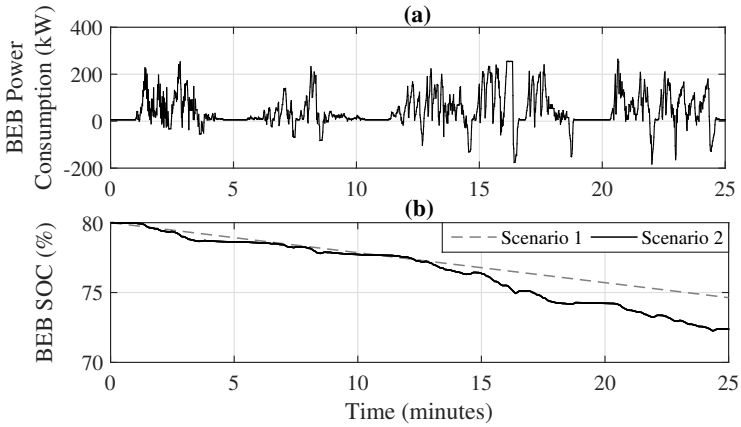

Figure 5.7: BEB #9 operated at Loyalist route (a) Scenario 2 energy consumption, and (b) Scenario 1 and Scenario 2 SOC.

Table 5.3 shows the average rate of energy consumption for the studied transit network under different traffic conditions. It should be noted that the uncertainty associated with weather condition is not considered in the model, and the resulted energy consumption is aggregated at the route level. The aggregation of the energy consumption for the transit

Table 5.3: BEBs Energy Consumption Based on Traffic Flow Condition

Parameters	Free Traffic ($v/c = 0.35$)	Light Traffic (v/c =0.55)	Congested Traffic ($v/c = 0.92$)
Consumption (kWh/km)	0.825	1.1	1.65
Time frame (h)	20:00–7:00	9:00–15:00, 18:00–20:00	7:00–9:00, 15:00–18:00

Table 5.4: Optimal BEBs Configuration

Scenario (ID)	$\mathcal{N}_{ch}$	$\mathcal{P}_{ch}$ (kW)	$\mathcal{E}_b$ (kWh)	Cost (k$)	Trips consumption (MWh)
Scenario (1)	3	500	75	1027.5	2.65
Scenario (2)	4	250	300	1580	3.21

network is essential from the transit agencies point of view, in order to standardize their BEBs fleet. Therefore, the BEBs can be scheduled to serve any of the transit system routes. The data in Table 5.3 is inputted to the proposed optimization model. Further, a sensitivity analysis between the feasible BEBs configuration is carried out for the studied scenarios. This is to concisely evaluate: 1) the impact of integrating the PDS model; and 2) quantify the trade-off relation between the BEBs optimal configurations.

5.5.1 Optimal BEBs Configuration

Table 5.4 shows the optimal configuration of the BEB system for the studied transit network in the two scenarios. The table shows also the cost of each configuration and the total daily consumed energy by the electric PBT network. As shown in the table, accounting for the PDS and the traffic flow conditions requires an increase of the net transit electrification cost by 53.8%, compared to Scenario 1 in order to satisfy the scheduled transit operation. It is also noticed that accurate consideration of the traffic flow conditions increases the BEBs fleet energy consumption by almost 21%. Figs. 5.8 (a)–(b) show the BEB charging profile of the two studied scenarios. Further, the impact of BEBs charging on the PDS voltage

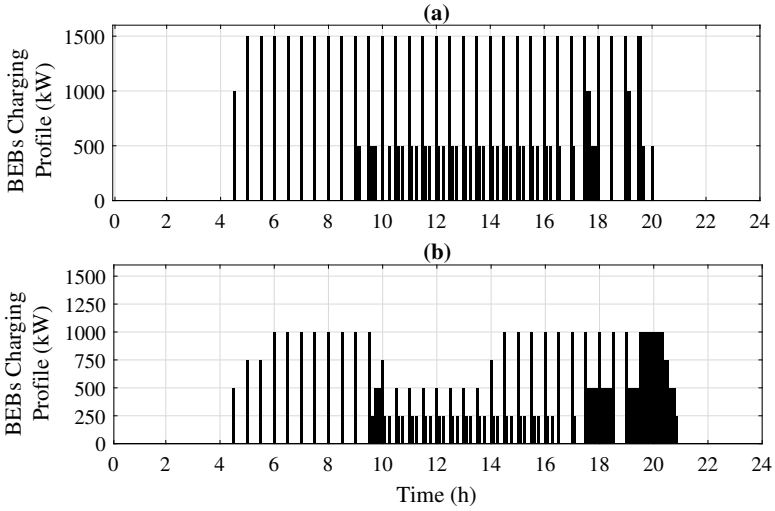

Figure 5.8: The BEBs charging profile at: (a) Scenario 1, and (b) Scenario 2.

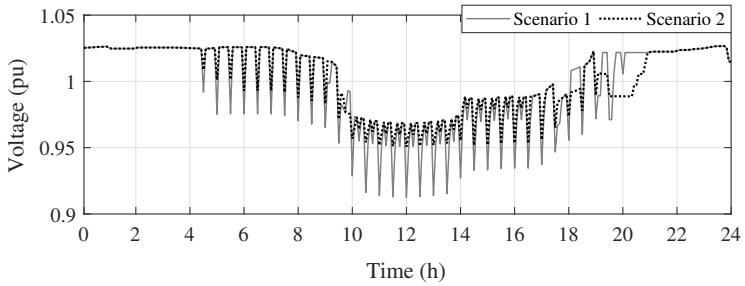

Figure 5.9: The PDS-wide minimum voltage profile for the studied scenarios.

profile is shown in Fig. 5.9, which represents the minimum voltage magnitude across the entire PDS at each time step. As depicted in the figure, without considering the PDS in the design of the BEB configuration, an undervoltage occurs due to the scheduled charging of the BEBs during peak loading conditions. Fig. 5.8 (b) and Fig. 5.9, however, show that the proposed integrated model adapted the BEBs configuration and their charging profile in such a way as to do not violate the prescribed voltage limit of the PDS. For this reason, the required charger size in Scenario 2 is found to be 250 kW compared to 500 kW in Scenario 1, as shown in Table 5.4. Yet, in order to maintain the scheduled operation of the transit network, the decrease in the charger size requires an increase in the BEBs battery from 75 to 300 kWh. With a larger battery capacity, BEBs could complete few

consecutive trips without the need of being fully charged. In addition, as illustrated in Fig. 5.8, BEBs with larger battery capacities require more time to be fully charged after the completion of their daily assignments to prepare for the next day trips. The results also show that although the charger size in Scenario 2 is decreased (compared to Scenario 1), the available chargers are not fully utilized during heavy–loading conditions of PDS. For example, during the time of 10:00 to 14:00, only two chargers at a time can be utilized out of four available chargers as shown in Fig. 5.8 (b).

5.5.2 Sensitivity Analysis of the BEBs Configurations

The results of the above subsection shows that there is a trade-off between the choices of the BEB battery capacity and the charger size for a transit network. To that end, a sensitivity analysis is conducted in this section using the proposed optimization model for the two studied scenarios. Given that, the BEB battery capacity is modular, different battery capacities is considered for the sensitivity analysis. Where, the studied battery capacities are within the minimum and maximum limits shown in Table 5.2, with a 25 kWh unit interval. Figs. 5.10 (a) and (b) show the optimal configurations for the electrified transit city bus at different number of chargers for Scenarios 1 and 2, respectively. As shown in Fig. 5.10, the relation between the required battery capacity and the required charger size is inverse proportional i.e., the battery capacity decreases with the increase of the charger size. As shown in Fig. 5.10 (a), the maximum required battery capacity is found to be 425 kWh for three 75 kW chargers. Fig. 5.10 (b), however, shows that the maximum battery capacity for Scenario 2 is 500 kWh at 75 kW charger size for three chargers and above. Hence, in the latter scenario, increasing the number of chargers at 75 kW rated power does not reduce the required battery capacity. As such, a 500 kWh is required for the BEBs battery capacity, so the BEBs can deliver the assigned transit schedule given the low charger size of 75 kW. This is mainly because the lower charger size cannot provide

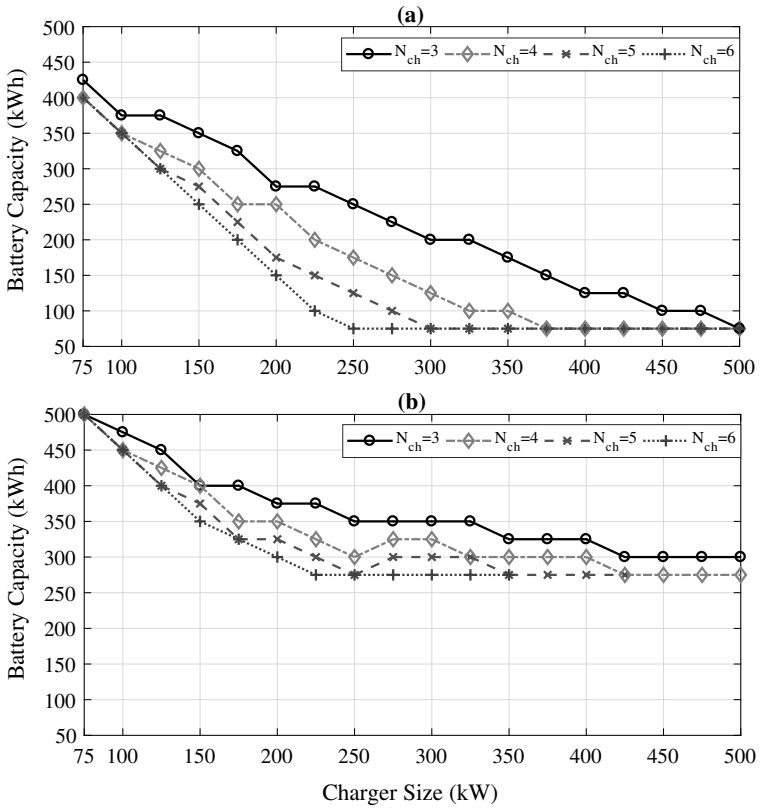

Figure 5.10: Feasible BEBs configurations at different number of chargers for; (a) Scenario 1, and (b) Scenario 2.

sufficient energy to the BEBs during the recovery time. Therefore, a large battery capacity is needed regardless increasing the probability of BEBs charging opportunity (i.e. number of charger).

It is also noticed that, the BEBs battery capacity in Scenario 2 is always higher than Scenario 1, because of the PDS incapability to charge the BEBs during high loading conditions. Therefore, larger battery capacity is required in order to satisfy the transit schedule and BEBs SOC constraints without violating the PDS constraints. For instance, the results show that only 75 kWh battery is required for three 500 kW chargers in Scenario 1 optimal configuration as shown in Table 5.4. However, as depicted in Fig. 5.10 (b), the required battery capacity for three 500 kW chargers is found to be 300 kWh for Scenario 2 due to the imposed constraints of the PDS.

5.6 Discussion and Summary

This chapter proposes an integrated utility-transit mathematical model for the optimal configuration design of transit BEB systems. The configuration includes the BEBs battery capacity, chargers size, and the number of required chargers. The objective of the optimization problem is to minimize the electrification expenditure cost of PBT networks. The proposed optimization algorithm takes into account the operation requirements of both power distribution and transit networks. It also incorporates accurate modeling for the BEBs energy consumption considering bus models, route topology, and traffic conditions. A real-world transit system has been utilized to validate the effectiveness of the proposed algorithm. The results show that the operation practices of both transit and power networks are highly sensitive to the BEB configuration. It is noted in the case studies that during heavy power loading conditions, PDS may not able to satisfy the charging requirements of the BEB fleet when the BEBs configuration and charging schedule are not optimally designed. When PDS is highly congested under certain BEB configuration, the following design aspects related to the BEB system can be considered. i) Increase the BEBs' battery capacity to deliver few consecutive trips without the need for a charging session. ii) Adjust the charging schedule so less number of BEBs could have the opportunity to charge during heavy–loading conditions. iii) Decrease the charger's size to allow BEBs to be charged without impacting the PDS during heavy–loading conditions. iv) Increase the number of chargers to sufficiently charge the BEBs before and after the heavy–loading conditions, given that BEBs will not have the full opportunity to charge during such conditions.

Chapter 6
Optimal Scheduling of Hydrogen Storage for Fuel Supply and Capacity Based Demand Response

6.1 Introduction

As the emerging technology offers more economic and efficient mechanisms for hydrogen production, FCEVs are expected to be deployed more extensively in the near future. Proliferation of hydrogen fueling stations throughout the transportation network and justifying their economic viability are key factors to the success of the FCEVs. On the other hand, in today's deregulated market environment, many governments are encouraging private investors to invest in key infrastructures including the hydrogen fueling stations. To that end, this chapter presents a new model for optimal scheduling of hydrogen fueling stations to both serve the transport sector and the electricity market operator. The model schedules the stations to yield the maximum revenue via the stacked profit from multiple sources.

The main objectives and contributions of the present chapter are listed in the following:

1. A new central scheduling model is proposed to coordinate distributed hydrogen fueling station in order to (i) exploit the lower electricity market prices to reduce the power purchase cost; (ii) contribute to the Capacity–Based Demand Response (CBDR) program in order to further enhance the economic feasibility of the stations; and (iii) satisfy the hydrogen demand by the transportation sector. The model considers profitability constraints and dynamic hydrogen pricing mechanisms in the optimization problem to ensure that the expected profit is achieved.

2. The CBDR management is incorporated into the optimization problem. The stacked benefit from the CBDR market and the hydrogen sale to the transportation sector enhances the economic viability of the stations. Thus, the expected profit can be achieved at the lower hydrogen sale prices.

3. The concept of the distributed coordination for the hydrogen fueling stations to respond to the DR signal is incorporated into the model. Based on this concept, hydrogen fueling stations might have different response behaviors to the DR signal depending on their SOC and the hydrogen demand by the transportation sector; yet they all contribute to the CBDR program as a whole by following the DR signal.

To that end, Table 6.1 presents the definition of this chapter indices, sets, constant, time–dependent parameters, and variables.

Table 6.1: Chapter 6 Nomenclature

A. Indices

t	Index of time steps.
h	Index of hydrogen fueling stations.
n	Index of power network nodes/feeders.

B. Sets

$\mathcal{T}$	Set of optimization problem time steps.
$\mathcal{H}$	Set of hydrogen fueling stations.
$\mathcal{N}$	Set of nodes in power distribution system.

C. Constants

Δt	Time interval of the optimization problem (h).
T	Optimization horizon (h).
F_h^{min}	Minimum hydrogen outflow of electrolyzer (m^3/h).
F_h^{max}	Maximum hydrogen outflow of electrolyzer (m^3/h).
V_n^{min}	Minimum voltage magnitude at Node n (pu).
V_n^{max}	Maximum voltage magnitude at Node n (pu).
P_n^{max}	Maximum power at Branch n (MW).
$Y_{nn'}$	Admittance magnitude from Node n to n' (pu).
$\theta_{nn'}$	Admittance angle from Node n to n' (Rad).
SOC_h^{min}	Minimum hydrogen state of charge (m^3).
SOC_h^{max}	Maximum hydrogen state of charge (m^3).
η^{PtH}	Efficiency of the PtH unit (%).
η^{F}	Faraday's efficiency (%).
F	Faraday's constant (MAh/m^3).
η^{Cmp}	Compression efficiency (%).
LHV_{H_2}	Lower heat value of hydrogen (MWh/kg).
λ_{H_2}	Hydrogen density (kg/m^3).
η^{PtH}	Efficiency of the PtH unit (%).
v^{PtH}	PtH unit input voltage (V).
Π^{PtH}	Power to hydrogen conversion factor (m^3/MWh).
γ^{Dsp}	Hydrogen storage energy dissipation rate (%/h).
DR^{Hr}	Normalized demand response contribution (h/yr).
$\alpha^{Adj,Prc}$	Penalty factor for hydrogen prices (m^3/h).
$\alpha^{Adj,ER}$	Penalty factor for expected revenue deviation (1/h).
$DR^{U,Prc}$	CBDR utilization price ($/MW).
$DR^{A,Prc}$	CBDR availability price ($/h).
R^{Exp}	Expected revenue for hydrogen stations ($).
R^{Dev}	Acceptable revenue deviation ($).
$Prc^{H_2,min}$	Hydrogen minimum sale price ($/$m^3$).
$\beta_h^{Adj,Prc}$	Price adjustment factor to control hydrogen prices.
C^{PtH}	Operating cost of the PtH unit ($/$m^3$).

Table 6.1: Chapter 6 Nomenclature ... continued

D. Time–Dependent Parameters

Prc_t^{Elc} Electricity prices ($/MWh).

$F_{h,t}^{Dem}$ Hydrogen demand by transportation sector (m^3/h).

SOC_t^{CBDR} Available state of charge for CBDR (m^3).

$P_{n,t}^{Dem}$ Power demand at Node n (MW).

$Q_{n,t}^{Dem}$ Reactive power demand at Node n (MVAr).

P_t^{Sgl} Demand response signal (MW).

ρ_t^{PtH} PtH unit pressure (bar).

ρ_t^{Sto} Hydrogen storage pressure (bar).

E. Variables

$\boldsymbol{Prc}_{h,t}^{H_2}$ Hydrogen sale price ($/$m^3$).

$\boldsymbol{Prc}_{h,t}^{H_2,Adj}$ Slack variable for hydrogen sale price ($/$m^3$).

$\boldsymbol{P}_{h,t}^{PtH}$ Input power of PtH unit (MW).

$\boldsymbol{Q}_{h,t}^{PtH}$ Reactive power of PtH unit (MVAr).

$\boldsymbol{P}_{h,t}^{Cmp}$ Input power of compressor at Station h (MW).

$\boldsymbol{F}_{h,t}^{PtH}$ Outflow of hydrogen from electrolyzer unit (m^3/h).

$\boldsymbol{SOC}_{h,t}^{lb}$ Lower bound SOC (m^3).

$\boldsymbol{SOC}_{h,t}$ SOC of the hydrogen station (m^3).

$\boldsymbol{SOC}_{h,t}^{A,DR}$ Slack variable for DR SOC (m^3).

$\boldsymbol{R}_t^{Adj,Exp}$ Slack variable to adjust the deviation of the expected revenue for hydrogen stations ($).

$\boldsymbol{P}_{n,t}^{Gen}$ Power generation at Node n (MW).

$\boldsymbol{Q}_{n,t}^{Gen}$ Reactive power generation at Node n (MVAr).

$\boldsymbol{\delta}_{n,t}$ Voltage angle at Node n (Rad).

$\boldsymbol{V}_{n,t}$ Voltage magnitude at Node n (pu).

$\boldsymbol{P}_{n,t}$ Power flow at Branch n (MW).

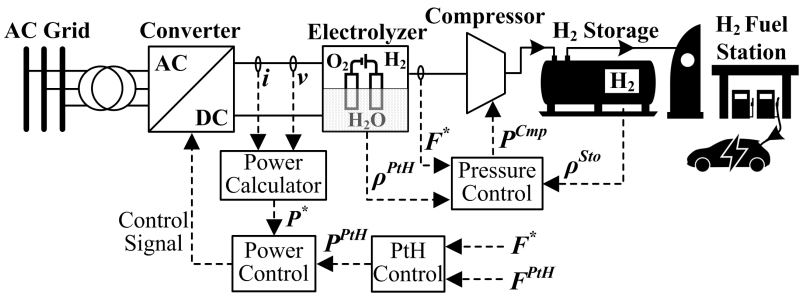

Figure 6.1: PtH unit interface with power grid and its control structure.

6.2 Problem Description

Fig. 6.1 shows a block diagram of the PtH interface with power grid and its power circuit control structure. The operational principle of the PtH system involves applying direct current through two electrodes, which are immersed in water to diffuse the water molecules into hydrogen and oxygen. In such a setup, the PtH unit requires a high level of DC current at a low voltage supply [138]. For this reason, the AC power needs to be rectified and regulated through an AC–DC converter [139]. The control system mainly consists of the PtH flow rate and pressure control [140], where the steady–state equations showing the PtH flow rate are given as follows [140]:

$$\boldsymbol{P}_{h,t}^{PtH} = \frac{\boldsymbol{F}_{h,t}^{PtH}}{\Pi^{PtH} \cdot \eta^{PtH}} \qquad \forall t \in \mathcal{T} \wedge \forall h \in \mathcal{H}, \tag{6.1}$$

$$\Pi^{PtH} = \frac{\eta^{F}}{2 \cdot F \cdot v^{PtH}} \qquad \forall t \in \mathcal{T} \wedge \forall h \in \mathcal{H}, \tag{6.2}$$

$$\eta^{PtH} = \frac{\boldsymbol{F}_{h,t}^{PtH} \cdot LHV_{H_2} \cdot \lambda_{H_2}}{\boldsymbol{P}_{h,t}^{PtH}} \qquad \forall t \in \mathcal{T} \wedge \forall h \in \mathcal{H}. \tag{6.3}$$

The control system generates the switching signals for the converter that would control the PtH input power flow, and thus, the produced hydrogen. The PtH system utilizes a feedback controller to adjust the pressure of the storage reservoir [140]. To that end, the pressure control mechanism generates a reference signal for the compressor input power

(P^{Cmp}), depending on the electrolyzer and hydrogen pressures as feedback quantities; the steady–state equation of the pressure controller is given as follow:

$$\boldsymbol{P}_{h,t}^{Cmp} = \frac{\boldsymbol{F}_{h,t}^{PtH}}{\eta^{Cmp}} \cdot \frac{k \cdot R \cdot T^{PtH}}{k-1} \Big[\Big(\frac{\rho_t^{Sto}}{\rho_t^{PtH}} \Big)^{\frac{k-1}{k}} - 1 \Big] \quad \forall\, t \in \boldsymbol{\mathcal{T}} \wedge \forall\, h \in \boldsymbol{\mathcal{H}}, \tag{6.4}$$

where, k, R, and T^{PtH} represent the polytropic coefficient, gas constant, and PtH temperature, respectively.

Hydrogen fueling stations are likely to be distributed throughout the transport network to support the consumers (i.e., FCEVs) in a wide area. A central controlling mechanism would, then, be required to supervise and schedule the stations connected at several points in the power distribution system. Central controllers have been used in industry and widely studied in the literature. Central controllers require bidirectional communication channels to collect the data, and then send the scheduling/control signals to multiple devices. Such controllers, for instance, aim to collect data from multiple assets in a microgrid and optimize the operation of the microgrid by providing the optimal setpoints to different assets such as generators, dispatchable loads, energy storage, etc. [141]. In the proposed algorithm, the central controller aims to optimize the joint operation of the distributed hydrogen fueling stations. In this regard, the received signals by the central controller include: (i) the hydrogen demand by the transportation sector (i.e., distributed hydrogen fueling stations), (ii) the hydrogen fueling station SOC, (iii) the electricity market prices, and (iv) the DR signal by the electricity market operator. The central controller processes the received data and determines the optimal setpoints of the PtH units for each hydrogen fueling station. In addition, hydrogen sale prices are decided by the central controller. It is also worth noting that the power grid's constraints are met by the scheduling model.

The general layout for the integrated hydrogen stations and power grid is represented in Fig. 6.2. As shown in the figure, it is assumed that the PtH unit (i.e., electrolyzer) is placed on site at the hydrogen fueling stations, where the hydrogen is supplied to the consumer.

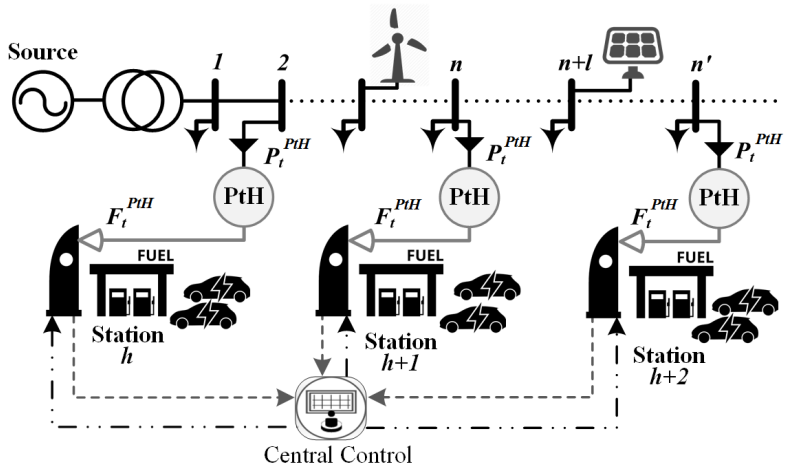

Figure 6.2: Hydrogen storage scheduling using a central controller.

Several electrolyzers are connected at different locations in the power distribution system that would convert the electricity to the hydrogen, which is stored in local storage and supplied to the consumers. In such a setup, there is also a potential for electrolyzers to act as dispatchable loads to provide some services to the power grid. The electrolyzers can participate in various DR programs in the electricity market, thereby achieving a higher revenue level. This work has targeted CBDR, which is a promising source of revenue for dispatchable consumers governed by some power system operators in North America [142]. The CBDR program allows the contracted DR providers to participate in the wholesale market by accepting the DR signals. In particular, the electrolyzers under CBDR are scheduled to take less power from the grid when such an action is demanded by the market operator. The storage would, however, need to be scheduled properly to provide reserve to support the transport sector since electrolyzers would have to generate less hydrogen when they receive DR signals during peak power demand.

This work aims to develop an optimal scheduling model that would incorporate DR signals into the optimization model to prepare the storage for the following purposes:

- Utilizing the lower/negative electricity market prices for hydrogen production to re-

duce the power purchase cost.

- Contributing to the CBDR program to further improve the economic feasibility of the investment in hydrogen stations.

While the main objective of the hydrogen stations would be fuel supply to the transport sector, the CBDR is chosen as the second objective due to the following reasons:

- Hydrogen fueling stations are dispatchable and can easily follow the DR signals issued by the market.
- Hydrogen fueling stations can accommodate lower power consumption for a short period of time once such a request is made by the market. In such a case, hydrogen stations rely on the reserved hydrogen in the storage.
- Several stations could be distributed over the network as a chain; thus, there would be a sizable amount of stored energy which may not always be needed by the transportation sector. The stored hydrogen can then be utilized to compensate for the lack of required hydrogen demand at peak power periods, usually when a DR signal is issued. This would enable the facility to serve the electricity market by participating to the CBDR program.

It is noteworthy that once the DR signal is issued, the model would prioritize the DR contribution to the hydrogen production. Such a mechanism is accommodated in the objective function using slack variables as explained in Section 6.3. The DR contribution is given the highest priority in order to (i) ensure that the stations can fulfill their commitment to the market, and (ii) enhance the generated profit since the DR revenue is usually higher than the revenue resulted from fuel supply during the DR signal time duration, i.e., the first objective [142].

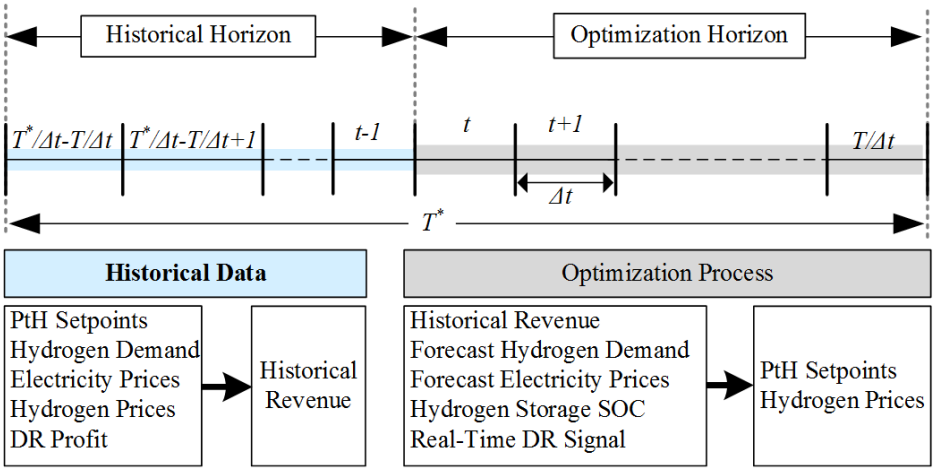

Figure 6.3: Schematic of the proposed central scheduling mechanism.

Fig. 6.3 shows the scheduling mechanism of the central controller that aims to optimize the setpoint of the hydrogen fueling stations and determine the hydrogen sale prices. In order to consider the load and renewable generation variability, the scheduling setpoints are recursively updated by reprocessing the optimization problem at each time step [143]. As shown in Fig. 6.3, the scheduling model stores and utilizes the historical revenue data that are added to the future revenue values; based on which the hydrogen sale prices are decided to ensure that the expected revenue is obtained over a given time period (i.e., T^*). The computed profit is resulted from the sum of the historical revenue data in the past several hours and the look–ahead revenue quantities. This ensures that unexpected and sudden changes in the market would not lead to abrupt changes in the hydrogen prices. As such, the hydrogen price follows a smoother trend to ensure that the longer–term revenue values meet the expectations rather than very short–term revenues.

6.3 Proposed Model

The proposed model for optimal scheduling of the PtH stations are formulated in this section. The model aims to (i) maintain the expected profit via stacked profit, and (ii) offers

the lowest values for the hydrogen sale prices. The objective function of the optimization problem is formulated as:

$$\underset{\boldsymbol{P}_{h,t}^{PtH},\ \boldsymbol{Prc}_{h,t}^{H_2},\ \boldsymbol{Prc}_{h,t}^{H_2,Adj},\ \boldsymbol{R}_t^{Adj,Exp}}{\text{Maximize}}:$$

$$\sum_{t\in\mathcal{T}}\left(\sum_{h\in\mathcal{H}} F_{h,t}^{Dem}\cdot\boldsymbol{Prc}_{h,t}^{H_2} - \sum_{h\in\mathcal{H}}\boldsymbol{P}_{h,t}^{PtH}\cdot Prc_t^{Elc}\right.$$

$$\left. -\alpha^{Adj,ER}\cdot\boldsymbol{R}_t^{Adj,Exp} - \sum_{h\in\mathcal{H}}\alpha^{Adj,Prc}\cdot\boldsymbol{Prc}_{h,t}^{H_2,Adj}\right)\cdot\Delta t. \tag{6.5}$$

The objective function stated by (6.5) aims to maximize the profit of hydrogen fuel stations, including the following terms:

1) Controlling the hydrogen price as a decision variable to meet the profitability constraint: $\sum_{h\in\mathcal{H}} F_{h,t}^{Dem}\cdot\boldsymbol{Prc}_{h,t}^{H_2}$

2) Deciding the optimal setpoints of the PtH unit to purchase the power at lower market prices: $\sum_{h\in\mathcal{H}}\boldsymbol{P}_{h,t}^{PtH}\cdot Prc_t^{Elc}$. Here it is worth noting that the objective function minimizes the electricity cost associated with the hourly volatile electricity prices in the wholesale electricity market. While, other electricity costs, such as global adjustment and peak demand payments would be paid as a percentage of the electricity bill [110].

3) Controlling the revenue deviation slack variable: $\alpha^{Adj,ER}\cdot\boldsymbol{R}_t^{Adj,Exp}$

4) Controlling the hydrogen price slack quantity: $\sum_{h\in\mathcal{H}}\alpha^{Adj,Prc}\cdot\boldsymbol{Prc}_{h,t}^{H_2,Adj}$.

The objective function is subject to the PtH constraints as follows:

$$F_h^{min}\le\boldsymbol{F}_{h,t}^{PtH}\le F_h^{max}\qquad\forall\, t\in\mathcal{T}\wedge\forall\, h\in\mathcal{H} \tag{6.6}$$

$$\boldsymbol{F}_{h,t}^{PtH}=\Pi^{PtH}\cdot\eta^{PtH}\cdot\boldsymbol{P}_{h,t}^{PtH}\quad\forall\, t\in\mathcal{T}\wedge\forall\, h\in\mathcal{H}, \tag{6.7}$$

where, (6.6) limits the operation of electrolyzer units to its minimum and maximum phys-

ical capacity, while (6.7) indicates the hydrogen production in m^3/h in terms of the consumed electric power by the electrolyzer.

The objective function is also subject to the hydrogen storage SOC balance equation:

$$\boldsymbol{SOC}_{h,t} = \boldsymbol{SOC}_{h,(t-1)} + (\boldsymbol{F}_{h,t}^{PtH} - F_{h,t}^{Dem} - \gamma^{Dsp} \cdot \boldsymbol{SOC_{h,t}}) \cdot \Delta t \quad \forall\, t \in \mathcal{T} \wedge \forall\, h \in \mathcal{H}, \tag{6.8}$$

where (6.8) ensures that the net energy into the storage reservoir at any given time step is equal to the available SOC plus the inflow of the generated hydrogen, while the hydrogen demand and the storage system dissipation are deducted.

The hydrogen storage is constrained based on its minimum and maximum capacity as expressed in (6.9)–(6.11) to meet the requirement for participation to the CBDR program.

$$SOC_{h,t}^{lb} \leq \boldsymbol{SOC}_{h,t} \leq SOC_h^{max} \quad \forall\, t \in \mathcal{T} \wedge \forall\, h \in \mathcal{H} \tag{6.9}$$

$$SOC_{h,t}^{lb} = SOC_h^{min} + SOC_t^{CBDR} - \boldsymbol{SOC}_{h,t}^{A,DR} \quad \forall\, t \in \mathcal{T} \wedge \forall\, h \in \mathcal{H} \tag{6.10}$$

$$0 \leq \boldsymbol{SOC}_{h,t}^{A,DR} \leq SOC_t^{CBDR} \quad \forall\, t \in \mathcal{T} \wedge \forall\, h \in \mathcal{H}, \tag{6.11}$$

where the DR slack variable in (6.10) allows the utilization of the contracted CBDR SOC, i.e., SOC_t^{CBDR} to respond to the DR signals. The CBDR SOC slack variable is separately assigned to each station and enables different contributions from each station to meet the CBDR requirement as a whole. While the contribution from each station is different, the aggregated SOC, $SOC_{h,t}^{lb}$, should satisfy the CBDR program requirement at each time step as formulated in the following constraint:

$$\begin{aligned} \sum_{h \in \mathcal{H}} SOC_h^{min} + \big(1 - Sgn(\boldsymbol{P}_t^{Sgl})\big) \cdot SOC_t^{CBDR} &\leq \sum_{h \in \mathcal{H}} \boldsymbol{SOC}_{h,t} \\ \leq \sum_{h \in \mathcal{H}} SOC_h^{max} \quad \forall t \in \mathcal{T} \wedge \forall h \in \mathcal{H}\ \forall \boldsymbol{P}_t^{Sgl} &\geq 0, \end{aligned} \tag{6.12}$$

where, $Sgn(\boldsymbol{P}_t^{Sgl})$ states the sign function of the DR signal at the time interval t, i.e.,

equals one if the signal has a non–zero value and equals zero if the signal is zero, pertaining no participation to the DR program is required. As expressed in (6.12), once the signal $Sgn(\boldsymbol{P}_t^{Sgl})$ is zero, the SOC lower bound would be boosted by the addition of the SOC_t^{CBDR}. Once the signal $Sgn(P_t^{Sgl})$ is non–zero, however, the SOC would be allowed to approach the minimum value so that the SOC_t^{CBDR} can be freed up to respond to the DR signal. In any case, the SOC is bounded by the maximum value as stated by (6.12). It should be noted that the issued DR signal aims to limit the total intake power of the fueling stations. The optimization constraint in (6.13) ensures that the optimization problem can act as per the DR signal, once the signal is issued.

$$\sum_{h\in\mathcal{H}} \boldsymbol{P}_{h,t}^{PtH} \leq Sgn(\boldsymbol{P}_t^{Sgl}) \cdot \boldsymbol{P}_t^{Sgl} + \big(1 - Sgn(\boldsymbol{P}_t^{Sgl})\big) \cdot \sum_{h\in\mathcal{H}} P_h^{max}$$
$$\forall\, t \in \mathcal{T} \wedge \forall\, h \in \mathcal{H} \wedge \forall\, \boldsymbol{P}_t^{Sgl} \geq 0; \tag{6.13}$$

equation (6.13) implies that the sum of the PtH intake power should not exceed the quantity of the DR signal ($\boldsymbol{P}_t^{Sgl}$). This is generally defined according to the executed contract between the market operator and the market participants who are willing to contribute to the DR program. As expressed by (6.13), once the signal is zero, the aggregated input power of the PtH units are limited to their maximum ratings stated by P_h^{max}, i.e., pertaining no limitation imposed by the electricity market operator. Once the signal is issued by the market operator (non–zero value for $Sgn(\boldsymbol{P}_t^{Sgl})$), the PtH units are scheduled accordingly to consume less power in order to serve the grid during peak periods. In such a case, the sign function of the DR signal changes to one; thus, (6.13) ensures that the aggregation of the PtH input power does not exceed the DR signal quantity. Equation (6.14) expresses the profitability constraint of the optimization problem, where it would adjust the hydrogen sale prices at each time interval to ensure that the expected revenue is achieved.

$$R^{Exp} - \boldsymbol{R}_t^{Adj,Exp} \leq \sum_{t\in\mathcal{T}^*}\Bigg\{\sum_{h\in\mathcal{H}}\left(\widehat{F}_{h,t}^{Dem}\cdot\widehat{\boldsymbol{Prc}}_{h,t}^{H_2} - \widehat{\boldsymbol{P}}_{h,t}^{PtH}\cdot\widehat{Prc}_t^{Elc} - C^{PtH}\cdot\widehat{\boldsymbol{F}}_{h,t}^{PtH}\right)\cdot\Delta t$$
$$+DR^{U,Prc}\cdot\widehat{\boldsymbol{P}}_t^{Sgl} + DR^{A,Prc}\cdot\frac{\widehat{\boldsymbol{SOC}}_t^{CBDR}}{\Pi^{PtH}\cdot\eta^{PtH}}\cdot DR^{Hr}\Bigg\}\forall t\in\mathcal{T}. \tag{6.14}$$

As such, the quantities of (6.14) over a set of time steps in $\mathcal{T}^*$ include several historical and look–ahead values that would contribute to the revenue calculation. These quantities are distinguished from the original optimization variables/parameters by $\widehat{\ }$ as expressed in (6.14). It is noteworthy that the historical revenue data are stemmed from the actual operation in the previous scheduling hours, where at each time step, the algorithm directly adds both the historical and look–ahead revenue data with the same weighting factor. This ensures that the long–term expected profit is met without experiencing a high volatility in hydrogen prices in order to achieve the expected revenue at every optimization cycle. The adopted methodology for the computation of the revenue, however, would ensure that the longer–term profitability of the system is met instead of meeting the targeted revenue at each optimization cycle. The generated revenue is set to equal or exceed the expected revenue, i.e., R^{Exp}, where the slack variable is bounded in the following (i.e., $\boldsymbol{R}_t^{Adj,Exp}$ allows the expected revenue to be deviated to a certain extent as needed):

$$0 \leq \boldsymbol{R}_t^{Adj,Exp} \leq R^{Dev} \qquad \forall\, t\in\mathcal{T}. \tag{6.15}$$

The revenue deviation in (6.15) would prevent the infeasibility of the optimization problem by creating a soft profitability constraint, where the expected revenue cannot be achieved temporarily. The future operation would compensate for the loss of revenue if the revenue is deviated from the expected value in one cycle. The slack variable $\boldsymbol{R}_t^{Adj,Exp}$ is penalized in the objective function so that the revenue is not deviated from the expected

value unless this is needed for the convergence of the optimization problem. While the hydrogen price is defined as a variable in the formulated optimization problem, it is bounded by the model based on the hydrogen price margin in the market. Thus, the hydrogen price does not arbitrarily increase to generate a higher profit. As such, the objective function given in (6.5) is also subject to the hydrogen price constraints as follows:

$$\boldsymbol{Prc}_{h,t}^{H_2} = Prc_h^{H_2,min} + \boldsymbol{Prc}_{h,t}^{H_2,Adj} \quad \forall\, t \in \mathcal{T} \wedge \forall\, h \in \mathcal{H} \tag{6.16}$$

$$0 \leq \boldsymbol{Prc}_{h,t}^{H_2,Adj} \leq \beta_{h,t}^{Adj,Prc} \cdot Prc_h^{H_2,min} \quad \forall\, t \in \mathcal{T} \wedge \forall\, h \in \mathcal{H}. \tag{6.17}$$

Equation (6.16) states that the hydrogen price can increase from a predefined minimum value up to a certain limit adjusted by another variable, i.e., $\boldsymbol{Prc}_{h,t}^{H_2,Adj}$. The adjusting variable can be anywhere between zero and a certain factor of the minimum price as stated by (6.17). The slack variable $\boldsymbol{Prc}_{h,t}^{H_2,Adj}$ is penalized in the objective function to prevent price increases unless it is required to meet the expected revenue. It is noted that while both slack variables $\boldsymbol{R}_t^{Adj,Exp}$ and $\boldsymbol{Prc}_{h,t}^{H_2,Adj}$ are penalized in the objective function, the penalty factor for the former is larger, and both penalty factors are higher than the electricity prices to prioritize generating the expected profit versus offering a lower sale price to FCEVs. Such a requirement is met by the following constraint:

$$\alpha^{Adj,ER} >> \alpha^{Adj,Prc} >> Prc_t^{Elc} \quad \forall\, t \in \mathcal{T}. \tag{6.18}$$

The objective function is also subject to the set of power flow and voltage constraints as stated in the following:

$$\boldsymbol{P}_{n,t} \leq P_n^{max} \quad \forall\, t \in \mathcal{T} \wedge \forall\, n \in \mathcal{N} \tag{6.19}$$

$$V_n^{min} \leq \boldsymbol{V}_{n,t} \leq V_n^{max} \quad \forall\, t \in \mathcal{T} \wedge \forall\, n \in \mathcal{N}. \tag{6.20}$$

The active and reactive power injected in the system at each node n are stated as:

$$\boldsymbol{P}_{n,t} = |\boldsymbol{V}_{n,t}| \sum_{n' \in \mathcal{N}} \Big[|\boldsymbol{V}_{n',t}| \cdot |Y_{nn'}| \times Cos\big(\boldsymbol{\delta}_n - \boldsymbol{\delta}_{n'} - \theta_{nn'}\big) \Big] \; \forall\, t \in \mathcal{T} \wedge \forall\, n \in \mathcal{N} \wedge \forall\, h \in \mathcal{H} \quad (6.21)$$

$$\boldsymbol{Q}_{n,t} = |\boldsymbol{V}_{n,t}| \sum_{n' \in \mathcal{N}} \Big[|\boldsymbol{V}_{n',t}| \cdot |Y_{nn'}| \times Sin\big(\boldsymbol{\delta}_n - \boldsymbol{\delta}_{n'} - \theta_{nn'}\big) \Big] \; \forall\, t \in \mathcal{T} \wedge \forall\, n \in \mathcal{N} \wedge \forall\, h \in \mathcal{H}. \quad (6.22)$$

The active and reactive power balance constraints in the power grid are stated by (6.23) and (6.24); in which $x(n)$ equals one for buses to which a fueling station is connected.

$$\Delta P_{n,t} = \boldsymbol{P}^{Gen}_{n,t} - P^{Dem}_{n,t} - x(n) \cdot \boldsymbol{P}^{PtH}_{h,t} - \boldsymbol{P}_{n,t} \qquad \forall\, t \in \mathcal{T} \wedge \forall\, n \in \mathcal{N} \wedge \forall\, h \in \mathcal{H} \quad (6.23)$$

$$\Delta Q_{n,t} = \boldsymbol{Q}^{Gen}_{n,t} - Q^{Dem}_{n,t} - x(n) \cdot \boldsymbol{Q}^{PtH}_{h,t} - \boldsymbol{Q}_{n,t} \qquad \forall\, t \in \mathcal{T} \wedge \forall\, n \in \mathcal{N} \wedge \forall\, h \in \mathcal{H}. \quad (6.24)$$

6.4 Numerical Illustration

Fig. 6.4 shows the 33–bus power distribution system [98, 109] adopted to numerically evaluate the proposed algorithm. As shown in the figure, the power system is integrated with a mix of wind and solar generation, in addition to the distributed hydrogen fueling stations. Each hydrogen fuel station is comprised of an electrolyzer and a hydrogen storage unit. The modeling and simulation parameters for the stations are adopted from the literature [89, 144], as listed in Table 6.2. Fig. 6.5 shows the hydrogen demand profile of the transit sector at each fueling station. As shown in the figure, each station is assumed to have a different consumption pattern depending on the demand requirement at that station. The figure also shows that the demand varies from the minimum during night time to the maximum during day time.

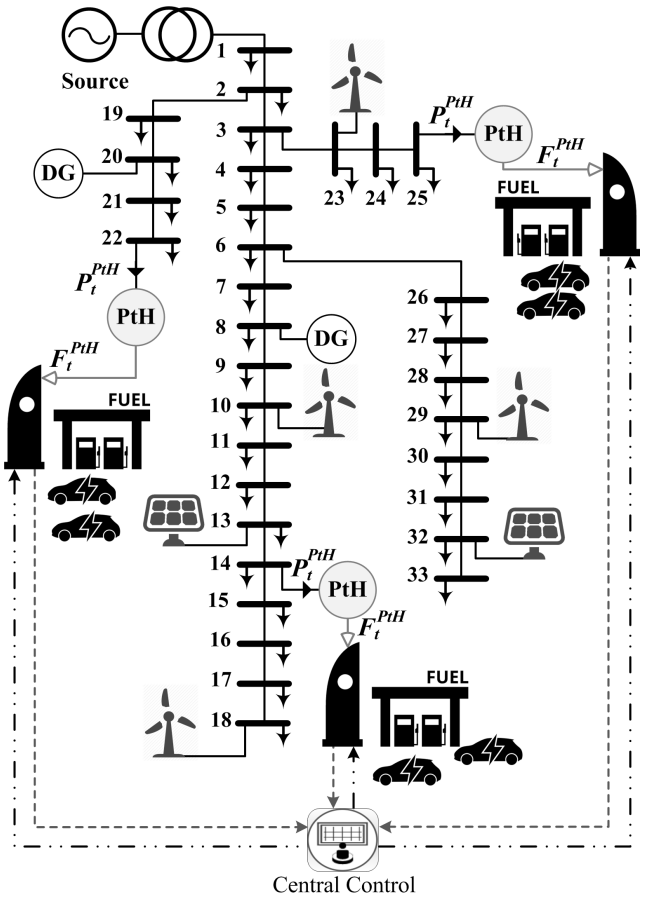

Figure 6.4: 33–bus power distribution test system with high penetration of renewable generation, integrated with hydrogen fueling stations.

Table 6.2: Modeling and Simulation Parameters

$F_h^{max} = 430$ (m^3/h)	$F_h^{min} = 0$
$SOC_h^{max} = 5000$ (m^3)	$SOC_h^{min} = 10\% \times SOC_h^{max}$
$\Pi^{PtH} = 360$ (m^3/MWh)	$\eta^{PtH} = 60\%$
$\gamma^{Dsp} = 0.006\% \times SOC_{h,t}$	$P_n^{max} = 10$ (MW)
$V_n^{max} = 1.05$ (pu)	$V_n^{min} = 0.95$ (pu)
Total CAPEX = \$2.5 Million	LS = 15 (Year)
$C^{PtH} = 3\% \times \$2.5\text{M}/(F_h^{max} \times 8760)$	$SOC_t^{CBDR} = 20\% \times SOC_h^{max}$
$DR^{A,Prc} = 30$ (\$/h)	$DR^{U,Prc} = 30$ (\$/MW)
$Prc_h^{H_2,min} = 0.25$ (\$/m^3)	$\beta^{Adj,Prc} = 2$
$R^{Exp} = 13\% \times$ CAPEX	$R^{Dev} = 3\% \times$ CAPEX

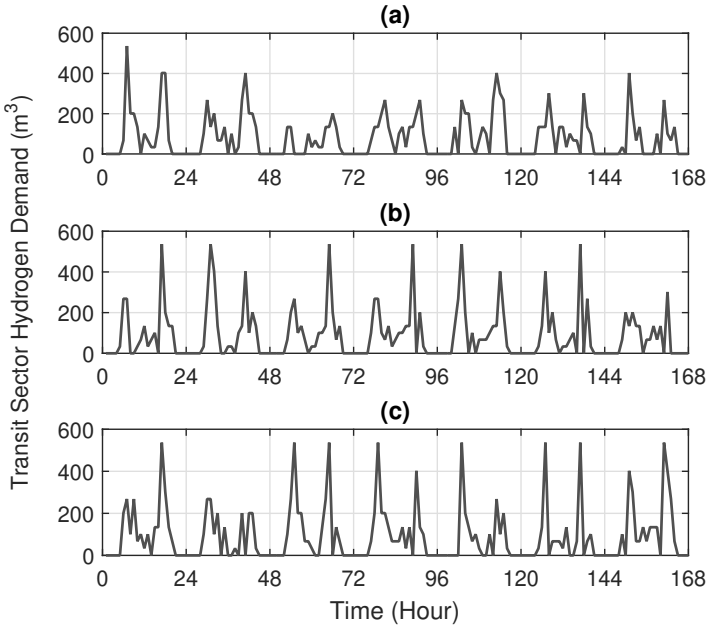

Figure 6.5: Hydrogen demand by the transit sector at (a) Station 1, (b) Station 2, and (c) Station 3.

The ratings for the electrolyzer and hydrogen storage units are selected based on the transportation demand and the requirement to participate to the CBDR program. For simulation purposes, it is assumed that the distributed hydrogen stations have different demand profiles. It should also be noted that while the expected revenue R^{Exp} in (6.14) could vary depending on the project risk profile, it is assumed to be 13% of the CAPEX for the numerical studies [145] in this section. In any case, considering different values for the expected revenue would not change the proposed concepts and the ultimate comparative study.

The formulated model in Section 6.3 is categorized as a nonlinear optimization problem and is solved using a combined Interior Point nonlinear programming and Newton Trust Region solution mechanism. It should be noted that while the optimization formulation is general in this research work, the optimization horizon is considered as 3 hours with 1–hour time interval in the numerical studies [146]. The look–ahead optimization problem

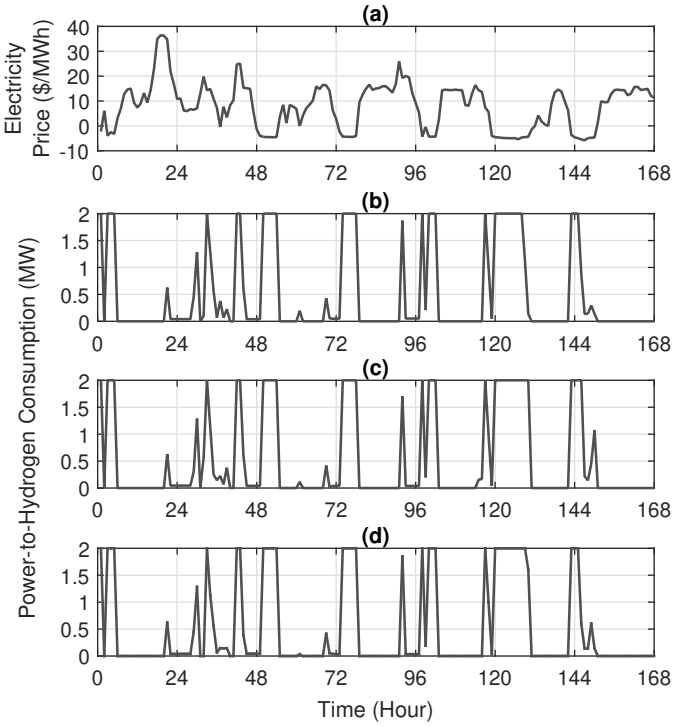

Figure 6.6: (a) Electricity market prices; operational setpoints of hydrogen fuel stations at: (b) Station 1, (c) Station 2, and (d) Station 3.

decides the scheduling setpoints for the next T hours based on the demand forecast for the same hours. Thus, storage will be prepared accordingly for the upcoming demand by the transportation sector. The proposed algorithm is coded and simulated in the MATLAB environment. The optimization algorithm is run in a PC with the following specifications: Core i7-6700, 3.4 GHz CPU, 16 GB RAM, and 64 bits system. The convergence tolerance and the maximum number of iterations are set to 10^{-6} and 500, respectively. It is found that the average execution time is around 10 seconds which would be suitable for the hourly scheduling model.

6.4.1 Operational Scheduling of Hydrogen Storage Stations

Fig. 6.6 shows the optimal scheduling setpoints of the hydrogen fueling stations at a given week out of the studied year. As depicted in the figure, PtH units operate at negative/lower

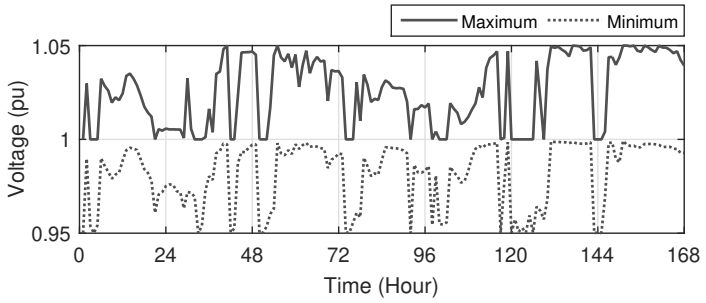

Figure 6.7: Minimum and maximum voltages in the power system.

market prices to reduce the power purchase cost and maximize the system profit. The operational setpoints are also impacted by the hydrogen demand at each station, hence they vary at different stations. Fig. 6.7 shows the system–wide minimum and maximum bus voltages in the test system; i.e., the maximum/minimum voltages in the entire system at each time interval. If system–wide voltages are within the allowable limits at each time interval, the operation of the entire system would be acceptable. As shown in Fig. 6.7, the optimization algorithm ensures that the system voltages are maintained within the acceptable limits, according to the ANSI code [136].

Fig. 6.8 (a) shows the DR signal issued by the market to the central controller of the hydrogen stations. The minimum allowed SOC, offered CBDR SOC, and the actual SOC are shown in Figs. 6.8 (b)–(d). It can be observed that the SOC at each station varies according to the local hydrogen demand by the transportation sector at the station. In addition, the CBDR capacity offered to the market is not utilized unless the DR signal is issued; this is to ensure that storage remains ready to follow the signal; i.e., actual SOC stays above the CBDR capacity. Once the signal is issued, however, the CBDR capacity is released so that the signal can be followed without affecting the supply to the transportation sector; this can be observed from the figure where the SOC crosses the DR capacity border once the signal is not zero. In such a case, each station would respond differently to the signal depending on the optimal setpoints decided by the optimization problem. Fig. 6.8 (e) shows the aggregated SOC of all the stations as a whole, which is

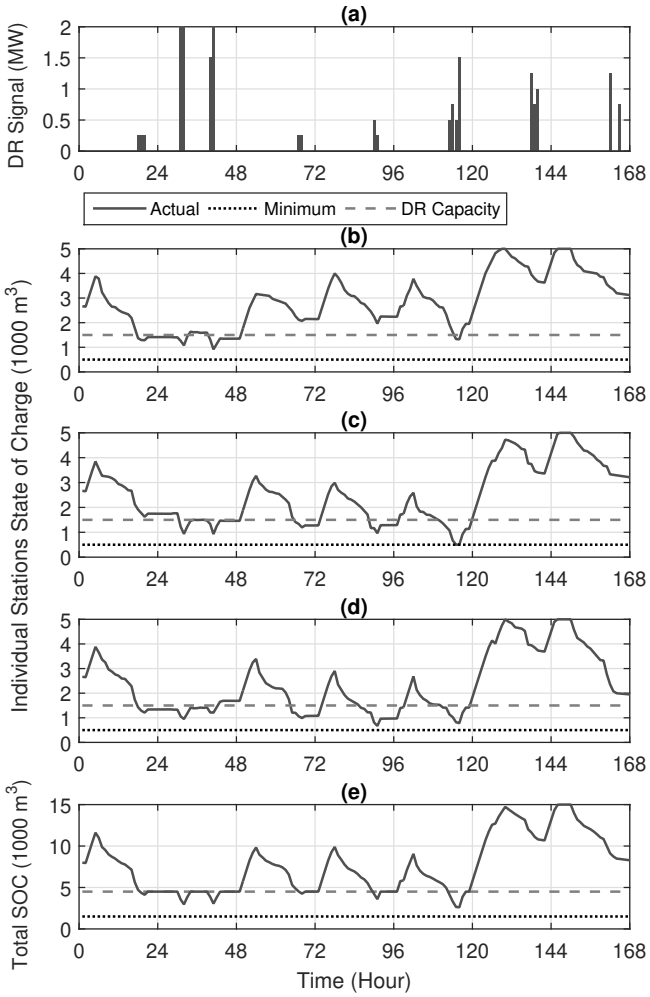

Figure 6.8: (a) Electricity market CBDR signal; hydrogen stations SOC at: (b) Station 1, (c) Station 2, (d) Station 3; (e) aggregated SOC

offered to the CBDR market. The stations operator receives both the availability payment (via CBDR SOC) and the utilization payment (via operation as per the signal quantity).

The hydrogen sale prices for each station are also decided by the optimization problem, as shown in Fig. 6.9, when the stations participate to the CBDR program. While the market prices are different at various hours, the average values are found to be 0.326, 0.321, and 0.323 $\$/m^3$ for Stations 1, 2 and 3, respectively. These prices are decided so that the stations can achieve the expected revenue as per the constraint stated in (6.14). While different hydrogen sale prices are decided by the stations depending on the local

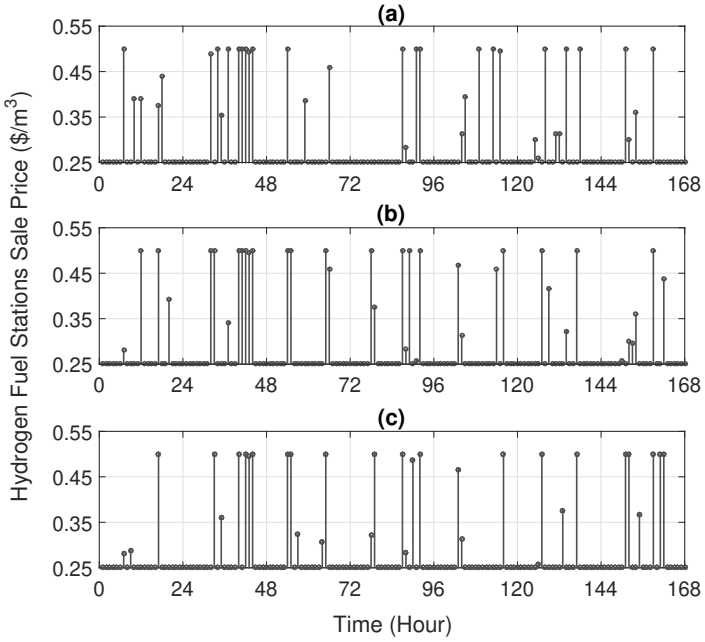

Figure 6.9: Hydrogen sale prices with contribution to CBDR program at: (a) Station 1, (b) Station 2, and (c) Station 3.

hydrogen demand, they all work as a whole to achieve the expected revenue.

Fig. 6.10 shows the sale prices when the stations do not participate to the CBDR program, but the same level of revenue is expected. It can be observed that the prices tend to be higher in this case to compensate for the lack of revenue that would have been achieved via the DR program. The average hydrogen prices for the three stations are found to be 0.398, 0.384, and 0.386 $\$/m^3$, respectively. Hence, the participation to the CBDR program leads to an average reduction of the hydrogen sale prices of 20.7%. Thus, via participation to the CBDR program, lower hydrogen prices can be offered to the transportation sector, thereby becoming more competitive in the market without compromising the expected revenue. The revenue of hydrogen fuel stations for the studied week is found to be \$18.4k, i.e., 12.8% of the stations CAPEX (i.e.,\$ 7.5 M).

The generated revenue is a key factor in every investment, and it has an expected value that should be met. The hydrogen sale price is a variable in the model that is dynamically

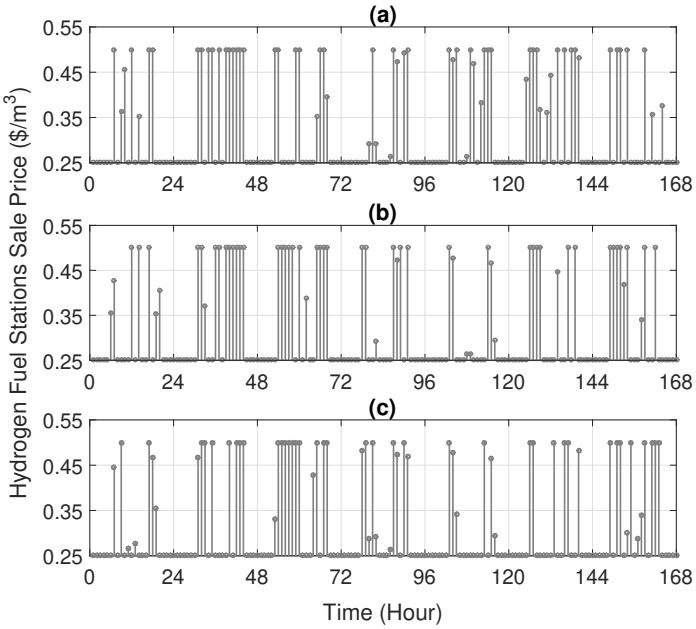

Figure 6.10: Hydrogen sale prices without contribution to CBDR program at: (a) Station 1, (b) Station 2, and (c) Station 3.

adjusted so that the expected revenue could be achieved. The model also profits from contribution to the CBDR program. Therefore, the higher the CBDR prices are, the lower the hydrogen sale prices will be at a given expected revenue value. In such a case, the impact of the CBDR price on the hydrogen sale prices is worth investigating. Accordingly, the required hydrogen sale prices to achieve the expected revenue of 13% are determined at different prices for the CBDR contribution, and the results are given in Fig. 6.11. As expected, the hydrogen sale prices decrease as the CBDR price goes higher at a given value for the expected revenue (i.e., 13% of the initial investment per year). This is because the CBDR revenue increases with the increase of its price and, thus, a lower hydrogen price occurs.

Another factor that could change depending on the project risk profile is the expected revenue. The hydrogen sale prices by the fueling stations are considerably sensitive to the expected revenue. Accordingly, the required hydrogen sale prices at different values of the expected revenue are computed while the price for the CBDR is considered constant in this

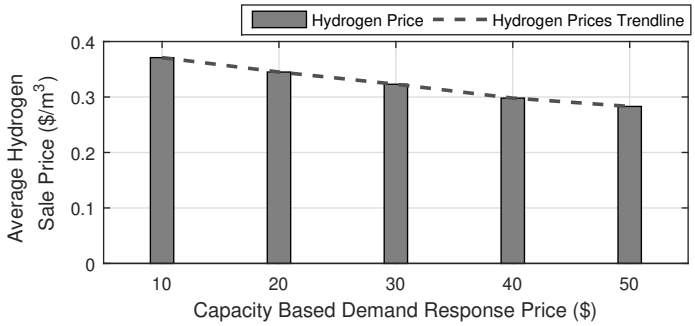

Figure 6.11: Average hydrogen sale price at different CBDR prices.

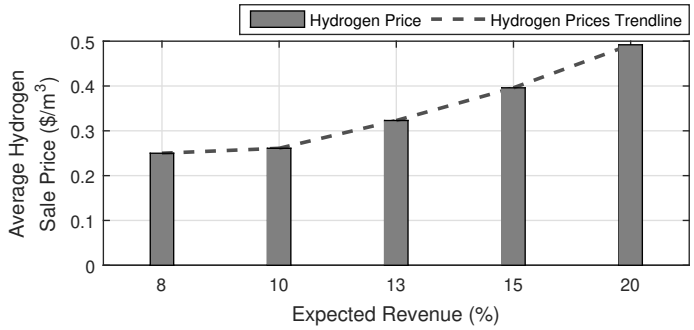

Figure 6.12: Average hydrogen sale price at different expected revenue values.

case; the results are shown in Fig. 6.12. As depicted, the average value of hydrogen sale prices changes from 0.25 to 0.49 $\$/m^3$ at the expected revenue of 8% and 20%, respectively.

6.4.2 Comparative Study: Hydrogen vs BEV Stations Revenue

A comparative economic study for different operational scenarios of the hydrogen and BEV charging stations is conducted in this section. Four cases are contemplated as follows:

Case 1: Hydrogen stations with participation to CBDR.

Case 2: BEV stations with participation to CBDR.

Case 3: Hydrogen stations without participation to CBDR.

Case 4: BEV stations without participation to CBDR.

In order to fairly compare the cases, it is assumed that the total energy supply in all cases are equal; i.e., the same mileage would be achieved for the transportation sector in all cases, where the BEVs charging demand is calculated as follows:

$$P_{h,t}^{BEV,Dem} = F_{h,t}^{Dem} \cdot E_{H_2}^{Den} \cdot \frac{1}{l_{H_2}} \cdot l_{BEV} \cdot \frac{1}{E_{elec}^{Den}} \quad \forall\, t \in \mathcal{T} \wedge \forall\, h \in \boldsymbol{\mathcal{H}}. \tag{6.23}$$

In (6.23), $P_{h,t}^{BEV,Dem}$, l_{BEV}, and E_{elec}^{Den} represent the BEVs charging demand, energy consumption of 1.11 Mj/km (i.e., equivalent to 0.31 kWh/km), and electric energy density of 3600 Mj/MWh, respectively [147]. In addition, l_{H_2} and $E_{H_2}^{Den}$ state the FCEV energy consumption of 0.94 Mj/km (i.e., equivalent to 0.094 m^3/km), where the hydrogen energy density is considered as 10 Mj/m^3, respectively [147]. It is noteworthy that the BEVs charging stations are sized to have the same CAPEX as the hydrogen fueling stations. While the initial investment is contemplated in the comparative studies, the land cost for both cases are ignored. Accordingly, the storage capacity of the stations and the power inverters are sized to be 5 MWh and 2 MW, respectively. In addition, the operating cost of the BEVs charging stations (C^{BEV}) is considered to be 60% of the hourly maintenance cost (i.e., 5% of CAPEX) at the maximum inverter rate. The energy sale prices for all cases were set based on the average retail prices in the market; i.e., 0.5 \$/m^3 for the hydrogen [89] and 145 \$/MWh for electricity [148].

Under the above–mentioned assumptions, the accumulated revenue of the fueling/charging stations for all cases is computed. It is emphasized that the revenue is calculated under the fixed hydrogen/electricity pricing with the values mentioned above. Fig. 6.13 presents the hourly revenue for the hydrogen and BEV charging stations both with participation to the CBDR program, i.e., Cases 1 and 2. As shown in the figure, the hourly revenue is volatile under both cases. The revenue has a positive peak once hydrogen is sold to the transportation sector. In addition, the generated revenue temporarily moves below zero once the stations pay for the power purchase. The figure also shows that the revenue of the

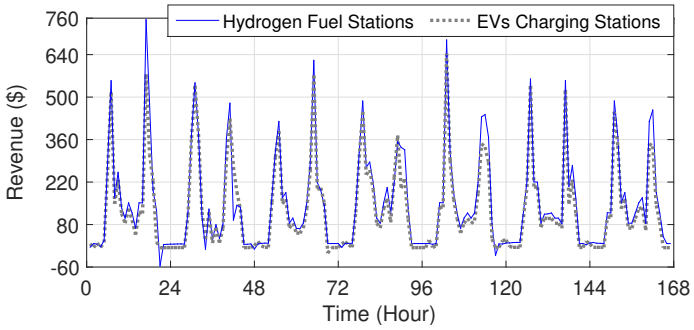

Figure 6.13: Comparative hourly revenue of hydrogen and BEV stations with participation to CBDR program.

Table 6.3: Comparative Energy Consumption

	Station 1	Station 2	Station 3	Total
FCEVs H2 Stations (Mj)	$2.98e^5$	$3.16e^5$	$3.02e^5$	$9.165e^5$
BEVs Charging Stations (Mj)	$2.03e^5$	$2.21e^5$	$2.22e^5$	$6.465e^5$

hydrogen stations is slightly higher than that of the BEV charging stations. This mainly stems from the fact that hydrogen is all together a more expensive form of energy in the market than electricity. As such, it is sold with a higher price as compared to the electricity. It is worth noting that the hydrogen stations reveal a higher energy consumption rate compared to the BEVs stations. This can be observed from the results in Table 6.3. The values in the table are achieved under the same mileage range for the vehicles (i.e., FCEVs and BEVs).

In order to compare the economic values of all cases, the annual revenue, Net Present Value (NPV), Internal Rate of Return (IRR), and the profitability of the investments are computed for the above–mentioned cases and reported in Table 6.4 by using a discount rate of 2.5%. The system profitability considers the initial cost and expected rate of return, and is calculated as a ratio between the annual revenue to the expected rate of return plus the normalized CAPEX over the lifespan of the facility [149]. As indicated in the

Table 6.4: Comparative Revenue and Profitability Values

	Hydrogen Fuel Station		BEV Charging Station	
	With CBDR	Without CBDR	With CBDR	Without CBDR
Annual Revenue (M$)	1.3	1.126	1.124	1.074
Profitability (%)	88.14	76.34	76.2	72.81
NPV (M$)	8.595	6.561	6.416	5.797
IRR (%)	15.28	12.5	12.4	11.54

table, hydrogen fueling stations offer a higher investment desirability. This is because the NPV and IRR of hydrogen stations are higher than the ones for BEV stations. Besides, the participation to the CBDR program enhances the NPV and IRR of the project for both the hydrogen fuel stations and BEVs stations. It is worth noting that the hydrogen stations are more profitable than BEV stations due to higher hydrogen sale prices. The following outcomes can be drawn from the results indicated in Table 6.4:

- The highest value of revenue is achieved for the hydrogen stations when they participate to the CBDR program. The higher revenue is resulted from the stacked benefit from the electricity market and the hydrogen sale to the transportation sector. For a similar reason, the revenue for the BEV charging stations is boosted once they participate to the CBDR program.
- The revenue of hydrogen stations is higher than that of the BEV stations under no contribution to the CBDR program. As mentioned above, this is stemmed from the fact that hydrogen in today's market is a more expensive product than the electricity.

In order to investigate the ability of the hydrogen and BEVs stations to achieve the expected profit, the profitability of investment needs to be determined. While the expected profit could vary for different projects, it is assumed to be 13% of the CAPEX per year plus the CAPEX value exhausted over the plant lifespan [145]. With the CAPEX and

plant lifespan reported in Table 6.2, the rate of return of \$1.475 M per year is expected in order for the plant to be considered profitable. Under the revenue values acquired for all cases, the profitability of the plant is computed for all cases and reported in Table 6.4. The results indicate that the generated revenue is not yet enough to meet the expected profit under either of the cases; however, a higher profitability level is resulted for hydrogen stations with participation to the CBDR program. This would intensify the fact that the stations should be utilized for as many ancillary services as possible in order to become profitable. It should also be noted that as the technology grows, the CAPEX for the stations is expected to shrink; thus, there would be a higher opportunity for the stations to return the expected revenue in the near future.

6.5 Discussion and Summary

This chapter proposes a model for the central scheduling of distributed electrolyzer–based hydrogen fueling stations. The proposed model aims at (i) utilizing the lower/negative electricity prices towards hydrogen generation, and (ii) optimizing the operation of the hydrogen stations, in order to increase the profitability of investment. Profitability constraints and dynamic hydrogen pricing mechanisms are contemplated in the model to achieve the expected profit though adjusting hydrogen sale prices. The model is numerically evaluated on a power distribution test system that supplies power to the distributed hydrogen storage stations. Numerical studies indicate that the system profit is considerably intensified once fueling stations participate to the CBDR program under the proposed model. The model would, thus, bring about new opportunities for the investment in distributed hydrogen stations.

Comparative studies are conducted in order to assess the economic viability of the investment in storage–based hydrogen fueling stations versus BEV charging stations. The study reveals that the investment in hydrogen fueling stations can result in a higher profit.

On the other hand, higher hydrogen fuel costs may actually be a reason for drivers to prefer BEVs over FCEVs. The results also indicate that the generated revenue is not yet enough to equal the expected rate of return under either of the cases. However, participation to the CBDR program enhances the generated profit. As the emerging technology materializes, the CAPEX of hydrogen stations is expected to shrink; thus, there would be more opportunities for the hydrogen fueling station to yield the expected revenue in the near future.

Chapter 7
Optimal Sizing and Scheduling of LOHC–Based Generation and Storage Plants

7.1 Introduction

LOHC technology now offers a promising solution for the reliable and safe storage of hydrogen. In this regard, this chapter demonstrates how LOHC–based hydrogen generation and storage plants should be sized and operated for joint applications, in order to enhance the system rate of return. Since the LOHC reservoir is significantly inexpensive compared to the generation plant and does not occupy a large space due to the LOHC higher energy density, the reservoir can be readily expanded to realize longer–term energy storage, e.g., weekly, monthly, or seasonal. A larger storage reservoir with massive amount of energy also allows for disaggregation of electrolyzer and storage capacity to provide multiple services to the transportation sector and power grid; the operating setpoints of the electrolyzer can be optimally scheduled to provide a combination of ancillary services to the market. The stacked profit yielded from multiple sources can alleviate the gap between the current and

the expected rate of return. As such, LOHC–based generation and storage plants can be optimally sized and operated for joint applications to serve both the transportation sector and ancillary services market.

Ancillary services provision to the grid has been identified as a win–win situation to the utility grid and the customers. On one hand, ancillary services allow the grid operator to be able to maintain the grid's normal conditions, i.e., Reactive Power (VAR) control for keeping the voltage within the limits and balancing out the generation and demand [150, 151], and DR for balancing the demand and generation in the grid [152]. On the other hand, ancillary services contributors are incentivized due to their participation to the market, thereby obtaining a higher rate of return level [6].

Here it is worth noting that, some of the electricity system operators do not have a specific energy conservation program that compensate for the VAR support. However, other electricity system operators such as Midcontinent Independent System Operator (MISO) in the Midwest United States and the Canadian province of Manitoba, and the independent electricity system operator in Ontario provide a compensation for the reactive power resource owner for its voltage control capability [150, 153]. Hence, in this work VAR support is adopted as an ancillary service that would be compensated based on its capability to follow the received VAR ancillary service signal.

To fill the gap between the existing studies and an industry–level model, this work shows how the LOHC–based generation and storage plants should be sized and operated for joint applications in order to enhance the system rate of return. This research work is the first of its kind to size and schedule the centralized LOHC–based generation and storage plants for concurrent services to the transportation sector and ancillary services market. In particular, this chapter presents the following contributions:

1) A new algorithm is developed for optimal sizing of LOHC–based generation and storage plants. The proposed algorithm is based on maximizing the system net profit

under various operating scenarios. The generation and storage plants are optimally sized considering the operation of the facility for multiple services to the transportation system and ancillary services market.

2) A new optimal scheduling model is presented for the LOHC–based generation and storage plants that would (i) exploit the lower electricity market prices considering the transportation demand, (ii) follow the ancillary service signals through the incorporation of slack variables into the model, and (iii) allow the seasonal storage in order to maximize the system profit.

3) The SOC in the storage plant is adaptively adjusted by the proposed scheduling model for each service in order to further enhance the system net profit. The adaption of the storage reserved capacity involves optimal scheduling for allocating and manging the required reserve for each ancillary service.

To that end, Table 7.1 presents the definition of indices, sets, constant, time–dependent parameters, proposed model sizing variables, and proposed model scheduling variables in this chapter.

Table 7.1: Chapter 7 Nomenclature

A. Indices

t	Index of time steps.
b	Index of power network buses.
s	Index of Monte Carlo scenarios.

B. Sets

T	Set of optimization problem time steps.
B	Set of buses in power transmission system.
S	Set of Monte Carlo simulation.

C. Constants

Δt	Time interval of the optimization problem (h).
$V_{b,min}$	Minimum voltage magnitude at Bus b (pu).
$V_{b,max}$	Maximum voltage magnitude at Bus b (pu).
$P_{b,max}$	Maximum power at Bus b (MW).
$Y_{bb'}$	Admittance magnitude from Bus b to b' (pu).
$\theta_{bb'}$	Admittance angle from Bus b to b' (Rad).

Table 7.1: Chapter 7 Nomenclature ... continued

η^{Elz} Efficiency of the electrolyzer unit (%).

η^{H^+} Efficiency of the LOHC hydrogenation unit (%).

η^{H^-} Efficiency of LOHC dehydrogenation unit (%).

Γ^{Elz} Electrolyzer conversion factor ($m^3_{H_2}$/MWh).

Γ^{H^+} Hydrogenation consumption factor (MWh/$m^3_{H_2}$).

Γ^{H^-} Dehydrogenation consumption factor (MWh/m^3_{LH}).

ξ^{LH} LOHC volumetric storage density (m^3_{LH}/$m^3_{H_2}$).

ω^{H^+} Hydrogenation heat production factor (kWh/$m^3_{H_2}$).

ω^{H^-} Dehydrogenation heat demand factor (kWh/$m^3_{H_2}$).

γ^{Dsp} LOHC storage energy dissipation rate (%/h).

C^{Elz} Electrolyzer capital cost ($/MW).

C^{Con} Converter capital cost ($/MVA).

C^{H^+} Hydrogenation unit capital cost ($.h/$m^3_{H_2}$).

C^{Sto} LOHC storage unit capital cost ($/$m^3_{LH}$).

OC^{Elz} Electrolyzer operating cost ($/MWh).

OC^{H^+} LOHC hydrogenation operating cost ($/$m^3_{H_2}$).

OC^{Sto} LOHC storage unit operating cost ($/$m^3_{LH}$.h).

LH^{Prc} LOHC–based fuel price ($/$m^3_{LH}$).

VAR^{Prc} Reactive power (denoted by VAR) ancillary service price ($/MVAr.h).

DR^{Prc} DR ancillary service price ($/MWh).

$E^{A,Prc}$ Average electricity price for annual operating hours ($/MWh).

E^{BE} Maximum Electricity price during operation ($/MWh).

OH Annual operating hours (h).

H^{VAR} VAR ancillary service hours per day (h).

H^{DR} DR ancillary service hours per day (h).

β^{VAR} Penalty factor for VAR ancillary service ($/MVAr.h).

β^{DR} Penalty factor for DR ancillary service ($/MWh).

ρ^{Rew} Generation reward factor.

F^{Elz}_{min} Minimum outflow capacity of electrolyzer ($m^3_{H_2}$/h).

SOC^{LH}_{min} Minimum capacity of LOHC storage (m^3_{LH}).

D. Time–Dependent Parameters

E^{Prc}_t Electricity price at time t ($/MWh).

$F^{LH}_{t,Dem}$ LOHC demand by transportation sector (m^3_{LH}/h).

Q^{VAR}_t VAR ancillary service signal (MVAr).

P^{DR}_t DR ancillary service signal (MW).

E. Sizing Variables

P^{Elz}_{max} Electrolyzer rated power (MW).

S^{Con}_{max} Rated power of electrolyzer converter (MVA).

F^{Elz}_{max} Maximum hydrogen outflow of electrolyzer ($m^3_{H_2}$/h).

Table 7.1: Chapter 7 Nomenclature ... continued

F. Scheduling Variables

Q_{max}^{Con} Maximum VAR of electrolyzer converter (MVAr).

SOC_{max}^{LH} Maximum capacity of LOHC storage (m^3_{LH}).

SOC^{VAR} VAR SOC reserve margin (m^3_{LH}).

SOC^{DR} DR SOC reserve margin (m^3_{LH}).

P_{min}^{DR} Minimum value of DR signal (MW).

Λ_t Operation state of LOHC facility.

λ^{DR} Limitation factor for DR service (%).

λ^{VAR} Limitation factor for VAR service (%).

P_t^{Elz} Electrolyzer unit input power (MW).

F_t^{Elz} Electrolyzer unit hydrogen outflow ($m^3_{H_2}$/h).

$P_t^{H^+}$ Hydrogenation unit power consumption (MW).

$F_t^{H^+}$ Hydrogenation unit LOHC outflow (m^3_{LH}/h).

$P_t^{H^-}$ Dehydrogenation unit power consumption (MW).

$F_t^{H^-}$ Dehydrogenation unit LOHC inflow (m^3_{LH}/h).

$F_t^{H_2}$ Dehydrogenation unit hydrogen outflow ($m^3_{H_2}$/h).

$\Delta H_t^{H^+}$ Hydrogenation heat power release (kW).

$\Delta H_t^{H^-}$ Dehydrogenation heat power requirement (kW).

SOC_t^{LH} SOC of LOHC storage unit (m^3_{LH}).

Q_t^{Con} Converter reactive power generation (MVAr).

Q_t^{VARM} Slack variable for VAR signal management (MVAr).

$Q_t^{VARM'}$ Slack variable for VAR signal management (MVAr).

P_t^{DRM} Slack variable for DR signal management (MW).

$\delta_{b,t}$ Voltage angle at Bus b (Rad).

$V_{b,t}$ Voltage magnitude at Bus b (pu).

$P_{b,t}$ Active power at Bus b (MW).

$Q_{b,t}$ Reactive power at Bus b (MVAr).

7.2 Problem Statement

The LOHC–based technology is considered as a promising solution to promote the proliferation of hydrogen fueling stations, thereby leading to the deployment of hydrogen–powered vehicles. In this regard, the merits of the LOHC technology needs to be economically justified. In what follows, the overall structure of the LOHC–based systems including the electrolyzer, hydrogenation plant, and storage units as well as the supply chain for the

Figure 7.1: LOHC generation, storage, and supply chain for transportation electrification.

transportation sector is explained. Then, the proposed algorithm for sizing and scheduling of the generation and storage systems is presented.

As shown in Fig. 7.1, hydrogen is produced using an electrolyzer that diffuses the water molecules into oxygen and hydrogen. The steady state relationship between the generated hydrogen and the electrolyzer power is given as a function of the electrolyzer power to hydrogen conversion factor (i.e., Γ^{Elz}= 360 $m^3_{H_2}$/MWh) and efficiency (i.e., η^{Elz}= 60%) as follows [6], [104]:

$$F_t^{Elz} = P_t^{Elz} \cdot \Gamma^{Elz} \cdot \eta^{Elz} \qquad \forall\, t \in T. \tag{7.1}$$

Then, the generated hydrogen is fed into the LOHC–based hydrogenation reactor that would chemically bound the hydrogen gas with the organic carrier. The hydrogenation reactor requires electric energy to produce LOHC, while the hydrogenation process is exothermal that produce heat as a bi–product [104]. Equation (7.2) presents the steady state outflow of the LOHC from the hydrogenation unit as a function of the hydrogen to LOHC conversion factor (i.e., η^{LH}= 1/630 $m^3_{LH}/m^3_{H_2}$) and the hydrogenation unit efficiency of η^{H^+}= 97% [104]. Equation (7.3) shows the required power by the hydrogenation system (i.e., Γ^{H^+}= 0.031 kWh/$m^3_{H_2}$) [104]. Besides, (7.4) states the exothermal heat as a function of the hydrogen inflow to the hydrogenation unit and the hydrogenation process heat production factor (i.e., ω^{H^+}= 0.75 kWh/$m^3_{H_2}$) [104].

$$F_t^{H^+} = F_t^{Elz} \cdot \xi^{LH} \cdot \eta^{H^+} \qquad \forall\, t \in T \tag{7.2}$$

$$P_t^{H^+} = F_t^{Elz} \cdot \Gamma^{H^+} \qquad \forall\, t \in T \tag{7.3}$$

$$\Delta H_t^{H^+} = F_t^{Elz} \cdot \omega^{H^+} \qquad \forall\, t \in T. \tag{7.4}$$

The generated LOHC can then be stored in the liquid form under the ambient condition and transported to hydrogen fueling stations. In such a case, the LOHC density of 630 $m^3_{H_2}/m^3_{LH}$ offers the capability to store/transport 57 kg of hydrogen in one cubic meters of LOHC [154]. Once LOHC is transported to the hydrogen fueling stations, it should be converted back to the hydrogen gas using a dehydrogenation unit before being loaded to the vehicles. Dehydrogenation is an endothermal process that requires heat energy (i.e., ω^{H^-}= 0.75 kWh/$m^3_{H_2}$), in addition to electric power (i.e., Γ^{H^-}= 0.0195 MWh/m^3_{LH}= 0.031 kWh/$m^3_{H_2}$) for operation with an efficiency of η^{H^-}= 99% [104]. In this regard, (7.5) states the conversion of LOHC to hydrogen gas while (7.6) and (7.7) express the required electricity and heat energy during the dehydrogenation process, respectively [104].

$$F_t^{H_2} = F_t^{H^-} \cdot \eta^{H^-} \,/\, \xi^{LH} \qquad \forall\, t \in T \tag{7.5}$$

$$P_t^{H^-} = F_t^{H^-} \cdot \Gamma^{H^-} \qquad \forall\, t \in T \tag{7.6}$$

$$\Delta H_t^{H^-} = F_t^{H_2} \cdot \omega^{H^-} \qquad \forall\, t \in T. \tag{7.7}$$

Based on the aforementioned discussion, the round-trip LOHC hydrogenation and dehydrogenation conversion process has an efficiency about 96%. Additional energy about 17.5% of the hydrogen energy content (i.e., 16.2% by dehydrogenation process heat requirement and 1.3% electric power requirements) is required by the LOHC conversion process. Compared to other conventional hydrogen storage process, such as hydrogen compression and liquification, LOHC storage is regarded as a more efficient process to store hydrogen. Storing hydrogen in a compressed form requires only an additional 10% of the hydrogen energy content. However, compressed hydrogen at the highest end of the typical storage pressure range at 350 bars has relatively low volumetric storage density of 20 kg/m3) [155].

While, the hydrogen liquification process has high additional energy demand represented by 36 – 45% of the hydrogen energy content to store 71 kg hydrogen in 1 m^3 [155].

To that end, in order to maximize the efficacy and economic viability of an LOHC–based system, each component needs to be optimally sized and scheduled as elaborated in Sections 7.3 and 7.4.

7.3 Proposed Sizing Algorithm for LOHC Facility

One of the important motivations to the optimal sizing would be to minimize the CAPEX and operating costs in order to enhance the system net profit. In this regard, a Monte Carlo–based algorithm is proposed in this section to maximize the project net profit by shrinking the system initial and operating costs. The following quantities are inputted to the proposed algorithm that utilizes the Monte Carlo simulation for optimal sizing: (i) the LOHC demand by the hydrogen fueling stations, (ii) historical electricity prices, (iii) cost of LOHC facility components, and (v) ancillary service prices and contracted service hours. Two types of ancillary services are considered in this chapter as follows: (i) VAR support to the grid and (ii) DR in which the facility is scheduled to absorb not more than a certain quantity of power, when requested by the utility operator [142]. The Monte Carlo–based algorithm generates several scenarios, s, for the sizing problem. In such a case, the system net profit as a function of the facility size, to be maximized by the algorithm, is given as:

$$\text{Maximize} : \Big\{ \text{Rev}(s) - \text{Cost}(s) - \big(\text{CAPEX}(s)/LS\big) \Big\} \quad \forall s \in S, \tag{7.8}$$

where (7.8) states the annual net profit by deducting the costs and annualized CAPEX from the revenue (i.e., Rev). The project CAPEX is given in (7.9) as a function of the LOHC facility components including: (i) electrolyzer (P_{max}^{Elz}), (ii) electrolyzer converter (S_{max}^{Con}), (iii) hydrogenation unit inflow (i.e., F_{max}^{Elz}), and (iv) LOHC storage reservoir (SOC_{max}^{LH}).

$$\text{CAPEX}(s) = P^{Elz}_{max}(s) \cdot C^{Elz} + S^{Con}_{max}(s) \cdot C^{Con} + F^{Elz}_{max}(s) \cdot C^{H^+} + SOC^{LH}_{max}(s) \cdot C^{Sto} \quad \forall s \in S. \quad (7.9)$$

The system gross revenue depicted in (7.10) states the profit obtained from the LOHC–based fuel sale, in addition to the revenue from ancillary service provision to the market. In such a set–up, ancillary services can be provided using the following two components: (i) the electrolyzer converter interconnected with the power grid that would provide VAR support, and (ii) a reserve capacity margin within the LOHC storage reservoir that would realize DR services. The former service is stemmed from the ability of a power electronic–based converter that can be controlled to absorb/inject VAR from/to the grid in response to a signal received from the grid operator. The latter, however, is originated from the capability of storage to reserve energy that would be used for LOHC supply when the grid operator requests the facility to consume less power, known as the capacity based–demand response program [6]. Various ancillary services could be offered by the LOHC–based facility to the electricity market such as frequency regulation and reserve provision. However, such services require LOHC to power conversion, thereby adding financial burden to the facility operator; such an arrangement would need the following additional components: (i) dehydrogenation unit to convert LOHC to hydrogen gas and (ii) fuel cell unit to convert the hydrogen back to electricity. This is to ensure maintaining bi–directional energy exchange with the grid, i.e., charge from and discharge to the grid [156, 157]. In addition, bi-directional energy conversation causes higher energy losses and reduces the system overall efficiency. As such, DR and ancillary services are considered in this study that would only require adjustment in the intake power rather than bi-directional energy exchange. In such a case, DR and VAR ancillary services contractual agreement between the consumer (i.e., LOHC–based facility) and grid operator is carried out. Such a contract represents an

agreement between a dispatchable electricity consumer and the grid operator that declares: (i) the DR/VAR signal quantity sent to the participant by the grid operator, (ii) the financially compensation for the participant, and (iii) the maximum number and duration of daily signals that could be sent by the grid operator [158]. The profit resulted from ancillary services provision to the grid is calculated based on the service hours contracted between the facility and the grid operator. Therefore, the profit from the DR services is given as the product of the DR service hours (H^{DR}), DR service price (DR^{Prc}), and the minimum contracted DR signal (i.e., P^{DR}_{min}); this is similar for the VAR services denoted by Q^{Con}_{max}, as:

$$\begin{aligned}\text{Rev}(s) = \sum_{t \in T} F^{LH}_{t,Dem}(s) \cdot LH^{Prc} \cdot \Delta t + H^{VAR} \cdot VAR^{Prc} \cdot Q^{Con}_{max}(s) \\ + H^{DR} \cdot DR^{Prc} \cdot P^{DR}_{min}(s) \quad \forall\, s \in S.\end{aligned} \tag{7.10}$$

The annual cost is given in (7.11) as the product of the annual operating hours (i.e., OH) and the following terms: (i) the electricity consumption and operating cost of the hydrogenation unit, i.e., $F^{Elz}_{max} \cdot$, $(OC^{H^+} + \Gamma^{H^+} \cdot E^{A,Prc})$, (ii) the operating cost of the storage unit, i.e., $SOC^{LH}_{max} \cdot OC^{Sto}$, and (iii) the electrolyzer electricity consumption and operating cost, i.e., $P^{Elz}_{max} \cdot (E^{A,Prc} + OC^{Elz})$:

$$\begin{aligned}\text{Cost}(s) = OH(s) \cdot \Big\{ F^{Elz}_{max}(s) \cdot \Big(OC^{H^+} + \Gamma^{H^+} \cdot E^{A,Prc}(s) \Big) + \\ SOC^{LH}_{max}(s) \cdot OC^{Sto} + P^{Elz}_{max}(s) \cdot \Big(E^{A,Prc}(s) + OC^{Elz} \Big) \Big\} \forall\, s \in S,\end{aligned} \tag{7.11}$$

where $E^{A,Prc}$ represents the average of the electricity prices during the operating hours. In this work, the average value of the electricity prices in a given scenario, s, involves computing the average of the annual minimum electricity prices for the annual operation

percentage of scenario s as follows:

$$E^{A,Prc}(s) = \frac{\sum_{t \in T} \left\{ \min_{OH} \left(E_t^{Prc}(s) \right) \right\}}{OH} \quad \forall\, s \in S \wedge \forall\, OH = \rho \cdot h^{Ann}, \tag{7.12}$$

where OH is the product of the percentage of annual operation, ρ, of a scenario s, and the annual hours h^{Ann} i.e., 8760 hours. The aforementioned equation implies that the facility would operate and store LOHC during low electricity price instances to maximize its profit. As elaborated in Section 7.4, $E^{A,Prc}$ is used to calculate the optimized average electricity price for seasonal scheduling of the LOHC generation and storage plants.

The objective function in (7.8) is subject to the electrolyzer and the hydrogenation unit constraints as given below:

$$P_{max}^{Elz}(s) \geq \frac{\sum_{t \in T} F_{t,Dem}^{LH}(s) \cdot \Delta t}{OH(s) \cdot \xi^{LH} \cdot \eta^{H^+} \cdot \Gamma^{Elz} \cdot \eta^{Elz}} \quad \forall\, s \in S \tag{7.13}$$

$$F_{max}^{Elz}(s) = P_{max}^{Elz}(s) \cdot \Gamma^{Elz} \cdot \eta^{Elz} \quad \forall\, s \in S. \tag{7.14}$$

As stated in (7.13), the facility operating hours and the LOHC demand impact the sizing of the electrolyzer and hydrogenation unit. Distributing the hydrogen production across a wide range of operating hours minimizes the sizing of the components. However, the operation of the facility over a long period of time limits the possibility to exploit lower electricity market prices, thereby adversely impacting the overall profit.

The objective function in (7.8) is also subject to the storage SOC given as:

$$\begin{aligned} SOC_{t+1}^{LH}(s) = SOC_t^{LH}(s) + \Big(& F_{max}^{Elz}(s) \cdot \xi^{LH} \cdot \eta^{H^+} \cdot \Lambda_t \\ & - F_{t,Dem}^{LH}(s) - \gamma^{Dsp} \cdot SOC_t^{LH}(s) \Big) \cdot \Delta t \quad \forall\, s \in S \wedge \forall\, t \in T \end{aligned} \tag{7.15}$$

$$SOC_{min}^{LH}(s) \leq SOC_t^{LH}(s) \leq SOC_{max}^{LH}(s) \quad \forall\, s \in S \wedge \forall\, t \in T \tag{7.16}$$

$$\Lambda_t(s) = \begin{cases} 1 \;\; \forall \; E_t^{Prc}(s) \leq E^{BE}(s) \\ 0 \;\; \forall \; E_t^{Prc}(s) > E^{BE}(s) \end{cases} \qquad \forall \; s \in S \wedge \forall \; t \in T, \tag{7.17}$$

where (7.15) and (7.16) represent the energy balance equation, and the SOC limit of the LOHC storage reservoir, respectively. Equation (7.17) determines the ON/OFF operating state of the LOHC–based facility at each time step t, represented by $\Lambda_t = 1$ and 0, respectively. As stated in (7.17), the facility operates when the market price is below the break even price (i.e., E^{BE}) to ensure the system rate of return.

Providing ancillary services to the grid stacks additional means of profit to the revenue resulted from the LOHC–based fuel sale. Nonetheless, ancillary services provision could limit the capability of the electrolyzer unit for hydrogen production, which needs to be considered in the sizing problem in order to ensure the LOHC production reliability is not impacted. In this regard, the optimization problem is subject to (7.18), which optimizes the storage reserve margin to provide VAR support to the grid.

$$H^{VAR} \cdot \lambda^{VAR}(s) \cdot P_{max}^{Elz}(s) \leq \frac{SOC^{VAR}(s)}{\xi^{LH} \cdot \eta^{H^+} \cdot \Gamma^{Elz} \cdot \eta^{Elz}} \quad \forall \; s \in S; \tag{7.18}$$

equation (7.18) implies that the stored LOHC energy for VAR support (i.e., SOC^{VAR}) should be at least equal to the contracted VAR requirements, where the electrolyzer power limitation factor due to the VAR ancillary service is given as follows:

$$\lambda^{VAR}(s) = \frac{P_{max}^{Elz}(s) - \sqrt{S_{max}^{Con}(s)^2 - Q_{max}^{Con}(s)^2}}{P_{max}^{Elz}(s)} \quad \forall \; s \in S. \tag{7.19}$$

Similarly, the reserve SOC margin constraint for the DR ancillary service is defined as:

$$H^{DR} \cdot \Big(Sgn(P_{min}^{DR}) \cdot \lambda^{DR}(s) \Big) \cdot P_{max}^{Elz}(s) \leq \frac{SOC^{DR}(s)}{\xi^{LH} \cdot \eta^{H^+} \cdot \Gamma^{Elz} \cdot \eta^{Elz}} \quad \forall \; s \in S; \tag{7.20}$$

where (7.20) ensures that the LOHC storage reservoir maintains enough energy to accom-

modate the LOHC requirements, when the electrolyzer is set to lower operation in response to the DR signal. In (7.20), the DR limitation factor is defined as:

$$\lambda^{DR} = \frac{P^{Elz}_{max}(s) - P^{DR}_{min}(s)}{P^{Elz}_{max}(s)} \quad \forall\, s \in S, \tag{7.21}$$

Accordingly, the size of the storage reservoir in (7.9) is defined as the sum of maximum SOC over the optimization horizon and the reserve requirements for the VAR and DR support as below:

$$SOC^{LH}_{max}(s) = \max\{SOC^{LH}_{t}(s)\} + SOC^{DR}(s) + SOC^{VAR}(s) \quad \forall\, s \in S \wedge \forall\, t \in T. \tag{7.22}$$

In the next section, a scheduling model is presented for the optimally sized LOHC–based generation and storage plants. The scheduling model would adaptively manage the stored LOHC for concurrent services to the transportation sector and ancillary services market.

7.4 Proposed Scheduling Model for LOHC Facility

Fig. 7.2 represents the schematic diagram of the proposed framework in which an LOHC–based hydrogen generation/storage plant is managed by a scheduling algorithm. The scheduling model interacts with the electricity market operator, where it would receive market prices and communicate the ancillary services data. The optimization problem is executed by the scheduling algorithm, and the optimal setpoints are sent to the electrolyzer to produce the required amount of hydrogen and to follow the ancillary services signal. The generation and storage plants, however, would be owned and operated by a private investor and is scheduled by one central model. Such a setup brings about more opportunities for the operator of the stations from serving the transportation sector and power grid.

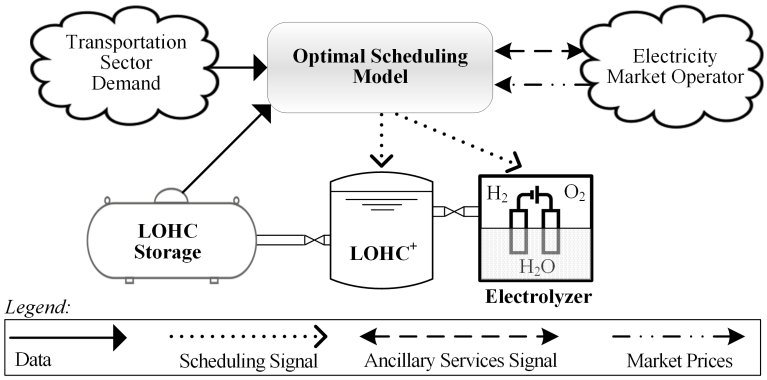

Figure 7.2: Optimal scheduling of LOHC–based generation and storage facility.

The proposed model for optimal scheduling of the LOHC–based facility is formulated below. The model aims to (i) optimally schedule the LOHC production unit to exploit the lower electricity market prices and (ii) participate to the transmission grid ancillary services. The objective function consists of four main terms that maximize the profit of the facility as formulated in the following:

$$\text{Maximize}: \sum_{t \in T} \left(R_t^{Sch} - \text{OPEX}_t + R_t^{Rew} - \beta_t^{Pen} \right) \cdot \Delta t. \tag{7.23}$$

The first term in (7.23) represents the revenue (i.e., R_t^{Sch}), resulted from operation of the facility in the power and transportation markets, given as follows:

$$\begin{aligned} R_t^{Sch} = F_{t,Dem}^{LH} \cdot LH^{Prc} + VAR^{Prc} \cdot \mid Q_t^{Con} \mid + DR^{Prc} \cdot \\ (P_t^{DR} - P_t^{DRM}) - E_t^{Prc} \cdot (P_t^{Elz} + P_t^{H^+}) \;\; \forall\, t \in T. \end{aligned} \tag{7.24}$$

The second term in (7.23) includes the OPEX of the facility as:

$$\text{OPEX}_t = P_t^{Elz} \cdot OC^{Elz} + F_t^{Elz} \cdot OC^{H^+} + SOC_t^{LH} \cdot OC^{Sto} \quad \forall\, t \in T; \tag{7.25}$$

equation (7.25) ensures that the electrolyzer and hydrogenation unit OPEX are considered while optimizing the scheduling operation.

The third term in (7.23) states a function rewarding the LOHC–based facility to be operated during low electricity price instances as given below:

$$R_t^{Rew} = \rho^{Rew} \cdot P_t^{Elz} \cdot \left(E^{A,Prc} - E_t^{Prc}\right) \ \forall\, t \in T; \tag{7.26}$$

the reward function allows the scheduling model to provide long–term storage without requiring the long–term price forecast; the storage is charged when the real–time market price is below the optimized price threshold, as determined in Section 7.3. Here it is worth noting that the accurate hourly scheduling is performed using short–term market price forecast, while the reward function in (7.26) enhances the optimization horizon to enable seasonal storage; this is performed by motivating the facility to produce and store LOHC at very low market prices over the seasonal horizon. Where, it is assumed that the objective function would only minimizes the electricity cost associated with the hourly volatile electricity prices in the wholesale electricity market. While, other electricity costs, such as global adjustment and peak demand payments would be paid as a percentage of the electricity bill [110]. The fourth term in (7.23) aims to manage the participation of the LOHC–based facility to the ancillary services market. As stated in (7.27), this term penalizes the non–zero values of VAR and DR slack variables to ensure that the ancillary services signal is effectively followed by the facility:

$$\beta_t^{Pen} = \beta^{VAR} \cdot (Q_t^{VARM} + Q_t^{VARM'}) + \beta^{DR} \cdot P_t^{DRM} \ \forall\, t \in T. \tag{7.27}$$

Equation (7.28) below represents the constraint that forces the LOHC generation facil-

ity to provide the VAR support requested by the utility:

$$Q_t^{Con} = Q_t^{VAR} + Q_t^{VARM} - Q_t^{VARM'}$$
$$\forall\, Q_t^{VAR} \neq 0 \wedge\ 0 \leq Q_t^{VARM}, Q_t^{VARM'} \leq Q_t^{VAR} \wedge\ \forall\, t \in T; \tag{7.28}$$

as stated in (7.28), this equation is provisional to non–zero values of the ancillary services signal. Besides, slack variables Q_t^{VARM} and $Q_t^{VARM'}$ create soft constraints to ensure the feasibility of the optimization problem. It is worth noting that once no signal is issued by the utility, the power converter of the facility is operated at the unity power factor.

Similarly, equation (7.29) limits the operation of the LOHC generation facility up to the DR value commanded by the utility:

$$P_t^{Elz} \leq P_t^{DR} + P_t^{DRM} \quad \forall\, P_t^{DR} \neq 0 \wedge \forall\, 0 \leq P_t^{DRM} \leq P_{max}^{Elz} - P_t^{DR} \wedge\ \forall\, t \in T. \tag{7.29}$$

The objective function in (7.23) is also subject to the electrolyzer constraints as follows:

$$F_{min}^{Elz} \leq F_t^{Elz} \leq F_{max}^{Elz} \quad \forall\, t \in T. \tag{7.30}$$

The objective function is subject to (7.1), which expresses the hydrogen production as a function of the electrolyzer power consumption. The constraints related to the LOHC production and power consumption of the hydrogenation unit are also represented in (7.2) and (7.3), respectively.

The objective function is subject to the storage SOC balance equation as follows:

$$SOC_{t+1}^{LH} = SOC_t^{LH} + (F_t^{H^+} - F_{t,Dem}^{LH} - \gamma^{Dsp} \cdot SOC_t^{LH}) \cdot \Delta t \quad \forall\, t \in T, \tag{7.31}$$

where, the LOHC storage is constrained to its minimum and maximum bounds as follows:

$$\begin{aligned}\big(1-\mid Sgn(Q_t^{VAR})\mid\big)\cdot SOC^{VAR}+\big(1-Sgn(P_t^{DR})\big)\cdot SOC^{DR}\\ +SOC_{min}^{LH}\leq SOC_t^{LH}\leq SOC_{max}^{LH}\quad\forall\, t\in T;\end{aligned}\tag{7.32}$$

equation (7.32) states that the storage SOC should be greater than the physically–limited minimum value, (SOC_{min}^{LH}), plus the reserve margin for the DR, (SOC^{DR}), and VAR, (SOC^{VAR}), ancillary services to the grid. As stated in (7.32), once a signal is received for either of the VAR or DR support, the relevant reserve margin is released by reducing the lower limit.

The objective function is also subject to power/voltage constraints and power flow equations as follows:

$$P_{b,t}\leq P_{b,max}\ \ \forall\, t\in T\wedge\forall\, b\in B\tag{7.33}$$

$$V_{b,min}\leq V_{b,t}\leq V_{b,max}\quad\forall\, t\in T\wedge\forall\, b\in B\tag{7.34}$$

$$P_{b,t}=V_{b,t}\sum_{b'\in B}\Big(V_{b',t}\cdot Y_{bb'}\times\mathrm{Cos}(\delta_b-\delta_{b'}-\theta_{bb'})\Big)\ \forall\, t\in T\wedge\forall\, b\in B\tag{7.35}$$

$$Q_{b,t}=V_{b,t}\sum_{b'\in B}\Big(V_{b',t}\cdot Y_{bb'}\times\mathrm{Sin}(\delta_b-\delta_{b'}-\theta_{bb'})\Big)\ \forall\, t\in T\wedge\forall\, b\in B.\tag{7.36}$$

7.5 Numerical Studies

In this section, the proposed sizing and scheduling algorithm for the LOHC–based generation and storage facility is numerically evaluated. The daily, weekly, and monthly hydrogen demand data is adopted from the National Renewable Energy Laboratory of the United States Department of Energy [159]. Different station ratings are considered in order to provide fuel to vehicles according to the following range: 1190 to 2870 vehicles per week with an average hydrogen amount of 4.6 kg [160], where this range mimics the average gas

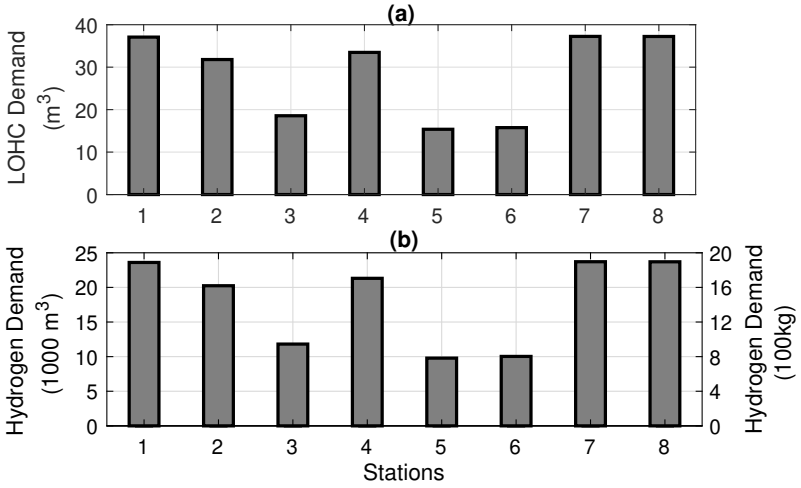

Figure 7.3: Demand at stations: (a) LOHC fuel and (b) equivalent of hydrogen gas.

demand from current gas fueling stations [160]. It is also worth noting that the demand of hydrogen by the transportation sector is converted to its LOHC equivalent using (7.5).

Fig. 7.3 shows the average daily demand by the transit sector at eight hydrogen fueling stations that needs to be provided by the LOHC–based generation facility [6]. Comparing Fig. 7.3 (a) and (b), one can realize how the LOHC technology can substantially reduce the fuel volume by converting and storing it in the liquid form; e.g., 22660 m^3 hydrogen gas has been reduced to 36.33 m^3 of LOHC. Accordingly, the LOHC demand quantities as depicted in Fig. 7.3 are used as input data for scenario design and case study in this chapter. It is worth noting that the demand of a centralized hydrogen generation plant (i.e., LOHC facility) is represented by aggregation of the individual vehicles demand. Such an accumulation of vehicles demand is known as temporal aggregation, which effectively reduces the uncertainties associated with the demand estimation or forecast [106]. Hence, without loss of generality, in this work the hydrogen demand is assumed to be represented by the average demand probability [159] that includes negligible uncertainties in both the sizing and scheduling models. Monte Carlo simulation and historical market prices are used for sizing purposes, while short–term point forecast data are employed for schedul-

Table 7.2: Modeling and Simulation Parameters

$\Gamma^{Elz} = 360$ ($m^3_{H_2}$/MWh)	$\eta^{Elz} = 60\%$
$\Gamma^{H^+} = 0.031$ (kWh/$m^3_{H_2}$)	$\eta^{H^+} = 97\%$
$\Gamma^{H^-} = 0.0195$ (MWh/m^3_{LH})	$\eta^{H^-} = 99\%$
$\xi^{LH} = 1/630$ ($m^3_{LH}/m^3_{H_2}$)	$LH^{Prc} = 250$ (\$/m^3_{LH})
$\gamma^{Dsp} \approx 0$	$C^{Con} = 120$ (1000\$/MVA)
$C^{Elz} = 600$ (1000\$/MW)	$OC^{Elz} = 3\% \times C^{Elz}/8760$ (\$/MWh)
$C^{H^+} = 1850$ (\$.h/$m^3_{H_2}$)	$OC^{H^+} = 3\% \times C^{H^+}/8760$ (\$/$m^3_{H_2}$)
$C^{Sto} = 2650$ (\$/m^3_{LH})	$OC^{Sto} = 2\% \times C^{Sto}/8760$ (\$/m^3_{LH}.h)
$H^{VAR} = 3$ (h)	$H^{DR} = 3$ (h)
$VAR^{Prc} = 30$ (\$/MVAr.h)	$DR^{Prc} = 30$ (\$/MWh)

ing. Table 7.2 reports the simulation and modeling parameters used for numerical studies [6, 104, 154]. The historical data from Ontario electricity market over the past five years are used for numerical studies [110]. The proposed sizing and scheduling models described in Section 7.3 and 7.4 are solved using the combined Interior Point nonlinear programming and Newton Trust Region algorithms [6]. Interior Point and Newton Trust Region programming techniques are already incorporated as built–in functions in MATLAB, referred to as *fmincon* toolbox. Hence, the optimization problem is coded and solved in the MATLAB environment. The optimization problem is executed in a PC with the following specifications: Core i7-6700, 3.4 GHz CPU, 16 GB RAM, and 64 bits system. The convergence tolerance and the maximum number of iterations are set to 10^{-6} and 500, respectively. It is found that the average execution time for the proposed sizing model is 3.5 seconds with 39 iterations on average. In addition, the average execution time for the proposed scheduling model is around 65 seconds with 27 iterations.

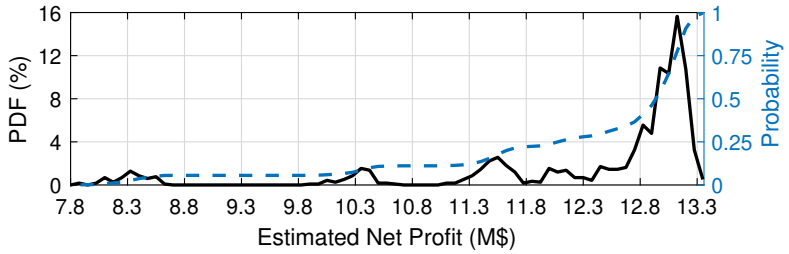

Figure 7.4: Probability density function & probability of LOHC facility annual profit.

7.5.1 Optimal Sizing of LOHC Generation and Storage Plants

In order to evaluate the sizing model, Monte Carlo simulation is used to generate various electricity price profiles. The historical electricity price profiles are inputted to the Monte Carlo simulation algorithm that would generate 60 annual electricity profiles. The electricity price profiles are generated using the Monte Carlo technique while bounded between the minimum and maximum values of the historical market data. Then, the generated annual electricity price profiles are mapped into different annual operation percentages (i.e., 15% up to 100% with a step of 5%) to generate 1080 scenarios in total. Each scenario represents one electricity price profile on an hourly basis over the year with a given percentage of the facility annual operation, which is inputted to the sizing model for numerical studies. Based on the input data, the proposed optimal sizing algorithm is executed and the annual net profit is computed for each scenario. Fig. 7.4 shows the PDF and probability of the estimated annual net profit for all simulated scenarios. As shown in the figure, the annual net profit is bounded between \$7.8 M and \$13.3 M, but the highest PDF value occurs at \$13.2 M. This means that while the profit could equal to any value between \$7.8 M and \$13.3 M, most likely it comes to around \$13.2 M per annum. In order to evaluate the profit on an average basis, the mean value of the market prices at each operating scenario is considered; accordingly, the annual net profit profile is computed, and the results are represented in Fig. 7.5 for each operating scenario. Fig. 7.5 also shows the CAPEX curve and the mean value of the electricity prices used for profit calculation. As shown in the

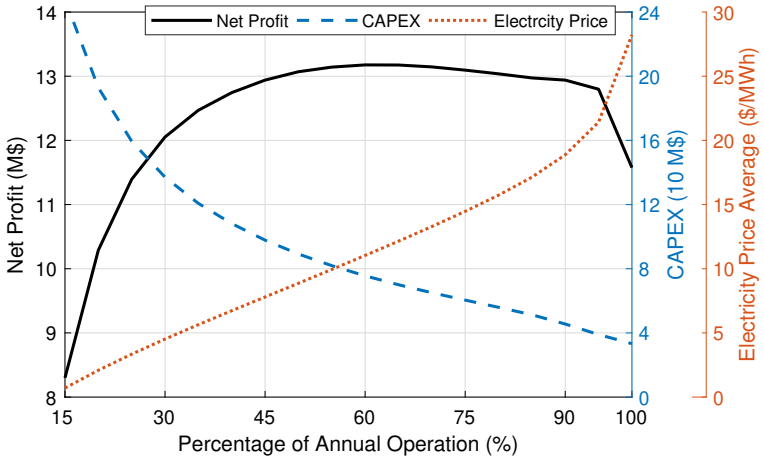

Figure 7.5: LOHC facility annual net profit, CAPEX, and average of electricity prices under various operating scenarios.

figure, the mean value of market prices at which the facility operate increases with the increase in the percentage of operation. The facility utilizes lower market price instances over the year, but as it operates more over the year, it has to utilize higher market price instances as well. For this reason, the average of the utilized market prices increases with an increase in the operation percentage. The CAPEX, however, reduces as the facility operates more since the facility can meet the demand with smaller ratings of components, thereby less expensive initial cost for each component. As such, higher percentage of operation positively impacts the CAPEX but adversely impacts the opportunity for utilizing lower market prices. In order to find the optimum point, the net profit should be taken into consideration as depicted in Fig. 7.5. As shown in the figure, the maximum profit of \$13.2 M occurs at 60% of operating hours over the year.

In order to evaluate the accuracy of the performed Monte Carlo simulations, the Confidence Interval (CI) for the simulated scenarios is computed which comes to at 95%. The CI represents an interval range including the true mean of a value with a probability of a specified confidence level [161]. In such a case, small CI values denote the precision of the estimated values reflecting the sufficiency of the simulated Monte Carlo scenarios [161]. To that end, a 95% CI value can be calculated as $1.96 \times \sigma/\sqrt{n}$ [161, 162]. In such a case,

Table 7.3: Original values and CIP of the evaluated parameters as depicted in Fig. 7.5

Annual Operation Percentage (%)	Electricity Price $/MWh (CIP)	Net Profit k$ (CIP)	CAPEX M$ (CIP)
15%	0.0310 (4.58%)	41.0 (0.49%)	0.5623 (0.22%)
20%	0.0284 (1.42%)	34.3 (0.33%)	0.4689 (0.24%)
25%	0.0271 (0.84%)	28.7 (0.25%)	0.3956 (0.24%)
30%	0.0263 (0.61%)	25.8 (0.21%)	0.3446 (0.25%)
35%	0.0255 (0.47%)	23.3 (0.18%)	0.3037 (0.25%)
40%	0.0250 (0.38%)	19.6 (0.15%)	0.2491 (0.23%)
45%	0.0248 (0.33%)	19.0 (0.14%)	0.2357 (0.24%)
50%	0.0249 (0.29%)	16.2 (0.12%)	0.1898 (0.21%)
55%	0.0246 (0.25%)	16.2 (0.12%)	0.1823 (0.22%)
60%	0.0245 (0.23%)	15.0 (0.11%)	0.1735 (0.23%)
65%	0.0248 (0.21%)	14.9 (0.11%)	0.1753 (0.25%)
70%	0.0249 (0.19%)	12.7 (0.09%)	0.1371 (0.21%)
75%	0.0252 (0.18%)	11.4 (0.08%)	0.1106 (0.18%)
80%	0.0257 (0.17%)	11.5 (0.08%)	0.1075 (0.19%)
85%	0.0272 (0.16%)	10.8 (0.08%)	0.0904 (0.17%)
90%	0.0311 (0.17%)	9.4 (0.07%)	0.0660 (0.14%)
95%	0.0398 (0.19%)	10.8 (0.08%)	0.0436 (0.11%)
100%	0.0708 (0.26%)	17.7 (0.15%)	0 (0%)

σ denotes the standard deviation and n represents the population samples. The facility parameters are depicted in Fig. 7.5, while Table 7.3 reports the CI for such parameters. In addition, the Confidence Interval Percentage (CIP) that states the percentage of the CI to the parameter mean value is given in Table 7.3. As reported in the table, the electricity price average shows small CI and CIP values with average values of 0.0295 $/MWh and 0.61%, respectively. The CI for the net profit of the LOHC–based facility comes to an average value of $18.8k which equates to about CIP of 0.1625%. Moreover, the results indicate low CI and CIP values for the CAPEX of the LOHC–based facility with CI of $0.21M on average, which equates to about 0.2% CIP on average. Given the low values of CI and CIP for the evaluated parameters of the LOHC facility, the number of simulated

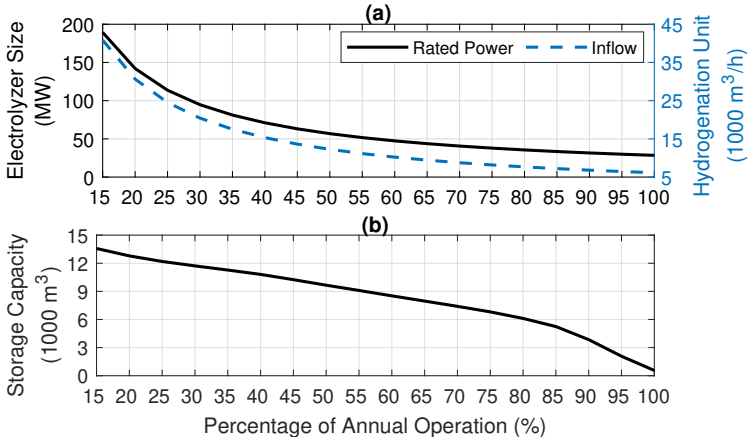

Figure 7.6: Component sizing: (a) electrolyzer rated power and hydrogenation unit inflow capacity, and (b) LOHC storage capacity, at various operating scenarios.

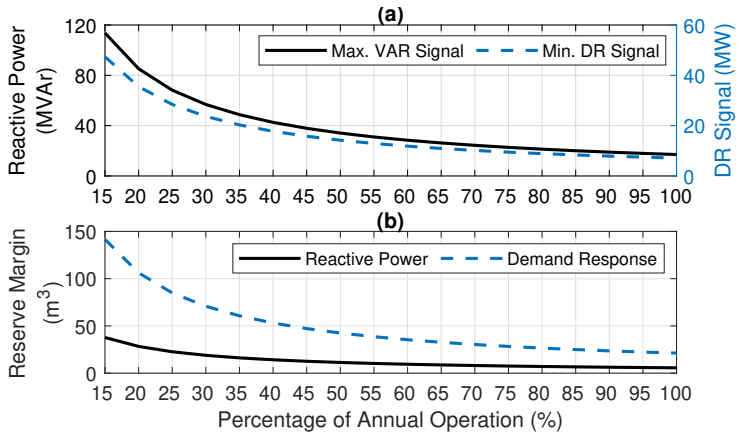

Figure 7.7: (a) Maximum VAR and minimum DR signals, and (b) required reserve margin for VAR and DR ancillary service, at various operating scenarios.

Monte Carlo scenarios is deemed adequate.

Having the optimum operation determined (i.e., 60% in this case), the optimum sizing of various components can be determined as discussed below.

Fig. 7.6 (a) shows the electrolyzer rated power and the LOHC hydrogenation unit inflow (i.e., electrolyzer outflow) at various operating scenarios. Fig. 7.6 (b), on the other hand, shows the LOHC storage capacity at various operating scenarios. As depicted in the figures, at higher operation percentage, smaller ratings for the electrolyzer (and thus hydrogenation) and storage capacity is required. Fig. 7.7 represents the maximum VAR

Table 7.4: Optimal Ratings of Various Components of LOHC–based Facility

P^{Elz}_{max}= 47.5 MW	SOC^{LH}_{max}= 8500 m^3_{LH}	P^{DR}_{min}= 12 MW
F^{Elz}_{max}= 10200 $m^3_{H_2}$	SOC^{DR}_{max}= 35.5 m^3_{LH}	Q^{Con}_{max}= 28.5 MVAr
S^{Con}_{max}= 47.5 MVA	SOC^{VAR}_{max}= 9.5 m^3_{LH}	$E^{A,Prc}$= 10.6 ($/MWh)

and minimum DR ancillary service signals and the required reserve margin by each ancillary service. It is noticed that the VAR ancillary service requires less reserve margin compared to DR services. This is because the DR ancillary service has a higher limitation factor upon the electrolyzer production compared to the VAR ancillary service. Accordingly, at the optimum operation percentage of 60%, the ratings of various components and requirements are computed and reported in Table 7.4. It is noteworthy that the CAPEX of the facility is considered as $75.6M at the optimum operation percentage.

7.5.2 Optimal Operation Scheduling

The proposed scheduling model for the LOHC–based facility formulated in Section 7.4 is based upon a look–ahead optimization problem considering the next T hours as the optimization horizon. The scheduling quantities for the next T hours are determined by the optimization problem according to the demand forecast. The optimal set points are, then, recursively updated at each time steps (i.e., 1–hour in this work) through re–executing the optimization problem. In this regard, the SOC of the LOHC storage will be prepared accordingly to accommodate the transportation sector demand. The proposed scheduling model is evaluated using the well–known 30–bus IEEE transmission system shown in Fig. 7.8. It is worth noting that due to higher ratings of the LOHC generation facility, it is assumed that the facility is directly connected to the transmission grid and deals with the wholesale electricity market [163, 164]. As depicted in the figure, there is a large–scale facility for LOHC–based hydrogen generation attached to Bus 18 of the system. In addition to conventional generation plants, renewable energy generations are assumed

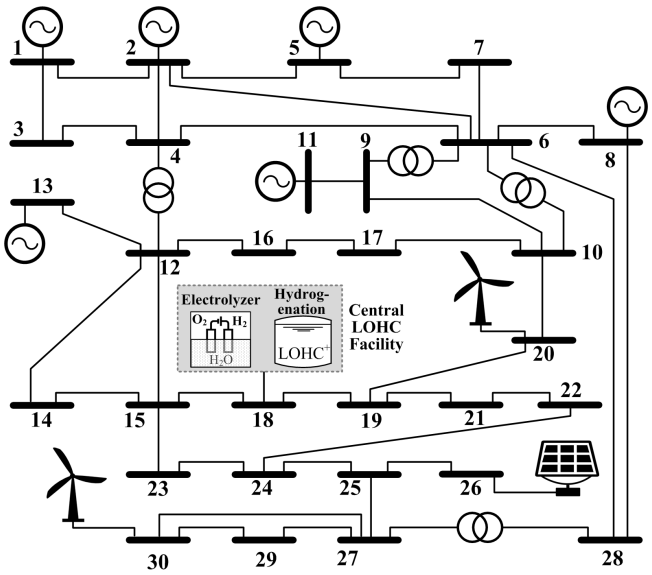

Figure 7.8: IEEE 30–bus transmission system employed for numerical studies.

to be installed. Wind turbines are located at Buses 20 and 30 with a rated capacity of 10 MW each, while a solar generation unit is located at Bus 26 with a rated capacity of 5 MW. Real–world load profile, wind generation, and solar data are obtained from Ontario for simulation purposes. The facility as optimally sized in Section 7.5.1 with the ratings reported in Table 7.4 is used for simulation. The proposed model is simulated for a typical year in Ontario market, and the results are discussed.

Fig. 7.9 represents the monthly average of (a) electricity prices, (b) electrolyzer and hydrogenation unit consumption, (c) LOHC–based fuel generation and demand, and (d) LOHC storage SOC. As shown in the figure, the electrolyzer shows higher operation during the months with lower market prices that would reduce the power purchase cost. It is noteworthy that the power consumption for hydrogenation process is only 0.69% of the electrolyzer consumption indicating that hydrogenation only slightly contributes to the power purchase cost (see Fig. 7.9 (b)). Fig. 7.9 (c) shows that the LOHC demand is fairly consistent in various months over the year, while hydrogen generation varies depending on the market prices in each month as shown in Fig. 7.9 (b). Fig. 7.9 (c) shows that the SOC

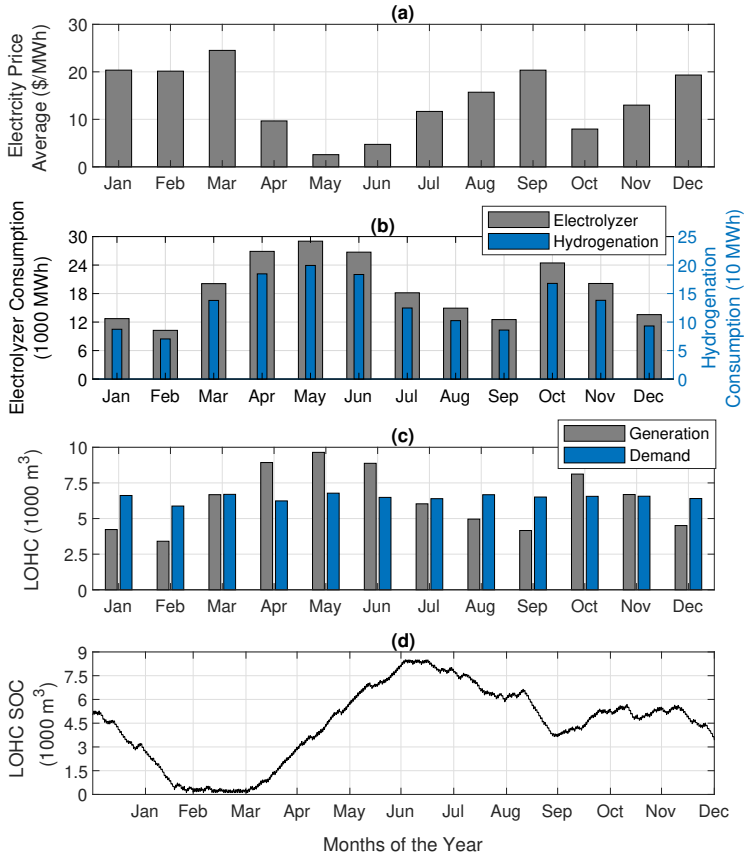

Figure 7.9: Monthly average of: (a) electricity price, (b) electrolyzer and hydrogenation unit consumption, (c) LOHC–based fuel generation and demand, and (d) LOHC storage SOC.

decreases when the demand exceeds the generation and vice versa as depicted in Fig. 7.9 (d). The storage SOC follows both the daily and seasonal trends as shown in Fig. 7.9 (c) that would improve both the short–term and long–term rate of return. Accordingly, the net profit for the simulated year is calculated as $14.76M.

7.5.3 Participation to Ancillary Services Market

Fig. 7.10 shows the hourly operation of the facility in response to the ancillary service signals for one week out of the studied year. The LOHC–based fuel delivery is assumed to

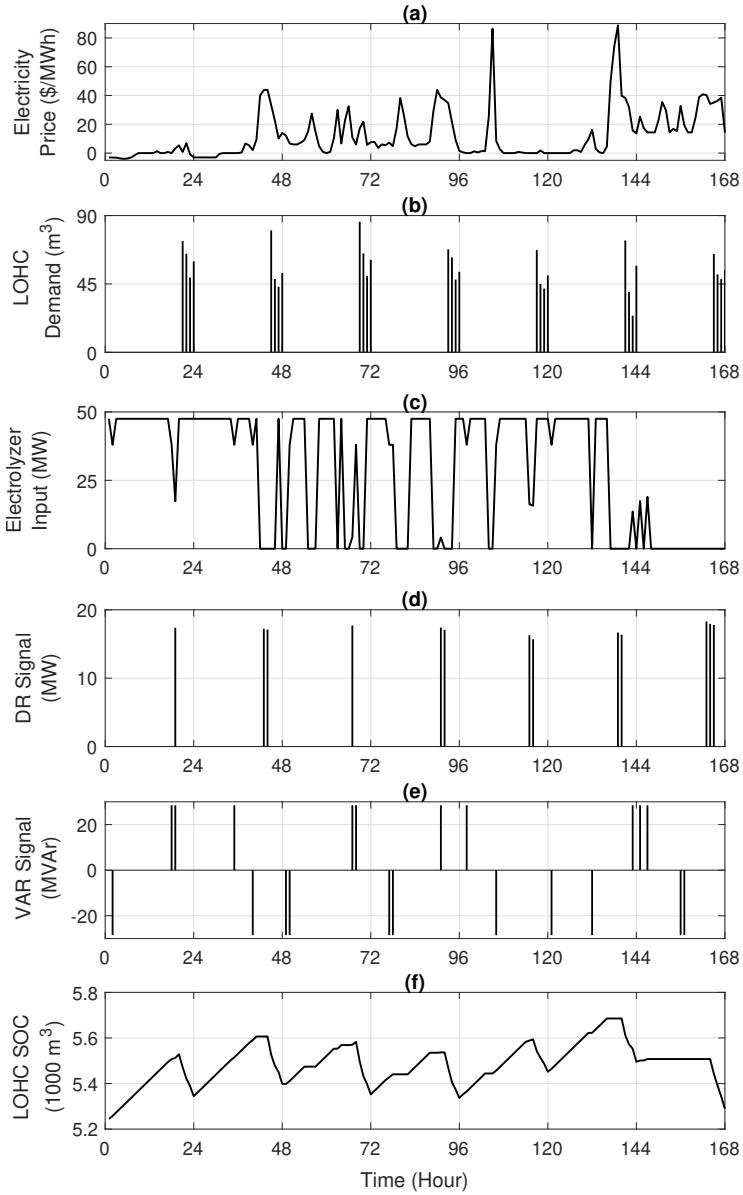

Figure 7.10: (a) electricity market price, (b) LOHC demand, (c) electrolyzer input power, (d) DR signal, (e) VAR signal, and (f) LOHC storage SOC, over a week.

take place towards the end of the day as shown in Fig. 7.10 (b), which is a time period for the trucks to transport the fuel from the generation site to fueling stations. As shown in Fig. 7.10 (c), the electrolyzer tends to operate during the period of low electricity prices. However, the operation of the electrolyzer is impacted once DR and VAR ancillary service

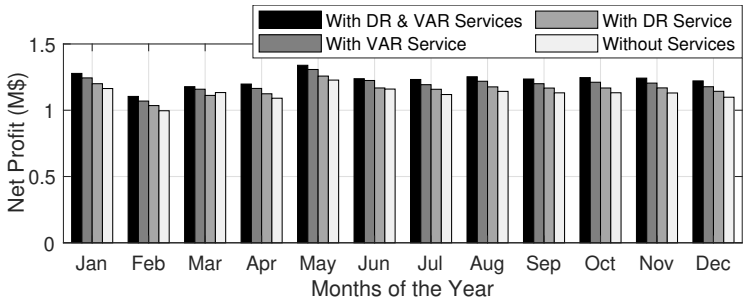

Figure 7.11: Monthly net profit with and without ancillary services contribution.

signals are issued since the facility has to operate as commanded by the utility operator. As shown in Figs. 7.10 (c) and (d), the input power of the electrolyzer is limited up to the value determined by the utility operator once a DR signal is issued. The facility takes no more than the utility–determined power to support the grid mainly during higher power demand periods. In addition, Figs. 7.10 (c) and (e) show that the operation of the electrolyzer is slightly impacted by the VAR signal; because the electrolyzer has to be operated in capacitive/reactive mode once reactive support is requested by the utility operator, thereby impacting its hydrogen generation capacity. Fig. 7.10 (f) shows the storage SOC variation in response to the operation of the electrolyzer and the hydrogen demand.

7.5.4 Profit Assessment

While the generation and storage facilities are operated for LOHC–based fuel supply to the transportation section, they are also utilized for ancillary services provision to the electricity market for higher profit. Fig. 7.11 shows the net profit of the LOHC facility achieved with and without participation to the ancillary services market. As shown in the figure, the net profit has been set to the lowest value when the facility does not provide any ancillary services, i.e., \$13.52 M per annum. The profit is elevated to \$13.88 M and \$14.37 M once the facility provides DR and VAR services, respectively. In addition, the

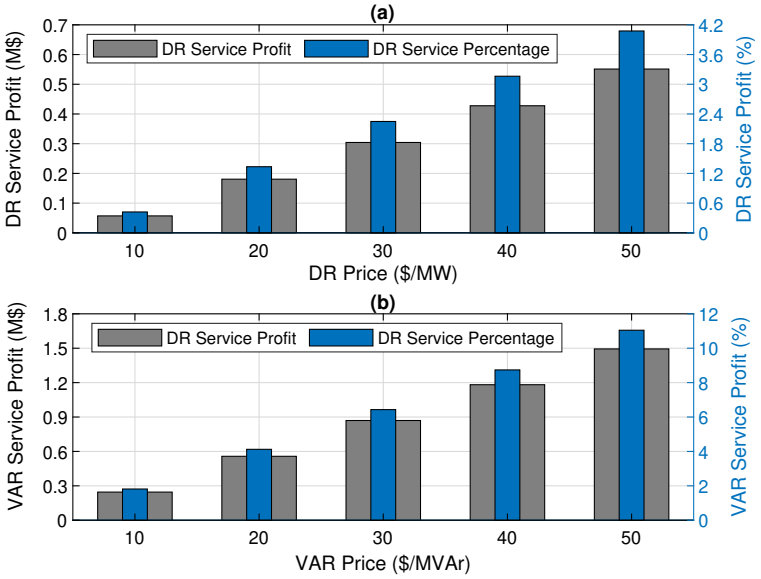

Figure 7.12: Ancillary services profit at different prices: (a) DR ancillary service, and (b) VAR ancillary service.

total annual net profit with participation to both the DR and VAR services results in \$14.76 M, thereby 9.17% enhancement in the net profit per annum.

7.5.5 Impact of Ancillary Services Price

Ancillary services price vary depending on the electricity market policies and regulations. For instance, California independent system operator (CAISO) offers DR regulation at 10 \$/MWh, while Pennsylvania New Jersey Maryland (PJM) interconnection operator in the US offers 30 \$/MWh for DR contribution [165]. In the case studies in Sections 7.5.1 and 7.5.2, 30 \$/MWh and 30 \$/MVAr are considered for contribution to the DR and VAR ancillary services, respectively. However, the impact of changes in these prices on the system profit is evaluated in this section, and the results are depicted in Fig. 7.12. As shown in Fig. 7.12 (a), the annual stacked profit resulted from the participation to the DR ancillary service is found to vary from \$57 k at the DR price of 10 \$/MWh up to \$551.2 k at 50 \$/MWh for the DR price. This corresponds to an additional profit of 0.42% up

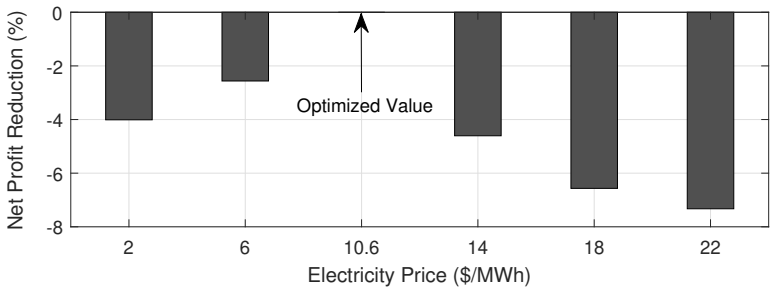

Figure 7.13: Net profit reduction at different electricity price threshold values.

to 4.1%, respectively, compared to the LOHC facility annul profit without participation in any services i.e., \$13.52M. Fig. 7.12 (b), represents the annual stacked profit resulted from the participation to the VAR ancillary services. As illustrated, the stacked profit varies from \$245.5 k at the VAR price of 10 \$/MVAr up to \$1.49 M at 50 \$/MVAr for the VAR price. This corresponds to an additional stacked profit of 1.81% up to 11%, respectively, compared to the LOHC facility annul profit without participation in any services.

7.5.6 Impact of Electricity Price Threshold Values

The application of the LOHC seasonal storage is presented as one of the features of the scheduling model in this chapter. In particular, the reward function in (7.26) motivates the facility to provide long–term storage (in addition to the short–term scheduling) without the need for long–term price forecasting. The optimized price threshold value for seasonal storage is determined as 10.6 \$/MWh as stated in Section 7.5.1. However, the impact of the facility's net profit at different price threshold values is worth evaluating as carried out in this section. Fig. 7.13 depicts the reduction in the net profit at different electricity price threshold values. As shown in the figure, the net profit is reduced by 4% and 2.56% at 2 \$/MWh and 6 \$/MWh, respectively, when the threshold value is lower than the optimized one. This is mainly due to the incapability of the LOHC generation facility to properly capture lower electricity prices when an unoptimized threshold is employed. In addition,

the facility's net profit decreases by 4.6%, 6.56%, and 7.32% at 14 $/MWh, 18 $/MWh, and 22 $/MWh threshold values, respectively, when the threshold is higher than the optimized value. This is due to the over–operation of the LOHC facility that leads to a generation level surplus to the required quantity by the transportation sector. As such it is imperative that the proper threshold for each market is used and regularly updated using the most recent market prices in order to maximize the profit generation.

7.6 Discussion and Summary

This chapter demonstrates how LOHC–based generation and storage plants can be sized and optimally operated for joint applications. A new model is proposed for optimal sizing and operation scheduling of LOHC facilities for concurrent services to both the transportation sector and ancillary services market. The model aims to (i) maximize the net profit of the facility through exploiting the lower market prices, (ii) satisfy the LOHC demand by the transportation sector, and (iii) participate to the ancillary services market. The ancillary service signals are incorporated into the scheduling model in order to prepare the generation and storage plants to effectively participate in the market. It is demonstrated that due to the LOHC higher density, massive amount of hydrogen can be stored in storage units with 1/630 m^3 smaller footprints, thereby allowing for the safe and reliable storage and transportation of the fuel. It is indicated that optimal scheduling of the LOHC–based generation and storage plants for concurrent services enhances the system rate of return. The proposed model shrinks the gap between the present and the expected rate of return of the LOHC facilities by about 10%, thereby promoting private investment in this area.

Chapter 8

Conclusions and Future Work

8.1 Summary and Conclusions

The research in this thesis presents a number of new algorithms to address and mitigate the integration challenges of the electrified transport networks into power grids. Specifically, the thesis focuses on addressing three main challenges; they are: sizing of personal battery-based and hydrogen-based EVFS (chapter 3), adoption of BEB to fully electrify PBT system and integrate them with existing power grids' infrastructure (chapter 4 and 5), and the integration of hydrogen-based generation and storage plants into power grids to serve the hydrogen powered transport sector (chapter 6 and 7).

Chapter 3 presents new analytical methodologies for the application to the size estimation of electric and hydrogen-based fueling stations as the two major foundations for electrified transportation. The ratings of various components are expressed in terms of the system operation percentage using the proposed formulation, and the desired ratings are selected at which the net profit reaches to the maximum point. Historical public-domain data from real-world systems are utilized for numerical evaluation of the proposed formulation. In addition, the estimation error of the proposed model is analyzed and compared

with artificial intelligence-based models for validation purposes. The results indicate that a trade-off has to be made between capital and operation costs in order to maximize the annual net profit while meeting the FCEVs/BEVs demand. Further, it is indicated that the operation percentage of the EVFS across the year to consume/store energy impacts the annual net profit, due to the variability in the wholesale electricity prices across the year. Using the proposed model in Chapter 3, it is demonstrated that the optimal value for the operation percentage can be estimated, and components can be sized accordingly towards maximizing the net profit.

Chapter 4 proposes a novel and generic model to calculate the EBEC without the need for a high time-resolution speed profile data. The proposed model generates a set of speed profiles using the basic information of the bus trip: trip time, trip length, and distances between successive bus stops. Roadway LoS is incorporated in the proposed model to simulate different traffic conditions. Further, a stochastic model for the bus speed profile is adopted to simulate the probability of the bus to stop at each on-route designated stop. The operation of the heat, ventilation and air conditioning system is also incorporated in the model using the thermal mass balance principle. The numerical results indicate that different trip directions might have different EBEC due to the route topography. Different weather temperatures also have a significant impact on the EBEC that can increase the energy consumption by more than 50%. In addition, the case studies reveal that traffic conditions impact the EBEC components. Moreover, the type of the BEB (i.e., single–decker versus double–decker) and the type of the transit service (city versus intercity bus service) affect the EBEC.

Chapter 5 proposes a new mathematical formulation to model BEB fleet systems. The model considers the operational requirements of PBT systems and the energy consumption characteristics of BEBs. The proposed transit model is then integrated with the power distribution system model to develop an integrated utility-transit problem formulation for the optimal design of BEB systems. The formulated optimization problem aims at determining

the optimal configuration parameters of BEB fleet systems that include: the bus battery capacity, chargers rated power, and the total number of installed chargers in the charging station. A real-world transit system data is used to validate the efficacy of the proposed integrated utility-transit model. The simulation results indicate that consideration of both power distribution and transit networks operation requirements significantly impact the choice of the BEBs configuration.

Chapter 6 presents a new model for optimal scheduling of hydrogen fueling stations to both serve the transport sector and the electricity market operator. The model schedules the stations to yield the maximum revenue via the stacked profit from multiple sources. Through such constraints, hydrogen sale prices would dynamically change to maintain the system profitable at the lowest possible hydrogen price. Numerical studies indicate that the system profit is considerably intensified once fueling stations participate to the CBDR program under the proposed model.

Chapter 7 presents optimal sizing and operation algorithms for LOHC–based hydrogen generation and storage facility to serve the FCEVs. It is demonstrated that the proposed model can alleviate the gap between the present and the expected rate of return of the LOHC–based plants via joint scheduling for DR and VAR services.

8.2 Future Work

Currently, there is an interesting research argument between the economic, efficient and reliable transit electrification technology to be deployed: Battery-based versus Fuel cell-based electrification concept. To be more concise, the key question is: what should be the optimal electrification mix between the two electrification technologies? In order to evidently answer such a question, profound technical, economical, and environmental investigations on both electrification technologies are required. These investigations will allow

for a better techno-economic decision making in the context of multiple transport electrification scenarios, the impact of each electrification scenario on the power grid, and the different mitigation strategies. Therefore, the research work in this thesis can be extended in future studies as listed below:

- Investigate the planning and operation mechanisms of the electrified bus fleets using battery-swapping and in-motion wireless charging techniques and compare such mechanisms with opportunity and overnight charging practices.
- Identify and mitigate the impacts of mass electrification of PBT and freight transportation networks on local power distribution and bulk transmission systems.
- Optimize the variable renewable generation mix requirement for cleaner transit electrification in order to guarantee the potential target of adopting a zero-emission electrified transport networks.
- Investigate and compare different pathways to generate, store, and distribute hydrogen fuel to electrify wide fleets of personal, transit and freight transportation networks. This investigation will include different technologies for hydrogen production (power grid versus natural gas), hydrogen storage (gaseous versus liquefied) and hydrogen delivery (pipeline versus trailer).

References

[1] I. Pavić, T. Capuder, and I. Kuzle, "A comprehensive approach for maximizing flexibility benefits of electric vehicles," *IEEE Systems Journal*, vol. 12, no. 3, pp. 2882–2893, Sep. 2018.

[2] D. Nicolaides, D. Cebon, and J. Miles, "Prospects for electrification of road freight," *IEEE Systems Journal*, vol. 12, no. 2, pp. 1838–1849, Jun. 2018.

[3] X. Zhang, H. Peng, H. Wang, and M. Ouyang, "Hybrid lithium iron phosphate battery and lithium titanate battery systems for electric buses," *IEEE Transactions on Vehicular Technology*, vol. 67, no. 2, pp. 956–965, Feb. 2018.

[4] D. Nicolaides, D. Cebon, and J. Miles, "An urban charging infrastructure for electric road freight operations: A case study for cambridge uk," *IEEE Systems Journal*, vol. 13, no. 2, pp. 2057–2068, Jun. 2019.

[5] F. Ahmad, M. S. Alam, S. M. Shariff, and M. Krishnamurthy, "A cost-efficient approach to ev charging station integrated community microgrid: A case study of indian power market," *IEEE Transactions on Transportation Electrification*, vol. 5, no. 1, pp. 200–214, Mar. 2019.

[6] N. A. El-Taweel, H. Khani, and H. E. Z. Farag, "Hydrogen storage optimal scheduling for fuel supply and capacity-based demand response program under dynamic hydrogen pricing," *IEEE Transactions on Smart Grid*, vol. 10, no. 4, pp. 4531–4542, Jul. 2019.

[7] "Energy efficiency for transportation and alternative fuels, 2020 fuel consumption guide,natural resources canada (NRCan."

[8] Y. Ligen, H. Vrubel, and H. H. Girault, "Mobility from renewable electricity: Infrastructure comparison for battery and hydrogen fuel cell vehicles," *World Electric Vehicle Journal*, vol. 9, no. 1, p. 3, 2018.

[9] H. Khani, N. A. El-Taweel, and H. E. Z. Farag, "Supervisory scheduling of storage-based hydrogen fueling stations for transportation sector and distributed operating reserve in electricity markets," *IEEE Transactions on Industrial Informatics*, vol. 16, no. 3, pp. 1529–1538, 2019.

[10] D. McPhail, "Evaluation of ground energy storage assisted electric vehicle DC fast charger for demand charge reduction and providing demand response," *Renewable energy*, vol. 67, pp. 103–108, Jul. 2014.

[11] M. O. Badawy and Y. Sozer, "Power flow management of a grid tied PV-battery system for electric vehicles charging," *IEEE Transactions on Industry Applications*, vol. 53, no. 2, pp. 1347–1357, Mar./Apr. 2017.

[12] S. Negarestani, M. Fotuhi-Firuzabad, M. Rastegar, and A. Rajabi-Ghahnavieh, "Optimal sizing of storage system in a fast charging station for plug-in hybrid electric vehicles," *IEEE Transactions on Transportation Electrification*, vol. 2, no. 4, pp. 443–453, Dec. 2016.

[13] J. Ugirumurera and Z. J. Haas, "Optimal capacity sizing for completely green charging systems for electric vehicles," *IEEE Transactions on Transportation Electrification*, vol. 3, no. 3, pp. 565–577, Sep. 2017.

[14] S. Faddel, A. T. Elsayed, and O. A. Mohammed, "Bilayer multi-objective optimal allocation and sizing of electric vehicle parking garage," *IEEE Transactions on Industry Applications*, vol. 54, no. 3, pp. 1992–2001, May 2018.

[15] S. Shojaabadi, S. Abapour, M. Abapour, and A. Nahavandi, "Optimal planning of plug-in hybrid electric vehicle charging station in distribution network considering demand response programs and uncertainties," *IET Generation, Transmission Distribution*, vol. 10, no. 13, pp. 3330–3340, 2016.

[16] H. Simorgh, H. Doagou-Mojarrad, H. Razmi, and G. B. Gharehpetian, "Cost-based optimal siting and sizing of electric vehicle charging stations considering demand response programmes," *IET Generation, Transmission Distribution*, vol. 12, no. 8, pp. 1712–1720, 2018.

[17] R. Xie, W. Wei, M. E. Khodayar, J. Wang, and S. Mei, "Planning fully renewable powered charging stations on highways: A data-driven robust optimization approach," *IEEE Transactions on Transportation Electrification*, vol. 4, no. 3, pp. 817–830, Sep. 2018.

[18] S. M. Mohammadi-Hosseininejad, A. Fereidunian, and H. Lesani, "Reliability improvement considering plug-in hybrid electric vehicles parking lots ancillary services:

a stochastic multi-criteria approach," *IET Generation, Transmission Distribution*, vol. 12, no. 4, pp. 824–833, 2018.

[19] L. Jia, Z. Hu, Y. Song, and Z. Luo, "Optimal siting and sizing of electric vehicle charging stations," in *2012 IEEE International Electric Vehicle Conference*, Mar. 2012, pp. 1–6.

[20] O. Erdinç, A. Taşcıkaraoğlu, N. G. Paterakis, Dursun, M. C. Sinim, and J. P. S. Catalão, "Comprehensive optimization model for sizing and siting of dg units, ev charging stations, and energy storage systems," *IEEE Transactions on Smart Grid*, vol. 9, no. 4, pp. 3871–3882, Jul. 2018.

[21] H. Zhang, S. J. Moura, Z. Hu, and Y. Song, "PEV fast-charging station siting and sizing on coupled transportation and power networks," *IEEE Transactions on Smart Grid*, vol. 9, no. 4, pp. 2595–2605, Jul. 2018.

[22] M. M. Islam, H. Shareef, and A. Mohamed, "Optimal location and sizing of fast charging stations for electric vehicles by incorporating traffic and power networks," *IET Intelligent Transport Systems*, vol. 12, no. 8, pp. 947–957, 2018.

[23] V. Salapić, M. Gržanić, and T. Capuder, "Optimal sizing of battery storage units integrated into fast charging ev stations," in *2018 IEEE International Energy Conference (ENERGYCON)*, Jun. 2018, pp. 1–6.

[24] V. I. Herrera, A. Milo, H. Gaztañaga, A. González-Garrido, H. Camblong, and A. Sierra, "Design and experimental comparison of energy management strategies for hybrid electric buses based on test-bench simulation," *IEEE Transactions on Industry Applications*, vol. 55, no. 3, pp. 3066–3075, May 2019.

[25] Y. J. Jang, E. S. Suh, and J. W. Kim, "System architecture and mathematical models of electric transit bus system utilizing wireless power transfer technology," *IEEE Systems Journal*, vol. 10, no. 2, pp. 495–506, Jun. 2016.

[26] T. Zhang, X. Chen, Z. Yu, X. Zhu, and D. Shi, "A monte carlo simulation approach to evaluate service capacities of ev charging and battery swapping stations," *IEEE Transactions on Industrial Informatics*, vol. 14, no. 9, pp. 3914–3923, Sep. 2018.

[27] N. A. El-Taweel, M. Mohamed, and H. E. Farag, "Optimal design of charging stations for electrified transit networks," in *2017 IEEE Transportation Electrification Conference and Expo (ITEC)*, Jun. 2017, pp. 786–791.

[28] M. Mohamed, H. Farag, N. El-Taweel, and M. Ferguson, "Simulation of electric buses on a full transit network: Operational feasibility and grid impact analysis," *Electric Power Systems Research*, vol. 142, pp. 163 – 175, Jan. 2017.

[29] N. A. El-Taweel, H. E. Z. Farag, and M. Mohamed, "Integrated utility-transit model for optimal configuration of battery electric bus systems," *IEEE Systems Journal*, vol. 14, no. 1, pp. 738–748, 2020.

[30] M. Mohamed, M. Ferguson, and P. Kanaroglou, "What hinders adoption of the electric bus in canadian transit? perspectives of transit providers," *Transportation Research Part D: Transport and Environment*, vol. 64, pp. 134 – 149, Oct. 2018.

[31] C. C. Chan, "The state of the art of electric, hybrid, and fuel cell vehicles," *Proceedings of the IEEE*, vol. 95, no. 4, pp. 704–718, Apr. 2007.

[32] N. Mendis, K. M. Muttaqi, S. Perera, and S. Kamalasadan, "An effective power management strategy for a wind–diesel–hydrogen-based remote area power supply system to meet fluctuating demands under generation uncertainty," *IEEE Transactions on Industry Applications*, vol. 51, no. 2, pp. 1228–1238, Mar. 2015.

[33] C. Wang, X. Yang, Z. Wu, Y. Che, L. Guo, S. Zhang, and Y. Liu, "A highly integrated and reconfigurable microgrid testbed with hybrid distributed energy sources," *IEEE Transactions on Smart Grid*, vol. 7, no. 1, pp. 451–459, Jan. 2016.

[34] W. Xiao, Y. Cheng, W. Lee, V. Chen, and S. Charoensri, "Hydrogen filling station design for fuel cell vehicles," *IEEE Transactions on Industry Applications*, vol. 47, no. 1, pp. 245–251, Jan. 2011.

[35] J. Kurtz, M. Peters, M. Muratori, and C. Gearhart, "Renewable hydrogen-economically viable: Integration into the u.s. transportation sector," *IEEE Electrification Magazine*, vol. 6, no. 1, pp. 8–18, Mar. 2018.

[36] "Hydrogenics corporation. mississauga, on, Canada." accessed: 10-Jan-2020. [Online]. Available: http://www.hydrogenics.com

[37] L. Eudy and M. B. Post, "Fuel cell buses in US transit fleets: Current status 2017," 2017, accessed: 10-Jan-2020. [Online]. Available: https://www.nrel.gov/docs/fy18osti/70075.pdf

[38] M. A. Dulebenets, "Minimizing the total liner shipping route service costs via application of an efficient collaborative agreement," *IEEE Transactions on Intelligent Transportation Systems*, vol. 20, no. 1, pp. 123–136, Jan. 2019.

[39] M. Jalalian, S. Gholami, and R. Ramezanian, "Analyzing the trade-off between co2 emissions and passenger service level in the airline industry: Mathematical modeling and constructive heuristic," *Journal of Cleaner Production*, vol. 206, pp. 251 – 266, Jan. 2019.

[40] M. A. Dulebenets, "A comprehensive multi-objective optimization model for the vessel scheduling problem in liner shipping," *International Journal of Production Economics*, vol. 196, pp. 293 – 318, Feb. 2018.

[41] B. Moaveni and S. Najafi, "Metro traffic modeling and regulation in loop lines using a robust model predictive controller to improve passenger satisfaction," *IEEE Transactions on Control Systems Technology*, vol. 26, no. 5, pp. 1541–1551, Sep. 2018.

[42] N. A. El-Taweel, H. Khani, and H. E. Z. Farag, "Analytical size estimation methodologies for electrified transportation fueling infrastructures using public–domain market data," *IEEE Transactions on Transportation Electrification*, vol. 5, no. 3, pp. 840–851, 2019.

[43] Q. Yang, S. Sun, S. Deng, Q. Zhao, and M. Zhou, "Optimal sizing of PEV fast charging stations with markovian demand characterization," *IEEE Transactions on Smart Grid*, vol. 10, no. 4, pp. 4457–4466, Jul. 2019.

[44] T. S. Bryden, G. Hilton, B. Dimitrov, C. Ponce de León, and A. Cruden, "Rating a stationary energy storage system within a fast electric vehicle charging station considering user waiting times," *IEEE Transactions on Transportation Electrification*, vol. 5, no. 4, pp. 879–889, Dec. 2019.

[45] Z. Liu, F. Wen, and G. Ledwich, "Optimal planning of electric-vehicle charging stations in distribution systems," *IEEE Transactions on Power Delivery*, vol. 28, no. 1, pp. 102–110, Jan. 2013.

[46] G. Wang, Z. Xu, F. Wen, and K. P. Wong, "Traffic-constrained multiobjective planning of electric-vehicle charging stations," *IEEE Transactions on Power Delivery*, vol. 28, no. 4, pp. 2363–2372, Oct. 2013.

[47] H. Chen, Z. Hu, H. Luo, J. Qin, R. Rajagopal, and H. Zhang, "Design and planning of a multiple-charger multiple-port charging system for pev charging station," *IEEE Transactions on Smart Grid*, vol. 10, no. 1, pp. 173–183, Jan. 2019.

[48] A. Aljanad, A. Mohamed, H. Shareef, and T. Khatib, "A novel method for optimal placement of vehicle-to-grid charging stations in distribution power system using a quantum binary lightning search algorithm," *Sustainable Cities and Society*, vol. 38, pp. 174–183, Apr. 2018.

[49] A. Q. Jakhrani, A.-K. Othman, A. R. H. Rigit, S. R. Samo, and S. A. Kamboh, "A novel analytical model for optimal sizing of standalone photovoltaic systems," *Energy*, vol. 46, no. 1, pp. 675–682, 2012.

[50] C. Olcan, "Multi-objective analytical model for optimal sizing of stand-alone photovoltaic water pumping systems," *Energy conversion and management*, vol. 100, pp. 358–369, Aug. 2015.

[51] B. Escobar, J. Hernández, R. Barbosa, and Y. Verde-Gómez, "Analytical model as a tool for the sizing of a hydrogen production system based on renewable energy: The mexican caribbean as a case of study," *International journal of hydrogen energy*, vol. 38, no. 28, pp. 12 562–12 569, 2013.

[52] D. Wu, M. Kintner-Meyer, T. Yang, and P. Balducci, "Analytical sizing methods for behind-the-meter battery storage," *Journal of Energy Storage*, vol. 12, pp. 297–304, Aug. 2017.

[53] C. Yang, W. Lou, J. Yao, and S. Xie, "On charging scheduling optimization for a wirelessly charged electric bus system," *IEEE Transactions on Intelligent Transportation Systems*, vol. 19, no. 6, pp. 1814–1826, Jun. 2018.

[54] U. Guida and S. Leonard, "Zeeus: Zero emission urban bus system," in *2014 IEEE International Electric Vehicle Conference (IEVC)*, Dec. 2014, pp. 1–7.

[55]

[56] A. Lajunen, "Lifecycle costs and charging requirements of electric buses with different charging methods," *Journal of cleaner production*, vol. 172, pp. 56–67, Jan. 2018.

[57] M. Bartłomiejczyk, "Driving performance indicators of electric bus driving technique: Naturalistic driving data multicriterial analysis," *IEEE Transactions on Intelligent Transportation Systems*, vol. 20, no. 4, pp. 1442–1451, Apr. 2019.

[58] N. A. El-Taweel, A. Zidan, and H. E. Z. Farag, "Novel electric bus energy consumption model based on probabilistic synthetic speed profile integrated with hvac," *IEEE Transactions on Intelligent Transportation Systems*, In Press. 2020.

[59] X. Qi, G. Wu, K. Boriboonsomsin, and M. J. Barth, "Data-driven decomposition analysis and estimation of link-level electric vehicle energy consumption under real-world traffic conditions," *Transportation Research Part D: Transport and Environment*, vol. 64, pp. 36–52, Oct. 2018.

[60] T. Liu, H. Yu, H. Guo, Y. Qin, and Y. Zou, "Online energy management for multimode plug-in hybrid electric vehicles," *IEEE Transactions on Industrial Informatics*, vol. 15, no. 7, pp. 4352–4361, Jul. 2019.

[61] L. Li, C. Yang, Y. Zhang, L. Zhang, and J. Song, "Correctional dp-based energy management strategy of plug-in hybrid electric bus for city-bus route," *IEEE Transactions on Vehicular Technology*, vol. 64, no. 7, pp. 2792–2803, Jul. 2015.

[62] L. Li, S. You, and C. Yang, "Multi-objective stochastic MPC-based system control architecture for plug-in hybrid electric buses," *IEEE Transactions on Industrial Electronics*, vol. 63, no. 8, pp. 4752–4763, Aug. 2016.

[63] M. Gallet, T. Massier, and T. Hamacher, "Estimation of the energy demand of electric buses based on real-world data for large-scale public transport networks," *Applied energy*, vol. 230, pp. 344–356, Nov. 2018.

[64] Z. Gao, Z. Lin, T. J. LaClair, C. Liu, J.-M. Li, A. K. Birky, and J. Ward, "Battery capacity and recharging needs for electric buses in city transit service," *Energy*, vol. 122, pp. 588–600, Mar. 2017.

[65] X. He, S. Zhang, W. Ke, Y. Zheng, B. Zhou, X. Liang, and Y. Wu, "Energy consumption and well-to-wheels air pollutant emissions of battery electric buses under complex operating conditions and implications on fleet electrification," *Journal of cleaner production*, vol. 171, pp. 714–722, Jan. 2018.

[66] N. A. El-Taweel and H. E. Z. Farag, "Incorporation of battery electric buses in the operation of intercity bus services," in *2019 IEEE Transportation Electrification Conference and Expo (ITEC)*, Jun. 2019, pp. 1–6.

[67] M. Xylia, S. Leduc, P. Patrizio, F. Kraxner, and S. Silveira, "Locating charging infrastructure for electric buses in stockholm," *Transportation Research Part C: Emerging Technologies*, vol. 78, pp. 183–200, May 2017.

[68] J. Stempien and S. Chan, "Comparative study of fuel cell, battery and hybrid buses for renewable energy constrained areas," *Journal of Power Sources*, vol. 340, pp. 347–355, Feb. 2017.

[69] Y. Gao, S. Guo, J. Ren, Z. Zhao, A. Ehsan, and Y. Zheng, "An electric bus power consumption model and optimization of charging scheduling concerning multi-external factors," *Energies*, vol. 11, no. 8, p. 2060, Aug. 2018.

[70] M. T. Sebastiani, R. Lüders, and K. V. O. Fonseca, "Evaluating electric bus operation for a real-world brt public transportation using simulation optimization," *IEEE Transactions on Intelligent Transportation Systems*, vol. 17, no. 10, pp. 2777–2786, Oct. 2016.

[71] Z. Chen, L. Li, B. Yan, C. Yang, C. Marina Martínez, and D. Cao, "Multimode energy management for plug-in hybrid electric buses based on driving cycles prediction," *IEEE Transactions on Intelligent Transportation Systems*, vol. 17, no. 10, pp. 2811–2821, Oct 2016.

[72] G. Correa, P. Muñoz, T. Falaguerra, and C. Rodriguez, "Performance comparison of conventional, hybrid, hydrogen and electric urban buses using well to wheel analysis," *Energy*, vol. 141, pp. 537–549, Dec. 2017.

[73] H. He, M. Yan, C. Sun, J. Peng, M. Li, and H. Jia, "Predictive air-conditioner control for electric buses with passenger amount variation forecast," *Applied energy*, vol. 227, pp. 249–261, Oct. 2018.

[74] K. Kivekäs, J. Vepsäläinen, and K. Tammi, "Stochastic driving cycle synthesis for analyzing the energy consumption of a battery electric bus," *IEEE Access*, vol. 6, pp. 55 586–55 598, 2018.

[75] G. D. Filippo, V. Marano, and R. Sioshansi, "Simulation of an electric transportation system at the ohio state university," *Applied Energy*, vol. 113, pp. 1686 – 1691, Jan. 2014.

[76] N. Qin, A. Gusrialdi, R. P. Brooker, and A. T-Raissi, "Numerical analysis of electric bus fast charging strategies for demand charge reduction," *Transportation Research Part A: Policy and Practice*, vol. 94, pp. 386 – 396, Dec. 2016.

[77] E. Akhavan-Rezai, M. F. Shaaban, E. F. El-Saadany, and F. Karray, "Online intelligent demand management of plug-in electric vehicles in future smart parking lots," *IEEE Systems Journal*, vol. 10, no. 2, pp. 483–494, Jun. 2016.

[78] S. Pirouzi, J. Aghaei, M. A. Latify, G. R. Yousefi, and G. Mokryani, "A robust optimization approach for active and reactive power management in smart distribution networks using electric vehicles," *IEEE Systems Journal*, vol. 12, no. 3, pp. 2699–2710, Sep. 2018.

[79] Y. Wang, Y. Huang, J. Xu, and N. Barclay, "Optimal recharging scheduling for urban electric buses: A case study in davis," *Transportation Research Part E: Logistics and Transportation Review*, vol. 100, pp. 115 – 132, Apr. 2017.

[80] L. E. Teoh, H. L. Khoo, S. Y. Goh, and L. M. Chong, "Scenario-based electric bus operation: A case study of putrajaya, malaysia," *International Journal of Transportation Science and Technology*, vol. 7, no. 1, pp. 10 – 25, Mar. 2018.

[81] B.-R. Ke, C.-Y. Chung, and Y.-C. Chen, "Minimizing the costs of constructing an all plug-in electric bus transportation system: A case study in penghu," *Applied Energy*, vol. 177, pp. 649 – 660, Sep. 2016.

[82] Y. Cheng, W. Wang, Z. Ding, and Z. He, "Electric bus fast charging station resource planning considering load aggregation and renewable integration," *IET Renewable Power Generation*, vol. 13, no. 7, pp. 1132–1141, May 2019.

[83] A. Ursua, L. M. Gandia, and P. Sanchis, "Hydrogen production from water electrolysis: Current status and future trends," *Proceedings of the IEEE*, vol. 100, no. 2, pp. 410–426, Feb. 2012.

[84] J. Alazemi and J. Andrews, "Automotive hydrogen fuelling stations: An international review," *Renewable and Sustainable Energy Reviews*, vol. 48, pp. 483 – 499, Aug. 2015.

[85] G. Cai and L. Kong, "Techno-economic analysis of wind curtailment/hydrogen production/fuel cell vehicle system with high wind penetration in china," *CSEE Journal of Power and Energy Systems*, vol. 3, no. 1, pp. 44–52, Mar. 2017.

[86] M. Rouholamini, M. Mohammadian, C. Wang, and A. A. Gharaveisi, "Optimal fuzzy-based power management for real time application in a hybrid generation system," *IET Renewable Power Generation*, vol. 11, no. 10, pp. 1325–1334, Sep. 2017.

[87] Y. Xiao, X. Wang, P. Pinson, and X. Wang, "A local energy market for electricity and hydrogen," *IEEE Transactions on Power Systems*, vol. 33, no. 4, pp. 3898–3908, Jul. 2018.

[88] M. Korpas and A. T. Holen, "Operation planning of hydrogen storage connected to wind power operating in a power market," *IEEE Transactions on Energy Conversion*, vol. 21, no. 3, pp. 742–749, Sep. 2006.

[89] G. Taljan, C. Canizares, M. Fowler, and G. Verbic, "The feasibility of hydrogen storage for mixed wind-nuclear power plants," *IEEE Transactions on Power Systems*, vol. 23, no. 3, pp. 1507–1518, Aug. 2008.

[90] M. Eypasch, M. Schimpe, A. Kanwar, T. Hartmann, S. Herzog, T. Frank, and T. Hamacher, "Model-based techno-economic evaluation of an electricity storage system based on liquid organic hydrogen carriers," *Applied energy*, vol. 185, pp. 320–330, Jan. 2017.

[91] D. F. Recalde Melo and L. Chang-Chien, "Synergistic control between hydrogen storage system and offshore wind farm for grid operation," *IEEE Transactions on Sustainable Energy*, vol. 5, no. 1, pp. 18–27, Jan. 2014.

[92] H. Bakhtiari and R. A. Naghizadeh, "Multi-criteria optimal sizing of hybrid renewable energy systems including wind, photovoltaic, battery, and hydrogen storage with ϵ-constraint method," *IET Renewable Power Generation*, vol. 12, no. 8, pp. 883–892, 2018.

[93] P. García, J. P. Torreglosa, L. M. Fernandez, and F. Jurado, "Optimal energy management system for stand-alone wind turbine/photovoltaic/hydrogen/battery hybrid system with supervisory control based on fuzzy logic," *International Journal of Hydrogen Energy*, vol. 38, no. 33, pp. 14 146–14 158, Nov. 2013.

[94] F. Grüger, L. Dylewski, M. Robinius, and D. Stolten, "Carsharing with fuel cell vehicles: Sizing hydrogen refueling stations based on refueling behavior," *Applied energy*, vol. 228, pp. 1540–1549, Oct. 2018.

[95] A. Ghosh and V. Aggarwal, "Control of charging of electric vehicles through menu-based pricing," *IEEE Transactions on Smart Grid*, vol. 9, no. 6, pp. 5918–5929, Nov. 2018.

[96] C. Luo, Y. Huang, and V. Gupta, "Stochastic dynamic pricing for ev charging stations with renewable integration and energy storage," *IEEE Transactions on Smart Grid*, vol. 9, no. 2, pp. 1494–1505, Mar. 2018.

[97] T. Zhao, Y. Li, X. Pan, P. Wang, and J. Zhang, "Real-time optimal energy and reserve management of electric vehicle fast charging station: Hierarchical game approach," *IEEE Transactions on Smart Grid*, vol. 9, no. 5, pp. 5357–5370, Sep. 2018.

[98] Q. Yan, B. Zhang, and M. Kezunovic, "Optimized operational cost reduction for an ev charging station integrated with battery energy storage and pv generation," *IEEE Transactions on Smart Grid*, vol. 10, no. 2, pp. 2096–2106, Mar. 2019.

[99] W. Yuan, J. Huang, and Y. J. A. Zhang, "Competitive charging station pricing for plug-in electric vehicles," *IEEE Transactions on Smart Grid*, vol. 8, no. 2, pp. 627–639, Mar. 2017.

[100] C. Jin, J. Tang, and P. Ghosh, "Optimizing electric vehicle charging with energy storage in the electricity market," *IEEE Transactions on Smart Grid*, vol. 4, no. 1, pp. 311–320, Mar. 2013.

[101] S. Pal and R. Kumar, "Electric vehicle scheduling strategy in residential demand response programs with neighbor connection," *IEEE Transactions on Industrial Informatics*, vol. 14, no. 3, pp. 980–988, Mar. 2018.

[102] A. Fikrt, R. Brehmer, V.-O. Milella, K. Müller, A. Bösmann, P. Preuster, N. Alt, E. Schlücker, P. Wasserscheid, and W. Arlt, "Dynamic power supply by hydrogen bound to a liquid organic hydrogen carrier," *Applied energy*, vol. 194, pp. 1–8, May 2017.

[103] N. El-Taweel, H. Khani, and H. E. Z. Farag, "Optimal sizing and scheduling of LOHC-based generation and storage plants for concurrent services to transportation sector and ancillary services market," *IEEE Transactions on Sustainable Energy*, In Press. 2019.

[104] M. Reuß, T. Grube, M. Robinius, P. Preuster, P. Wasserscheid, and D. Stolten, "Seasonal storage and alternative carriers: A flexible hydrogen supply chain model," *Applied energy*, vol. 200, pp. 290–302, Aug. 2017.

[105] A. Haupt and K. Müller, "Integration of a LOHC storage into a heat-controlled chp system," *Energy*, vol. 118, pp. 1123–1130, Jan. 2017.

[106] B. Rostami-Tabar, M. Z. Babai, A. Syntetos, and Y. Ducq, "Demand forecasting by temporal aggregation," *Naval Research Logistics (NRL)*, vol. 60, no. 6, pp. 479–498, 2013.

[107] J. Kurtz, S. Sprik, C. Ainscough, and G. Saur, "Fuel cell electric vehicle (FCEV) performance composite data products," 2017.

[108] N. G. Paterakis and M. Gibescu, "A methodology to generate power profiles of electric vehicle parking lots under different operational strategies," *Applied energy*, vol. 173, pp. 111–123, Jul. 2016.

[109] H. Khani and H. E. Z. Farag, "Optimal day-ahead scheduling of power-to-gas energy storage and gas load management in wholesale electricity and gas markets," *IEEE Transactions on Sustainable Energy*, vol. 9, no. 2, pp. 940–951, Apr. 2018.

[110] "Power data, IESO, Toronto, Canada," accessed: 12-Jan-2020. [Online]. Available: http://www.ieso.ca/power-data

[111] M. Smith and J. Castellano, "Costs associated with non-residential electric vehicle supply equipment: Factors to consider in the implementation of electric vehicle charging stations," National Renewable Energy Laboratory (NERL), Tech. Rep., Nov. 2015.

[112] G. Parks, R. Boyd, J. Cornish, and R. Remick, "Hydrogen station compression, storage, and dispensing technical status and costs: Systems integration," National Renewable Energy Lab.(NREL), Tech. Rep., 2014.

[113] A. Ehsan and Q. Yang, "Coordinated investment planning of distributed multi-type stochastic generation and battery storage in active distribution networks," *IEEE Transactions on Sustainable Energy*, vol. 10, no. 4, pp. 1813–1822, Oct. 2019.

[114] "Highway capacity manual," Transportation research board, National Research Council, Washington, DC, Tech. Rep., 2000.

[115] H. Tian, X. Wang, Z. Lu, Y. Huang, and G. Tian, "Adaptive fuzzy logic energy management strategy based on reasonable soc reference curve for online control of plug-in hybrid electric city bus," *IEEE Transactions on Intelligent Transportation Systems*, vol. 19, no. 5, pp. 1607–1617, May 2018.

[116] "Thermo king bus hvac systems," accessed: 05-Feb-2020. [Online]. Available: https://www.thermoking.com/na/en/road/bus-and-shuttle/bus-hvac-systems.html

[117] E. Atam and L. Helsen, "Control-oriented thermal modeling of multizone buildings: Methods and issues: Intelligent control of a building system," *IEEE Control Systems Magazine*, vol. 36, no. 3, pp. 86–111, Jun 2016.

[118] R. J. Osczevski, "The basis of wind chill," *Arctic*, pp. 372–382, Dec. 1995.

[119] H. Cho, B. Liu, and K. Gowri, "Energy saving impact of ashrae 90.1 vestibule requirements: Modeling of air infiltration through door openings," Pacific Northwest National Lab.(PNNL), Richland, WA (United States), Tech. Rep., 2010.

[120] "Standard bus procurement guidelines–40 ft. low floor–diesel technical specifications," American Public Transportation Association, Tech. Rep., 2008.

[121] J. A. Pinzon, P. P. Vergara, L. C. P. da Silva, and M. J. Rider, "Optimal management of energy consumption and comfort for smart buildings operating in a microgrid," *IEEE Transactions on Smart Grid*, vol. 10, no. 3, pp. 3236–3247, May 2019.

[122] "Thermal environmental conditions for human occupancy," American Society of Heating and Refrigerating and Air-Conditioning Engineers (ASHRAE) and American National Standards Institute (ANSI), Tech. Rep., 2004.

[123] D. Göhlich, T.-A. Fay, D. Jefferies, E. Lauth, A. Kunith, and X. Zhang, "Design of urban electric bus systems," *Design Science*, vol. 4, 2018.

[124] "Brampton city, schedules and map," accessed: 05-Feb-2020. [Online]. Available: http://www.brampton.ca/EN/residents/transit/plan-your-trip/Pages/schedules.aspx

[125] "GO Transit, full schedules," accessed: 05-Feb-2020. [Online]. Available: https://www.gotransit.com/en/trip-planning/seeschedules/full-schedules

[126] G. R. Chehab, R. H. Chehade, L. Houssami, and R. Mrad, "Implementation initiatives of the mechanistic-empirical pavement design guide in countries with insufficient design input data–the case of lebanon," in *International Congress and Exhibition" Sustainable Civil Infrastructures: Innovative Infrastructure Geotechnology"*. Springer, 2017, pp. 147–167.

[127] "BYD, k9 specification," accessed: 05-Feb-2020. [Online]. Available: https://en.byd.com/wp-content/uploads/2019/07/4504-byd-transit-cut-sheets_k9-40_lr.pdf

[128] "Alexander dennis, enviro500 superlo specification," accessed: 05-Feb-2020. [Online]. Available: https://www.alexander-dennis.com/media/71947/enviro500-superlo-spec.pdf

[129] R. D. L. Vollaro, L. Evangelisti, G. Battista, P. Gori, C. Guattari, and A. Fanchiotti, "Bus for urban public transport: Energy performance optimization," *Energy Procedia*, vol. 45, pp. 731–738, 2014.

[130] V. Guihaire and J.-K. Hao, "Transit network design and scheduling: A global review," *Transportation Research Part A: Policy and Practice*, vol. 42, no. 10, pp. 1251 – 1273, Dec. 2008.

[131] H. Khani, N. El-Taweel, and H. E. Z. Farag, "Power congestion management in integrated electricity and gas distribution grids," *IEEE Systems Journal*, vol. 13, no. 2, pp. 1883–1894, Jun. 2019.

[132] P. Bonami, L. T. Biegler, A. R. Conn, G. Cornuéjols, I. E. Grossmann, C. D. Laird, J. Lee, A. Lodi, F. Margot, N. Sawaya, and A. Wächter, "An algorithmic framework for convex mixed integer nonlinear programs," *Discrete Optimization*, vol. 5, no. 2, pp. 186 – 204, May 2008.

[133] P. Bonami and J. P. M. Gonçalves, "Heuristics for convex mixed integer nonlinear programs," *Computational Optimization and Applications*, vol. 51, no. 2, pp. 729–747, Mar. 2012.

[134] "OPTI toolbox: Basic open source nonlinear mixed integer programming," accessed: 10-Jan-2020. [Online]. Available: https://www.inverseproblem.co.nz/OPTI/index.php/Solvers/BONMIN

[135] M. V. Kirthiga, S. A. Daniel, and S. Gurunathan, "A methodology for transforming an existing distribution network into a sustainable autonomous micro-grid," *IEEE Transactions on Sustainable Energy*, vol. 4, no. 1, pp. 31–41, Jan. 2013.

[136] "American national standard for electric power systems and equipment–voltage ratings (60 hertz), ANSI Std. c84.1," Dec 2006.

[137] S. Chung and O. Trescases, "Hybrid energy storage system with active power-mix control in a dual-chemistry battery pack for light electric vehicles," *IEEE Transactions on Transportation Electrification*, vol. 3, no. 3, pp. 600–617, Sep. 2017.

[138] L. Török, L. Mathe, C. K. Nielsen, and S. Munk-Nielsen, "Modeling and control of three-phase grid-connected power supply with a small dc-link capacitor for electrolyzers," *IEEE Transactions on Industry Applications*, vol. 53, no. 5, pp. 4634–4643, Sep. 2017.

[139] B. R. Naidu, G. Panda, and P. Siano, "A self-reliant dc microgrid: Sizing, control, adaptive dynamic power management, and experimental analysis," *IEEE Transactions on Industrial Informatics*, vol. 14, no. 8, pp. 3300–3313, Aug. 2018.

[140] N. Gyawali and Y. Ohsawa, "Integrating fuel cell/electrolyzer/ultracapacitor system into a stand-alone microhydro plant," *IEEE Transactions on Energy Conversion*, vol. 25, no. 4, pp. 1092–1101, Dec. 2010.

[141] M. M. A. Abdelaziz, M. F. Shaaban, H. E. Farag, and E. F. El-Saadany, "A multistage centralized control scheme for islanded microgrids with pevs," *IEEE Transactions on Sustainable Energy*, vol. 5, no. 3, pp. 927–937, Jul. 2014.

[142] "Capacity–based demand response. IESO, Toronto, Canada." accessed: 10-Jan-2020. [Online]. Available: http://www.ieso.ca/en/Sector-Participants/Market-Operations/Markets-and-Related-Programs/Demand-Response-Pilot

[143] A. H. Hajimiragha, M. R. Dadash Zadeh, and S. Moazeni, "Microgrids frequency control considerations within the framework of the optimal generation scheduling problem," *IEEE Transactions on Smart Grid*, vol. 6, no. 2, pp. 534–547, Mar. 2015.

[144] L. Bertuccioli, A. Chan, D. Hart, F. Lehner, B. Madden, and E. Standen, "Development of water electrolysis in the european union," *Fuel cells and hydrogen joint undertaking, E4tech, and Element Energy*, Feb. 2014.

[145] H. Khani and M. R. D. Zadeh, "Online adaptive real-time optimal dispatch of privately owned energy storage systems using public-domain electricity market prices," *IEEE Transactions on Power Systems*, vol. 30, no. 2, pp. 930–938, Mar. 2015.

[146] Z. Li, W. Wu, B. Zhang, and B. Wang, "Adjustable robust real-time power dispatch with large-scale wind power integration," *IEEE Transactions on Sustainable Energy*, vol. 6, no. 2, pp. 357–368, Apr. 2015.

[147] M. F. Torchio and M. G. Santarelli, "Energy, environmental and economic comparison of different powertrain/fuel options using well-to-wheels assessment, energy and

external costs – european market analysis," *Energy*, vol. 35, no. 10, pp. 4156 – 4171, Oct. 2010.

[148] S. Bashash and H. K. Fathy, "Cost-optimal charging of plug-in hybrid electric vehicles under time-varying electricity price signals," *IEEE Transactions on Intelligent Transportation Systems*, vol. 15, no. 5, pp. 1958–1968, Oct. 2014.

[149] H. Khani, N. A. El-Taweel, and H. E. Z. Farag, "Power loss alleviation in integrated power and natural gas distribution grids," *IEEE Transactions on Industrial Informatics*, vol. 15, no. 12, pp. 6220–6230, 2019.

[150] "Ancillary services market. IESO, Toronto, ON, Canada," accessed: 12-Jan-2020. [Online]. Available: http://www.ieso.ca/ancillary-services

[151] "Ancillary services market. AESO, Calgary, AB, Canada,," accessed: 12-Jan-2020. [Online]. Available: https://www.aeso.ca/market/ancillary-services

[152] J. Leithon, S. Sun, and T. J. Lim, "Demand response and renewable energy management using continuous-time optimization," *IEEE Transactions on Sustainable Energy*, vol. 9, no. 2, pp. 991–1000, Apr. 2018.

[153] "Midcontinent independent system operator MISO, Legal Tariff," accessed: 28-Jul-2020. [Online]. Available: https://www.misoenergy.org/legal/tariff/

[154] "Hydrogenious products, hydrogenious technologies," accessed: 12-Jan-2020. [Online]. Available: http://www.hydrogenious.net/en/products

[155] A. M. Abdalla, S. Hossain, O. B. Nisfindy, A. T. Azad, M. Dawood, and A. K. Azad, "Hydrogen production, storage, transportation and key challenges with applications: A review," *Energy conversion and management*, vol. 165, pp. 602–627, 2018.

[156] T. Nguyen, H. Yoo, and H. Kim, "A droop frequency control for maintaining different frequency qualities in a stand-alone multimicrogrid system," *IEEE Transactions on Sustainable Energy*, vol. 9, no. 2, Apr. 2018.

[157] Y. Yang, C. Shen, C. Wu, and C. Lu, "Control performance based dynamic regulation reserve allocation for renewable integrations," *IEEE Transactions on Sustainable Energy*, vol. 10, no. 3, pp. 1271–1279, Jul. 2019.

[158] J. A. Schachter and P. Mancarella, "Demand response contracts as real options: A probabilistic evaluation framework under short-term and long-term uncertainties," *IEEE Transactions on Smart Grid*, vol. 7, no. 2, pp. 868–878, Mar. 2016.

[159] "Fuel cell electric vehicle composite data products," accessed: 12-Jan-2020. [Online]. Available: https://www.nrel.gov/hydrogen/fuel-cell-electric-vehicle-cdps.html

[160] T. P. Chen, "Hydrogen delivey infrastructure option analysis," Nexant, Inc., US Department of Energy Fuel Cell Technologies Office, Tech. Rep., 2010.

[161] S. Patil and D. J. Lilja, "Using resampling techniques to compute confidence intervals for the harmonic mean of rate-based performance metrics," *IEEE Computer Architecture Letters*, vol. 9, no. 1, pp. 1–4, Jan. 2010.

[162] G. Rubino and B. Tuffin, *Rare event simulation using Monte Carlo methods*. John Wiley & Sons, 2009.

[163] "Connection assessments, IESO, Toronto, Canada," accessed: 12-Jan-2020. [Online]. Available: http://www.ieso.ca/Sector-Participants/Connection-Assessments/Obtaining-A-Connection-Assessment

[164] J. Wang, H. Zhong, W. Tang, R. Rajagopal, Q. Xia, and C. Kang, "Tri-level expansion planning for transmission networks and distributed energy resources considering transmission cost allocation," *IEEE Transactions on Sustainable Energy*, vol. 9, no. 4, pp. 1844–1856, Oct. 2018.

[165] F. Rahimi and A. Ipakchi, "Using a transactive energy framework: Providing grid services from smart buildings," *IEEE Electrification Magazine*, vol. 4, no. 4, pp. 23–29, Dec. 2016.

[166] M. Mahmoud, R. Garnett, M. Ferguson, and P. Kanaroglou, "Electric buses: A review of alternative powertrains," *Renewable and Sustainable Energy Reviews*, vol. 62, pp. 673 – 684, Sep. 2016.

[167] "Pantograph down | ABB opportunity charging for electric buses," accessed: 10-Jan-2020. [Online]. Available: http://new.abb.com/ev-charging/products/opportunity-charging

[168] M. Eypasch, M. Schimpe, A. Kanwar, T. Hartmann, S. Herzog, T. Frank, and T. Hamacher, "Model-based techno-economic evaluation of an electricity storage system based on liquid organic hydrogen carriers," *Applied Energy*, vol. 185, pp. 320 – 330, Jan. 2017.

[169] E. Heydarian-Forushani, M. E. H. Golshan, M. Shafie-khah, and P. Siano, "Optimal operation of emerging flexible resources considering sub-hourly flexible ramp product," *IEEE Transactions on Sustainable Energy*, vol. 9, no. 2, pp. 916–929, Apr. 2018.

[170] G. Valverde, D. Shchetinin, and G. Hug-Glanzmann, "Coordination of distributed reactive power sources for voltage support of transmission networks," *IEEE Transactions on Sustainable Energy*, vol. 10, no. 3, pp. 1544–1553, Jul. 2019.

[171] Y. J. Kim, J. L. Kirtley, and L. K. Norford, "Reactive power ancillary service of synchronous DGs in coordination with voltage control devices," *IEEE Transactions on Smart Grid*, vol. 8, no. 2, pp. 515–527, Mar. 2017.

[172] K. Christakou, M. Paolone, and A. Abur, "Voltage control in active distribution networks under uncertainty in the system model: A robust optimization approach," *IEEE Transactions on Smart Grid*, vol. 9, no. 6, pp. 5631–5642, Nov. 2018.

[173] V. K. Tumuluru and D. H. K. Tsang, "A two-stage approach for network constrained unit commitment problem with demand response," *IEEE Transactions on Smart Grid*, vol. 9, no. 2, pp. 1175–1183, Mar. 2018.

[174] K. Kopsidas, A. Kapetanaki, and V. Levi, "Optimal demand response scheduling with real-time thermal ratings of overhead lines for improved network reliability," *IEEE Transactions on Smart Grid*, vol. 8, no. 6, pp. 2813–2825, Nov. 2017.

[175] E. Ucer, I. Koyuncu, M. C. Kisacikoglu, M. Yavuz, A. Meintz, and C. Rames, "Modeling and analysis of a fast charging station and evaluation of service quality for electric vehicles," *IEEE Transactions on Transportation Electrification*, vol. 5, no. 1, pp. 215–225, Mar. 2019.

[176] A. Ravey, N. Watrin, B. Blunier, D. Bouquain, and A. Miraoui, "Energy-source-sizing methodology for hybrid fuel cell vehicles based on statistical description of driving cycles," *IEEE Transactions on Vehicular Technology*, vol. 60, no. 9, pp. 4164–4174, Nov. 2011.

[177] S. Ziaeinejad, Y. Sangsefidi, and A. Mehrizi-Sani, "Fuel cell-based auxiliary power unit: Ems, sizing, and current estimator-based controller," *IEEE Transactions on Vehicular Technology*, vol. 65, no. 6, pp. 4826–4835, Jun. 2016.

[178] J. Snoussi, S. B. Elghali, M. Benbouzid, and M. F. Mimouni, "Optimal sizing of energy storage systems using frequency-separation-based energy management for fuel cell hybrid electric vehicles," *IEEE Transactions on Vehicular Technology*, vol. 67, no. 10, pp. 9337–9346, Oct. 2018.

[179] E. Schaltz, A. Khaligh, and P. O. Rasmussen, "Influence of battery/ultracapacitor energy-storage sizing on battery lifetime in a fuel cell hybrid electric vehicle," *IEEE Transactions on Vehicular Technology*, vol. 58, no. 8, pp. 3882–3891, Oct 2009.